Effect of Spatial Organization and Population Ratios on the Dynamics of Quorum Sensing and Quorum Quenching in Bacteria Communities

Maria-Fe Sayon Thielman

Thesis submitted to the faculty of Virginia Polytechnic Institute and State University in partial fulfillment of the requirements for the degree of

Master of Science
In
Mechanical Engineering

Prof. Bahareh Behkam, Chair

Prof. Alexander Leonessa

Prof. Ryan Senger

February 1st, 2024

Blacksburg, VA

Keywords: quorum sensing, quorum quenching, fluorescent reporters, flagellated bacteria, agent-based modeling, computational biology, motility in agar, engineered living materials

Effect of Spatial Organization and Population Ratios on the Dynamics of Quorum Sensing and Quorum Quenching in Bacteria Communities

Maria-Fe Sayon Thielman

Academic Abstract

Quorum sensing (QS) is a type of microbial communication used by bacteria to coordinate their behavior based on population density, regulating complex processes like biofilm formation and virulence, among other behaviors. Quorum quenching (QQ), on the other hand, disrupts this communication, usually by degradation of the QS signaling molecule. QQ offers a potential strategy for controlling bacterial behaviors linked to pathogenicity and biofouling. Despite significant advances in understanding and modeling the spatial-temporal behavior of QS, predictive modeling of QQ remains nascent, with a notable gap in the quantitative assessment of QQ's impact on QS. Here we show quantitative evaluation and characterization of the effect of QQ on QS in agar-based experiments, combined with an experimentally validated computational model. This research utilizes green fluorescence in *E. coli* MG 1655 as an indicator of QS activation, focusing on the degradation of Acyl-Homoserine Lactone (AHL), a key QS molecule in Gram-negative bacteria linked to pathogenicity, by the AiiA enzyme in engineered AiiA-producing *Salmonella* Typhimurium 14028. Our findings suggest that QQ more effectively influences QS in spatial configurations of the populations with larger interaction surfaces and shorter diffusion distances. Contrary to our initially held hypothesis, the primary effect of QQ is not a delay in QS onset but rather an attenuation of QS activity, with the area-under-the-curve of fluorescence serving as a quantitative metric. This study also introduces, to the best of our knowledge, one of the first instances of experimentally validated predictive modeling for QQ, applied to agar-based experimental setups. We posit that the quantitative experimental characterization and modeling framework presented in this research will enhance the understanding of bacterial community interactions. Enhanced comprehension of QQ and QS behaviors holds significant promise for advancing practical applications, particularly in mitigating or diminishing undesirable QS-associated activities. This is especially relevant in areas like biofouling, waste treatment, and the reduction of infections and progression of diseases in plants and animals, areas increasingly important as concerns about drug resistance in microbes and food security escalates.

An Investigation into the Effect of Quorum Quenching Bacteria on Quorum Sensing Fluorescent Reporter Strains in Bacteria Communities

Maria-Fe Sayon Thielman

General Audience Abstract

One of the ways bacteria communicate with each other is called quorum sensing (QS), where they use chemical signals to organize and time group behavior, including forming communities encapsulated in protective layers, called biofilms, and engaging in virulent attacks against hosts. Quorum quenching (QQ) in bacteria, however, disrupts this communication system, usually by breaking down the chemical signals that bacteria use to send messages to each other.

Even though QS has been studied extensively, determining how to predict and control QQ is still a nascent area of research. Here, we studied and characterized how QQ affects QS by doing experiments with bacteria populations in agar (a jelly-like substance) and applied a computational model to explain and ultimately predict the experimental observations. Engineered QS population (*E. coli* MG 1655) produced Acyl-Homoserine Lactone (AHL) signaling molecules, and engineered QQ bacteria (*S.* Tm 14028) used the Autoinducer Inactivation A (AiiA) enzyme to break down the AHL.

According to our results, QQ doesn't delay the QS bacteria's group behaviors (in our case, green fluorescent signal production); it weakens the signal instead.

Understanding QQ and QS better, especially through measurements and modeling, could lead to expanded methods of deterring harmful bacterial behavior, managing waste better, and stopping diseases in plants, animals, and humans, especially with the concerning rise of drug-resistant microbes and food security. One exciting possibility is using QQ to protect plants from bacterial infections. This could be a way to shield our crops without always relying on antibiotics.

Dedication

This thesis is dedicated to my late grandparents Fausto and Felomina Sayon and George and Susanne Thielman, to my parents Judith and Gerhard Thielman, my siblings David, Benjamin, Deborah, Joseph, and Hannah, and to my husband, Jack, and his family, whose collective support, and love, encouragement made it not only possible but a reality to pursue my graduate education at Virginia Tech. I would also like to dedicate this work to the memory of the late Dr. Preston Durrill, Professor Emeritus of Chemical Engineering at Virginia Tech, the person who most encouraged me to pursue engineering graduate school and medicine. But foremost, this thesis is dedicated to God, in the hopes that it contributes to a greater understanding and appreciation of His creation.

Acknowledgements

I wish to thank first and foremost my advisor, Dr. Bahareh Behkam, for giving me the opportunity to join her lab, for training me as a developing researcher, and for guiding the endeavors in this research project. I am deeply grateful for her mentorship and encouragement in my academic journey and endeavors. I hope as a physician I can learn to be as phenomenal a teacher, mentor, and source of support to others as she has been to me and to my colleagues in the lab. I wish to also thank the other members of the committee, Dr. Alexander Leonessa and Dr. Ryan Senger, for their help and support in this work, and whose classes and excellent teaching not only fueled my interests and curiosity but also provided the necessary background to approach this project.

I am especially grateful to Behkam Lab member Dr. Eric Leaman for training me in the laboratory and in the theory behind quorum sensing and quenching. He laid the foundations for this work, and his guidance, support, and continued advising and lending of his expertise with the model he built were invaluable throughout my journey in the lab. This thesis would not be what it is without him. In that same spirit, I would like to acknowledge another Behkam Lab member and the other original author of the model, Brian Geuther, whose work laid the foundation for both my and Dr. Leaman's computational exploration in quorum sensing and quorum quenching.

I am grateful also to all the other past and present members of the MicroN BASE lab who have helped and supported me in my journey and who have collectively created a lab culture of unparalleled professionalism, congeniality, advocacy, teamwork, and collaboration, especially Dr. Naimat Bari, Ying Zhan, Binita Saha, Alvin Aung, Bhas Karmarkar, Hajar Chokhmane, Dr. Apratim Mukherjee, and Lauren Hughes, née Berman.

I wish to thank the other engineering professors who played formative roles in my journey, most especially Dr. Alan Asbeck, Dr. Roger Chang, Dr. Sevak Tahmasian, Dr. Michael von Spakovsky, and Dr. Scott Henricks, Professor Emeritus, for their kind encouragement, mentorship, and support for my educational endeavors in the worlds of engineering and medicine.

I would also like to thank other members of the Virginia Tech faculty and staff, including Dr. Ann Stevens for her guidance and the lending of her expertise in quorum sensing and bacterial physiology, and Ms. Cathy Hill, the graduate advisor for Mechanical Engineering, for her advice and support in my graduate journey. I would also like to give heartfelt thanks to the New Horizon Graduate Scholars (NHGS) program for their support for my education, Renee Cloyd, the former director for the NHGS program, as well as Dr. Corina Sandu, the Associate Department Head for Graduate Studies. I would also thank the National Science Foundation (CAREER Award to BB, CBET-1454226) for their financial support for this research.

Table of Contents

List of Figures and Tables

List of key abbreviations:

QS	Quorum sensing
QQ	Quorum quenching
AUC	Area-under-curve (fluorescence curve or GFP curve)
AHL	Acyl-Homoserine Lactone
AiiA	Autoinducer Inactivation A
RBS	Ribosomal binding site
GFP	Green fluorescent protein
D_{AHL}	Diffusion coefficient for AHL in 0.2% agar
$V_{b,e}$	Velocity magnitude (*E. coli* MG1655)
$V_{b,s}$	Velocity magnitude (*S.* Tm 14028)
A_1	Basal rate of QS signal (AHL) production
A_2	Upregulated rate of AHL production
H	Hill constant
Q_0	AHL upregulation threshold
k_{tr}	Rate of gfp translation
k_{G_m}	Rate of maturation of GFP
R_d	Relative rate of AHL degradation in the environment
K_A	Michaelis-Menten constant for AiiA
α	Scaling parameter for initial conditions
k_A	Constitutive rate of AiiA production
k_{cat}	Specific activity of AiiA
$k_{A,deg}$	Relative rate of AiiA degradation

I. Chapter 1: Introduction

Microbes, particularly bacteria, often exist in complex communities that have a profound impact on various aspects of our world. These microbial communities, known as microbiomes, are found in diverse environments, including the human gut, cancerous tissues, and soil. In recent years, there has been growing interest in understanding how these microbiomes influence ecology, health, and disease (Cho & Blaser, 2012); (Proctor *et al*., 2019); (Delgado-Baquerizo *et al*., 2018).

The human gut microbiome, for example, is crucial for healthy digestion, immune system function, and overall well-being, including mental health (Clemente *et al*., 2012); (Margolis *et al*., 2021). In cancer, the microbiome within tumors can affect disease progression and responses to treatment (Sepich-Poore *et al*., 2021). For example, certain bacteria can convert the chemotherapy drug gemcitabine into an inactive form, leading to gemcitabine resistance in the mouse tumors, which was reversible with antibiotics (Geller *et al*., 2017); (Helmink *et al*., 2019). This suggests that co-administering antibiotics with gemcitabine treatment might enhance the effectiveness of this therapy in pancreatic cancer patients with associated bacterial infections, and of course, it opens larger questions into how large of a role bacteria play in diseases previously thought unconnected to bacteria. Environmental microbiomes also play essential roles in nutrient cycling and maintaining ecosystem stability (Delgado-Baquerizo *et al*., 2018).

i. Quorum Sensing (QS)

Bacterial communities are capable of coordinated gene expression. Quorum sensing (QS) is an example of this cooperative behavior, where bacteria regulate gene expression based on cell density. This regulation is achieved through the synthesis and detection of signaling molecules that increase in concentration when the population size increases, forming a positive feedback loop that triggers coordinated expression once the signal concentration exceeds a certain threshold. Such QS systems govern a range of bacterial processes, from metabolism to virulence, potentially influencing 5%-25% of bacterial genes (Dong & Zhang, 2005); (Helman & Chernin, 2015), including virulence, antibiotic production, and biofilm formation, to name a few. Quorum sensing systems give bacteria some characteristics of higher organisms, which

has led to the question of whether quorum sensing may have played a pivotal role in the evolution of multicellularity (Miller & Bassler, 2001).

The QS signaling molecule used in this research project is a type of Acyl-Homoserine Lactone (AHL), a group of signaling molecules comprised of a homoserine lactone ring with an acyl chain; variability in the acyl chain influences the specificity of AHL-mediated communication (Dong & Zhang, 2005). There are a wide variety of different types of QS signaling molecules beyond AHL as well, such as peptides and autoinducers-2 (AI-2) (Helman & Chernin, 2015). Recent discoveries have also led to the discovery of cyclic dipeptides and quinolones in *Pseudomonas aeruginosa* and other molecules such as diffusible signal factor (DSF) in *Xanthomonas* (Helman & Chernin, 2015), which is a cis-unsaturated fatty acid. These quorum-sensing signaling molecules are commonly preserved across numerous Gram-negative bacterial pathogens. These molecules enable both species-specific and non-specific communication, allowing bacteria to modify their behavior based on interactions with neighbors in their communities. In past years, the realm of QS research has also broadened its scope beyond just prokaryotic interactions, as it has been discovered that numerous bacterial QS signaling molecules can to influence eukaryotic organisms, which in turn have developed their mechanisms to interact with QS signaling molecules (Helman & Chernin, 2015); (Ye *et al*., 2020). By understanding QS, we gain insights into how microbial communities maintain balance and carry out their functions.

ii. Quorum Quenching (QQ)

Quorum Quenching (QQ) is the interference with QS cell-to-cell communication, usually via degradation of the QS signaling molecule to prevent the positive feedback loop from activating or deactivating the QS behavior. **Figure I.1** shows a visual aid of QS activation as the population increases, represented by expression of green fluorescence as an example of QS behavior and AHL as an example of the signaling molecule. The QS behavior is attenuated or completely diminished as the population's AHL molecule is degraded by QQ enzyme AiiA.

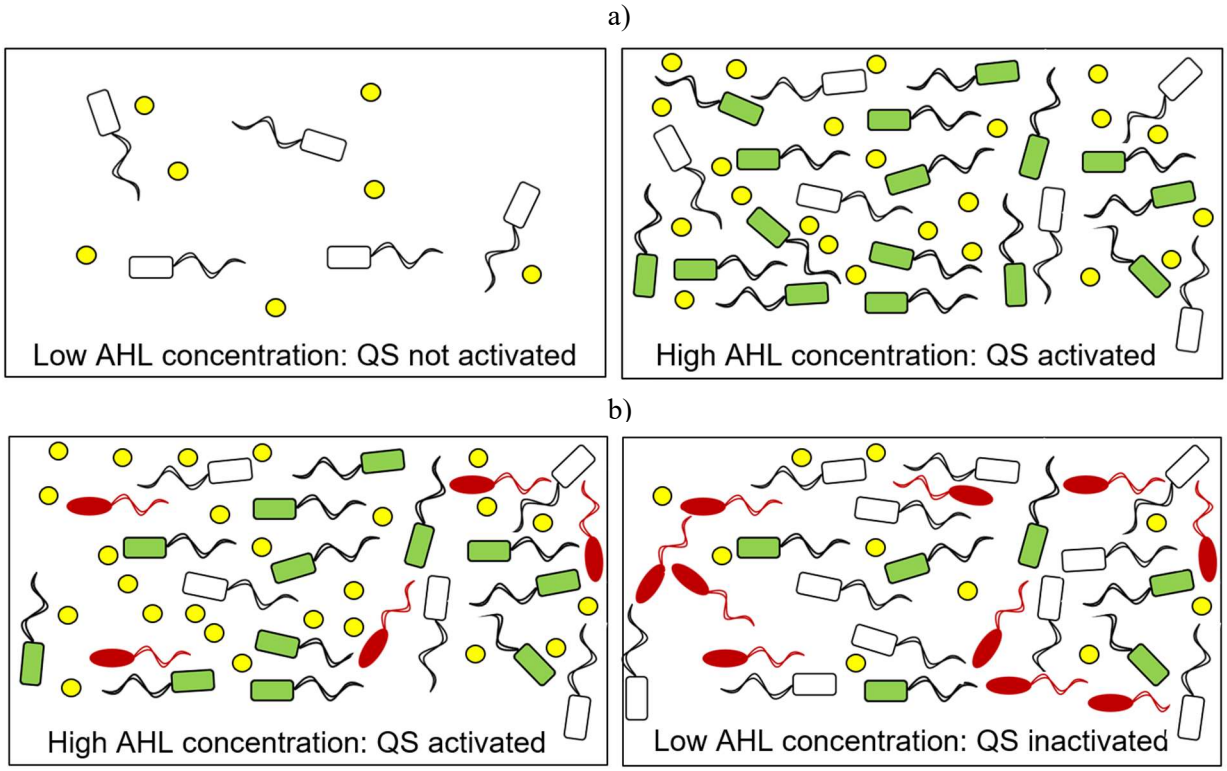

Fig. I.1. Schematic representation of QS and QQ. (a) As the AHL (yellow circle) concentration increases with increasing population size, initially colorless bacteria express QS-regulated green fluorescence. (b) Degradation of the AHL molecules by the intracellular AiiA enzyme produced by QQ bacteria (red) leads to reduction of green fluorescence expression.

A deeper understanding of QQ may improve how we treat waste as well as plant, animal, and human disease. QQ shows promise as a method of combating undesirable QS-associated behaviors, especially biofilm formation and other general pathogenicity. To provide context for the motivation of our work, the remainder of this chapter discusses the recent research on the effect of QQ in communities and QS-related bacterial behaviors.

a. Waste Treatment of Membrane Bioreactors

Membrane bioreactors (MBRs) are a type of waste treatment system for wastewater that uses biological organisms to degrade organic matter combined with membrane filtration techniques (Kim *et al.,*2023). Nonetheless, a significant issue in this process is biofouling on the membrane's surface within the filtration module, which reduces the efficiency of the MBR operation. Biofouling, the accumulation of microbial biofilms on surfaces in bioreactors, interferes with waste treatment processes, and QQ shows promise as a means of combating

biofilm formation in these reactors. For instance, Shah *et al*. (2023) introduced a composite bio-medium consisting of QQ bacteria, porous silica, and polyelectrolytes, which effectively controlled biofouling in anaerobic membrane bioreactors. This approach did not compromise the bioreactor's organic matter removal or methane production efficiency. Similarly, continuous QQ feed strategies, as demonstrated by Kim *et al*. (2023), reduced biofilm formation in membrane bioreactors, providing a dynamic solution to biofouling without the propensity to clog, which can be a challenge with stationary QQ applications. Wang *et al*. (2023) isolated novel QQ strains from municipal solid waste and demonstrated their effectiveness in reducing biofilm formation, offering potential applications in landfill waste treatment. However, QS-QQ interactions in these contexts are complex and not yet well understood (Ouyang *et al*., 2020). A deeper understanding of microbial communities and QS-QQ interactions can improve approaches taken to reduce biofouling.

b. Plant, Animal, and Human Disease

QQ also has shown promise as a method to mitigate pathogenic behavior in bacteria. Kim *et al*. (2018) demonstrated that the addition of a QQ strain reduced the AI-2 activity of Enterohemorrhagic *E. coli* in swine, mitigating gut pathogens. *Bacillus thuringiensis* strain KMCL07 successfully degraded AHL of pathogen *Pseudomonas aeruginosa* PAO1 (Anandan & Vittal, 2019) using AiiA, a quorum quenching enzyme, and reduced its biofilm formation. Rodríguez *et al*. (2020) found evidence that the naturally QQ-capable *Pseudomonas segetis* strain P6 reduced the soft rot symptoms in potatoes and carrots from *Dickeya solani, Pectobacterium atrosepticum* and *P. carotovorum* and protected tomato plants against pathogenic *Pseudomonas syringae*, suggesting biotechnological applications in agriculture. Similarly, Zhou *et al*. (2022) found that *Rhodococcus pyridinivorans XN-36* was another QQ-capable AHL-degrading strain that protected Chinese cabbage from *P. carotovorum*.

Xanthomonas campestris pv. *campestris* (Xcc) is notorious for causing black rot disease in cruciferous vegetables in the stems and leaves of plants (Ye *et al*., 2020). Xcc spreads by guttation droplets which can be transported across fields to healthy plants via flying insects, rain, wind, and water splashes, especially under humid conditions. Ye *et al*. (2020) showed that *Burkholderia anthina* HN-8, a bacterium with remarkable diffusible signaling factor (DSF) degradation capabilities, could measurably decrease black rot disease progression in infected

vegetables. Black rot, attributable to Xcc, is among the most widespread diseases affecting the crucifer (*Brassicaceae*) family worldwide, with significant occurrences reported annually.

The long-term sustainability of using biocides and antibiotics in agriculture and medicine for disease management is becoming increasingly uncertain. The rapid rise of antibiotic-resistant bacteria strains has compromised the effectiveness of numerous drugs traditionally employed in the prevention and treatment of infections, and antibiotic resistance stands as one of the biggest global health hazards of the 21st century (Pan *et al*., 2023); (World Health Organization, 2021). Projections suggest that by 2050, fatalities due to antibiotic-resistant infections may surpass 10 million annually, with the potential economic burden escalating to 10 trillion USD (Molnar *et al*., 2019). QQ holds at least some promise of addressing some of the critical challenges across various disciplines and growing the repertoire of strategies to combat harmful bacterial behaviors.

c. Challenges with QQ Applications and the Need for Further Understanding

Despite the promise in recent research, QQ-based treatments are not simple in their application or their effects, and there is a profound need for a comprehensive understanding of QQ's role in biofouling dynamics and community dynamics, in general, to progress forward with applications.

One example of research that highlights this need was unanticipated outcomes in a paper by Ouyang *et al*. (2020), where QQ treatment was expected to reduce biofilm formation in membrane bioreactors but instead did the opposite; the results showed an unanticipated increase in biofouling, contradicting initial expectations. The authors believed QQ compounds may disrupt quorum sensing systems, but their impact depends on community structure and could vary significantly depending on the specific microorganisms involved and on environmental conditions, among other factors. It could be reasonably anticipated that the same intricate community dynamics that produced unanticipated effects on biofouling could create similar challenges in utilizing QQ for mitigating plant, animal, and human diseases. Biofouling and pathogenicity are influenced by a multitude of factors, including species interactions, environmental conditions, and the presence of different microbial populations. Furthermore, Song *et al*. (2014) uncovered the presence of coexisting QQ activity in activated sludge in a membrane bioreactor, revealing a previously underestimated quorum sensing activity. Despite

the presence of QQ mechanisms, QS activities persisted and seemed to do so in a balanced dynamic, casting uncertainty on the viability of relying solely on QQ as an effective solution for reducing undesirable QS-associated activities. Predicting outcomes accurately, it appears, is a multifaceted challenge.

There is also concern about microbes developing QQ resistance. While previously believed to exert limited selective pressure due to their non-biocidal nature, QQ compounds may theoretically indeed lead to resistance in bacterial populations when exposed (Maeda *et al*., 2012). When subjected to mutation of the antibiotic efflux pump MexAB-OprM to increase efflux of exogenous C-30 (a well-established QS inhibitor) in the media, *Pseudomonas aeruginosa* became resistant to C-30 and overcame the QQ treatment that otherwise inhibited *P. aeruginosa* bacteria's pathogenic behavior toward *C. elegans* for non-mutated pathogens. Because the modification of an existing antibiotic export pump conferred resistance to a QQ compound, this work opened up a question of how easy it is for bacteria to develop QQ resistance, since it is known they readily develop antibiotic resistance. Thus, Maeda's work simultaneously supported the use of QQ for inhibiting QS-induced disease while also pointing to the threat of resistance, raising concerns about the long-term effectiveness of QQ-based strategies in disrupting QS systems. A comprehensive understanding of QQ would be a prerequisite to progress with applications to ensure the long-term viability of QQ-based treatments and approaches.

d. Efforts toward Computational Modeling of Communities and QS-QQ Behavior

Interest in modeling microbial communities has increased over the years. Dynamic models – computational or mathematical models that simulate the changes and interactions within microbial communities over time, as opposed to simple correlation studies, offer the ability to predict time-dependent properties of microbial communities, such as long-term stability, even in fluctuating environments (Qian *et al*, 2021). These models are "dynamic" because they are designed to capture and predict the temporal evolution of complex biological systems, reflecting how these systems respond to various internal and external factors. Such models open avenues to identify key microbes and molecules that exert substantial effects on community behaviors. Mechanistic models are rooted in biologically relevant hypotheses. These models offer the potential to reduce overfitting by deriving parameters from simpler

experimental systems. Other models are more empirical, driven by data and with mathematical structures lacking direct physical interpretations (Qian *et al*., 2021). Of course, machine learning could also in theory be applied to model QS and QQ interactions. While machine learning approaches may not provide direct mechanistic insights, they could assist in building biological hypotheses and designing new experiments. Wu *et al*.'s work (2022) explores the utilization of machine learning to construct a communication network for human gut microbiota, focusing on QS interactions. This avenue holds the potential for predicting and controlling QS-QQ interactions based on genetics. Although it remains uncertain whether machine learning will replace established computational models, it introduces an exciting dimension for future research. Collectively, these papers show the evolving landscape of modeling bacterial communities, offering a range of approaches, from dynamic models that capture mechanistic insights to machine learning-driven models that may foster innovative strategies for understanding and manipulating microbial behaviors.

In recent years, there has been extensive modeling work on the spatiotemporal aspects of quorum sensing behavior, including the development of an experimentally validated model that predicted the activation time of QS communities in different spatial arrangements (Leaman *et al*., 2018). When QS was induced with the rise of acyl-homoserine lactone (AHL) production, the QS bacteria reported QS activation by producing green fluorescent protein, and activation time was defined as the time at which the fluorescence (swarm behavior) reached a detectable threshold concentration. The model would best be described as a dynamic hybrid agent-based model, utilizing ODEs and PDEs to describe agent behavior at a single-agent level, while also incorporating fitting and correction factors to tune the model (Leaman *et al*., 2018) Agent-based models are computational models where the system's overall behavior emerges from the behavior of individual agents (bacteria, in this case). This type of model allows for the exploration of complex phenomena that arise from the interactions of simpler entities; in the case of Leaman's work, the model quantified QS behavior through the activation time parameter.

e. Motivation for Thesis

This thesis aims to contribute to the growing body of knowledge surrounding QQ. While extensive research has been conducted and continues to explore the potential of QQ in

adversely influencing QS-related behaviors, a significant knowledge gap persists regarding the quantitative investigation of QQ on QS bacteria community interactions. To the best of our knowledge, there has been little work in the realm of agent-based modeling of QQ and QS, and this thesis presents one of the first attempts at experimentally validating a model that predicts the effect of QQ bacteria on QS bacterial populations.

This thesis builds on the previous works from our lab by Leaman *et al*. (2016; 2018;2019; 2020) by investigating in more detail the spatiotemporal effects of a QQ-capable engineered *Salmonella* Typhimurium strain producing Acyl-Homoserine Lactonase (AiiA) on the QS-associated fluorescent signal from an AHL-producing engineered *E. coli* reporter strain. AiiA is an enzyme capable of degrading and disrupting the quorum-sensing signaling AHL molecules (Fig. I.1). By degrading AHLs, AiiA can interfere with the quorum sensing of other bacteria, potentially disrupting their ability to coordinate group behaviors and virulence. As it is a QQ compound, the AiiA enzyme is of interest for its potential applications in controlling bacterial behaviors and biofilm formation. To characterize the effect of QQ, we measured QS-fluorescence signals in QS-QQ communities with a wide range of population sizes and explored the effect of QQ agent number and the ratio of QQ agents to QS agents on QS-associated fluorescence in homogenously mixed communities in low concentration agar well experiments.

Our goal was to first explore how spatial organization affected QQ-based attenuation of QS by comparing QS-QQ interactions in four different spatial arrangements. Bacterial populations can segregate spatially based on their motility or response to physical or chemical environmental cues (e.g., when subjected to varying gradients of chemo-attractants), resulting in spontaneous separation. Differential organization behavior occurs in natural communities in connection with pathogenic behavior, as Dejea *et al.* found in their research on gut microbiota's association with colon cancer (2014). According to their study, while there is no marked difference in the bacterial types and quantities when comparing healthy tissue to tumor tissues, the way microbial communities are structured may play a role in the advancement of diseases. This phenomenon motivated our study of the interactions between QS and QQ behaviors in spatially distinct populations that retain the ability to engage in chemical communication. A significant portion of the work in this thesis involved designing,

prototyping, and developing innovative engineered living materials aimed at studying QS-QQ communities that, while not interacting physically, were able to communicate chemically through the diffusion of signals across a delineating boundary.

Our second goal was to test the hypothesis that QQ manifested its effect as a delay of the onset of QS. We complemented our work with separated communities with another set of experiments with homogenously mixed communities of different QS genetic circuit strengths. We found experimental evidence that QS behavior is indeed affected differently by QQ depending on the spatial arrangements and the size of the communication interface, based on experiments in agar wells. Furthermore, we believe that the effect of QQ does not necessarily manifest as a delay in QS activation, but rather as an attenuation of QS-related behavior (i.e., GFP expression in this study) as measured by a parameter called the Area-Under-Curve (AUC), referring to the min-normalized fluorescence in the case of experiments, or the GFP concentration in the case of simulations.

Our third goal was to experimentally validate the QQ theoretical model for different population sizes and ratios of QS and QQ agents in mixed homogenous communities. We found that our model can describe experimentally observed trends. Modeling is useful for testing and exploring scenarios and edge cases that are difficult to do experimentally.

We hope our work, albeit centered on the limited characterization of a subset of one chemical signal between two different bacteria species in a community, can contribute to the foundational efforts aimed at a broader comprehension of microbial communication, with implications for waste treatment, agriculture, and human disease and its treatment.

II. Chapter 2: Materials and methods

i. Modeling and Governing Equations

The computational platform used in this study was adapted from a prior work developed by a former lab member (Leaman *et al*., 2018);(Leaman, 2016). The original agent-based model described bacteria growth, motility, chemotaxis, and quorum sensing (QS) in aqueous environment. In this work, the model was modified to describe growth, motility, and quorum sensing in an agar medium. Furthermore, a quorum quenching (QQ) model was added. In this section, we present the governing equations for growth, motility, QS, and QQ and discuss the computational implementations.

The QS circuit had been adapted from the natural quorum sensing mechanism of *Vibrio fischeri* (Miller & Bassler, 2001) to visually demonstrate QS activity through the expression of green fluorescent protein (GFP) instead of bioluminescence. GFP signal was used to quantitatively evaluate bacterial communication and population density-dependent gene expression.

The basic components of the *Vibrio fischeri* QS system are:

- LuxI: an enzyme that produces acyl-homoserine lactone (AHL).
- LuxR: a transcriptional regulator protein that gets activated when it binds to AHL. The LuxR-AHL complex then binds to the lux operon.
- Lux operon: a set of genes (*luxICDBEG*) in *Vibrio fischeri* that encode for the luciferase enzyme, responsible for bioluminescence.

The QS bacteria in this work, used by Leaman *et al.* (2016; 2018), featured a modified circuit where the *luxCDBEG* genes in the lux operon that naturally produced luciferase had been replaced with the *gfp* gene. A visual aid of the genetic circuit is presented in **Fig. II.1**.

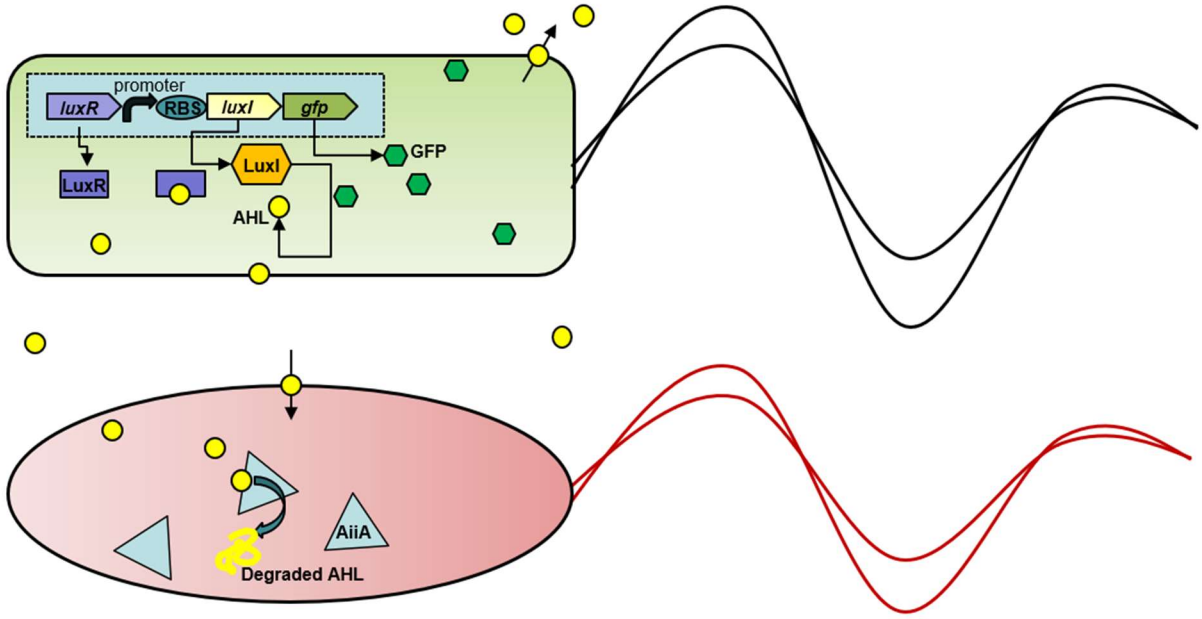

Fig. II.1. Schematic representation of QS genetic circuit. AHL signaling molecule (yellow circle) binds to the LuxR protein (purple rectangle), and the LuxR-AHL complex acts on the promoter region as transcriptional regulator of the *lux* operon, which codes for LuxI and green fluorescence protein (GFP). LuxI in turn produces AHL, which diffuses out of the QS bacterial cell and into the QQ bacterium and is degraded by AiiA (blue triangle). Regulation of the QS genetic circuit involves n_{luxI} copies of the *luxI* gene. Different ribosomal binding sites (RBS) with η_{luxI} strength can be replaced to increase or reduce the sensitivity of the circuit.

Existing LuxI protein produces AHL, which binds to LuxR protein, thus activating it as a transcriptional regulator of the *lux* operon. The LuxR-AHL complex binds to the promoter of the *luxI* gene (PluxI), which in turn triggers the production of more LuxI protein as well as GFP due to the replacement of the *lux* operon genes with the *gfp* gene. The production of more AHL by the additional LuxI creates a positive feedback loop. As more bacteria are present (higher cell density), more AHL is produced, which in turn activates more LuxR, which produces more LuxI, which produces more AHL, while more GFP is also produced.

In this modified system, the expression of GFP serves as a visual marker for quorum-sensing activity. As the bacterial population density increases, GFP expression also increases, making detectable green fluorescence signals.

a. QS Mathematical Model

Each QS agent expresses AHL molecules at a low basal rate. When the population density is high enough that a threshold concentration of AHL is reached, a positive feedback loop is triggered and the production of the signaling molecules is upregulated to a high production rate.

The AHL signaling molecules produced by the QS agents diffuse out through the cell membranes of the producing bacteria and into the environment. The concentration of AHL in the environment, designated by Q, can be modeled to change according to

1) $$\frac{dQ}{dt} = \nabla \cdot (D_{AHL} \nabla Q) - \nabla \cdot \left(\vec{V} Q\right) - R_d Q$$

where D_{AHL} is the diffusivity of AHL in the surrounding medium, $\vec{V}$ is the local fluid velocity, and R_d is the relative rate of AHL degradation, which is a percentage of the amount of AHL present (%/hr). The $\nabla \cdot \left(\vec{V} Q\right)$ term corresponds to AHL transport due to advection, was assumed to be negligible as our experiments were performed in well plates (no flow). Given the homogeneity of our experimental system in 3D, the model was also only considered in two dimensions, x, and y, to simplify the model even further.

Thus, the concentration of AHL in the environment could be described by the simpler equation

2) $$\frac{dQ}{dt} = D_{AHL}\left(\frac{\partial^2 Q}{\partial x^2} + \frac{\partial^2 Q}{\partial y^2}\right) - R_d Q$$

A small control area, 1400 × 1400 μm^2, was modeled, rather than the entirety of the well. The boundary conditions were the following for the control area within the well:

3) $$\frac{dQ}{dy}\Big|_{y=h} = \frac{dQ}{dy}\Big|_{y=0} = \frac{dQ}{dx}\Big|_{x=0} = \frac{dQ}{dx}\Big|_{x=w} = 0$$

where *h* and *w* are the height and width of the simulated domain, respectively.

A parameter called the initial condition (IC) was also defined to describe the initial QS status of the bacterial population , as given by

4) $$Q(\vec{r}, 0) = \alpha\beta$$

where β represents the number of initially fluorescent cells per image region normalized to the number of cells in the region, and α is a correction constant obtained by using a fitting method of least-squares to match the simulated activation time to the experimental activation time. β was calculated experimentally by averaging the number of initially fluorescent cells taken from the two images of each well, and dividing that quantity by the initial OD_{600} measurement, yielding a parameter with units of cells/OD, hereafter au (Section II.ii). Altogether, this parameter $Q(\vec{r}, 0)$ was used to indirectly describe the initial AHL concentration detected by all agents as necessary to reconcile delays and slightly different starting points in data collection.

The total rate of AHL production, A_t, can be modeled as a Hill function (Müller *et al*., 2006) and is given by

$$A_t = A_1 + A_2 \frac{Q^H}{Q^H + Q_0^H} \quad (5)$$

where A_1 is the constitutive (basal) rate of AHL production, A_2 is the rate of AHL production in the upregulated state, and $Q = Q(\boldsymbol{x}, t)$ is the local concentration of AHL, and Q_0 is the threshold concentration that once surpassed, triggers upregulation. Finally, H is the Hill constant.

QS activity was quantified by the expression of GFP, which is regulated by the QS circuit (**Fig II. 1**). The expressed GFP protein first is translated in an immature form, G_i, and subsequently matures into the fluorescent conformation, G_m. The translation of immature protein, G_i, and the maturation of immature G_i to mature G_m is given by a set of coupled ordinary differential equations (ODEs):

$$\frac{dG_i}{dt} = k_{tr} \frac{Q^H}{Q^H + Q_0^H} - k_{G_m} G_i - \mu G_i - k_{deg} \frac{G_i}{G_i + G_m + K_m} \quad (6)$$

and

$$\frac{dG_m}{dt} = k_{G_m} G_i - \mu_{QS} G_m - k_{deg} \frac{G_m}{G_i + G_m + K_m} \quad (7)$$

where k_{tr} is the translation rate of immature protein G_i, k_{G_m} is the rate of maturation of G_i into G_m, and μ_{QS} is the dilution of intracellular GFP concentration due to cell division and

growth of the QS population. k_{deg} is the maximum rate of GFP degradation, applied to both G_i and G_m. Lastly, K_m is the Michaelis-Menten constant representing the concentration of GFP at which the rate of degradation is half its maximum rate (assumed to be the same for G_i and G_m).

The rate of production of the protein LuxI, which is associated with QS response in experiments, is limited by the probability of ribosome association with the RNA. The translation initiation rate (TIR) serves as a parameter to indirectly quantify the probability of ribosome association. In the model, the different TIRs for different circuit constructs were accounted for by scaling the basal and upregulated rates of AHL production A_1 and A_2, respectively, by factor η_{RBS}, given by

8) $$\eta_{RBS} = \frac{R_{RBS}}{R_{B0034}}$$

where R_{RBS} is the TIR of the RBS in the construct that is being modeled and R_{B0034} is the TIR of the reference RBS of TIR = 1262 au, referred to interchangeably in this thesis as the BioBrick construct (Chapter II.i). If additional copies of the *luxI* gene were incorporated into the circuit, then the baseline AHL production rate, A_1, was multiplied by the number of copies, n_{luxI}. Thus, the modified rate of AHL production to account for different TIRs and various numbers of copies of the *luxI* gene was given by

9) $$A_t = n_{luxI}\eta_{RBS}A_1 + \eta_{RBS}A_2\frac{Q^H}{Q^H + Q_0^H}$$

b. QQ Model

Quorum quenching, as mentioned in the introduction, is the process of interfering with the QS process (Fig. II.1). Experimentally, *Salmonella* Typhimurium strain (ATCC 14028) engineered to produce an AHL-inactivator protein, autoinducer inactivation A (AiiA), was used to inhibit QS responses and behavior. AHL degradation by AiiA is usually assumed to be a second-order reaction (Momb *et al*., 2008), but can be reasonably assumed to follow Michaelis-Menten kinetics (Anandan & Vittal, 2019), and was thus modeled in this work to be related to the concentration of AiiA by

10) $$Q^- = k_{cat}A\frac{Q}{K_A + Q}$$

where Q^- is the rate of AHL degradation by AiiA, Q is the concentration of AHL, k_{cat} is the specific activity of AiiA, A is the concentration of AiiA, and K_A is the concentration of Q at which the rate of Q degradation is half of the max possible rate (Leaman, 2016).

Unlike AHL, which leaves the QS agent membrane and diffuses into the environment, AiiA is limited to staying within the QQ agent cell membrane. The rate of change of AiiA in each QQ agent is given by

$$\frac{dA}{dt} = k_A - \mu_{QQ}A - k_{A,deg}A \quad (11)$$

where k_A is the constitutive rate of AiiA production, μ_{QQ} is the growth rate of the QQ agents, and $k_{A,deg}$ is the relative rate of AiiA degradation. The absolute rate of degradation depends on the total amount present.

c. Overview of Model Implementation

Combining the QS and QQ models, the overall model can be described below. At each time step, each QS agent releases a certain number of AHL signaling molecules into the four concentration nodes nearest the agent, and that number of AHL molecules released into the environment is given by

$$N_{QS}(x, y) = A_t(x, y)\,\Delta t \quad (12)$$

If the agent was between nodes, then the concentration put into each of the nearest nodes was not equal but was corrected for using interpolation.

For QQ agents, the rate of AHL removal was given by

$$N_{QS}^{-}(x, y) = Q^-(x, y)\Delta t \quad (13)$$

At each time step, the motility functions were called and the agent translated in space at speed V_b a distance $V_b\Delta t$ if it was in the run phase or remained stationary if it was in the tumble phase. In the simulations, the following were used: a timestep of 0.01 min, simulated domain of 1400 × 1400 μm^2, agent position mesh size was 1× 1 μm^2, and AHL reaction-diffusion model mesh size was of 70 × 70 μm^2 (20 × 20 grid within the 1400 × 1400 μm^2 domain). The timer, whether running or tumbling, was compared to the time step. If $\Delta t \geq \tau_{remaining}$, then

new timers were set and the bacterium started the next time step in the opposite phase, at a different orientation. If the simulation time step was greater than the time remaining in the run or tumble phase, then the agent would switch to a run or tumble as appropriate at the next time step, and the t_{remain}, rather than the time step, would be input into the run function, to prevent the bacterium from overshooting its run, which would lead to error compounding. At the end of each time step, the mesh is updated with the new positions of agents and new concentrations of AHL.

The number of QS and QQ bacterium in experiments is not static, however. To model bacteria growth, the growth was defined as

$$P^*(t) = \frac{P(t)}{P_0} \tag{14}$$

where $P(t)$ is the population size at any point in time, and P_0 is the initial population. Guided by experimental results (Chapter IV.i), bacterial growth in the agar wells was modeled as a quadratic polynomial function, instead of exponentially, according to

$$P(t) = at^2 + bt + 1 \tag{15}$$

where the coefficients were determined based on experimental growth data.

At each time step, the probability of the agent dividing was related to the total population and was given by

$$p_{double} = \frac{\Delta t \Delta P}{\Delta t_g P(t)} = \frac{\Delta t P_0 \left(P^*(t) - P^*(t - \Delta t_g)\right)}{\Delta t_g P(t)} \tag{16}$$

where Δt_g is the time required for the population to increase by one agent, according to the model for population growth, $P(t)$. A random number between 0 and 1 was chosen and sampled, and if that sampled number was less than the calculated probability of division, p_{double}, then the agent divided in the simulation. In the case that the sampled number was greater than p_{double}, the agent did not divide. A 5000 total agent (QS + QQ) ceiling was applied to prevent computational errors due to crowding, as excess population led to the simulation not advancing. If the population exceeded 5000 agents, all growth was turned off. Superposition, or the presence of two agents in one location, was avoided by relocating each

agent to nearest adjacent nodes if collision or position overlap occurred, a process called "Volume Exclusion."

In the simulation, the bacteria were considered to have activated when the intracellular mature green fluorescent protein (GFP) concentration surpassed 654 nM. Area-Under-Curve was calculated by multiplying the intracellular GFP concentration by the timestep (30 seconds), and summing the values from t = 0 to t = 300 minutes (the total duration of the simulations).

Most parameters and features from Leaman's model were retained (**Table 1**). Adjustments were made to align with experimental variations, including changing the AHL diffusion coefficient, the basal and upregulated rates of AHL production, the AHL upregulation threshold, and the motility speeds of *E. coli* and *Salmonella*. The latter were derived from motility experiments, while AHL production rates and thresholds were adjusted from literature estimations through linear regression, correlating experimental and model activation times. Additionally, the GFP concentration threshold for considering activation was also increased. We tripled the GFP threshold to compensate for increased opacity of the agar medium. This adjustment is acknowledged as an estimated factor and would benefit from more detailed analysis and refinement, as discussed in the final chapter.

Converting from OD_{600} measurements to simulation agent count was given by

$$17) \qquad N = \left(5 \times 10^{8} \frac{CFU}{mL}\right) * \left(1 \times 10^{-12} \frac{mL}{\mu m^3}\right) * (d^2\ \mu m^2) * (1\ \mu m) * OD_{600}$$

where N is the number of agents (in the simulation), and d is the simulated domain length (assuming square domain). A 1 μm thickness represents unit depth in the 2D model.

Table 1. Model Parameters

Parameter	Symbol	Value	Units	Source
Diffusion coefficient for AHL in 0.2% agar	D_{AHL}	1.11×10^4	μm^2 / sec	(H. Song *et al*., 2009)
Average run duration in absence of a chemoeffector gradient	τ_0	0.86	s	(E. J. Leaman *et al*., 2018)
Average tumble duration	τ_T	0.14	s	(Leaman *et al*., 2018)
Velocity magnitude *(E. coli* MG1655)	$V_{b,e}$	28.6	μm / sec	Measured
Velocity magnitude *(S.* Tm 14028)	$V_{b,s}$	33.5	μm / sec	Measured
Mean change in bearing between successive run changes	θ_μ	68	degrees	(Leaman *et al*., 2018)
Standard deviation of bearing between run phases	θ_σ	36	degrees	(Leaman *et al*., 2018)
Basal rate of QS signal (AHL) production	A_1	3.0	Molecule / second	Fitted
Upregulated rate of AHL production	A_2	297.3	Molecule / second	Fitted
Hill constant	H	2.5		(Leaman *et al*., 2018)
AHL upregulation threshold	Q_0	2.8	nM	Fitted
Rate of *gfp* translation	k_{tr}	4.20×10^{-1}	Molecule / second	(Leaman *et al*., 2018)
Rate of maturation of G_i to G_m	k_{G_m}	3.16×10^{-3}	s^{-1}	(Leaman *et al*., 2018)
Maximum rate of GFP degradation	k_{deg}	1.5	nM / sec	(Leaman *et al*., 2018)
Concentration of GFP to achieve half-maximum rate of GFP degradation	K_m	1625	nM	(Leaman *et al*., 2018)
Relative rate of AHL degradation in the environment	R_d	10.80	% hr^{-1}	(Leaman *et al*., 2018)
Michaelis-Menten constant for AiiA	K_A	1.0	mM	Estimated, (Leaman *et al*., 2018)
Scaling parameter for initial conditions	α	2.24	nM	Fitted, (Leaman *et al*., 2018)
Constitutive rate of AiiA production	k_A	105.7	Molecule / second	Estimated, (Leaman *et al*., 2018)
Specific activity of AiiA	k_{cat}	22.7	s^{-1}	Estimated, (Leaman *et al*., 2018)
Relative rate of AiiA degradation	$k_{A,deg}$	0.1	% hr^{-1}	Estimated, (Leaman *et al*., 2018)

The primary bacteria model was solved in C++ to generate the AHL concentration field, and then solving of the coupled differential equations (Equations 6 and 7) to obtain GFP concentration over time was done in a separate Python script (Leaman, 2016) for each timestep after the AHL spatial-temporal data was generated. **Figure II.2** shows the process flow of the integrated Python/C++ model.

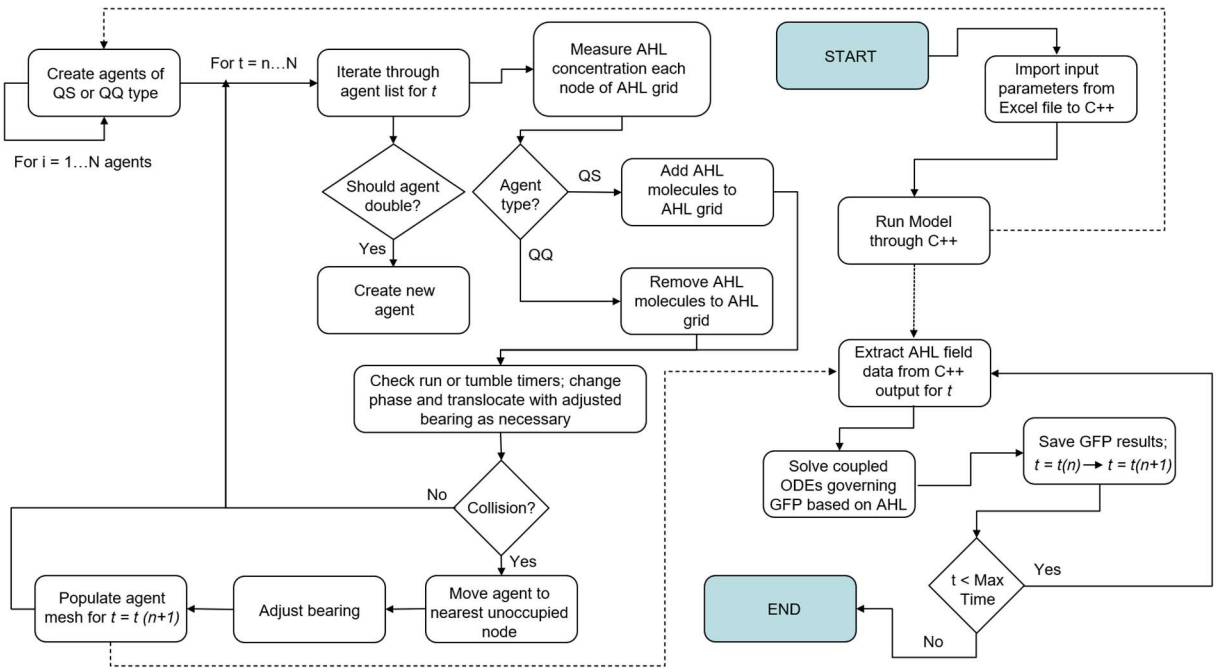

Fig. II.2. Flowchart of model process of the agent-based model.

The Python script used by Leaman (2016), uses the *scipy.integrate.odeint* function for solving differential equations, which, in turn, employs the LSODA (Livermore Solver for Ordinary Differential Equations) algorithm, relying on LSODA's capability to adaptively choose the most appropriate method (Adams-Moulton or backward differentiation formulas) based on the stiffness of the differential equations being solved. This choice is made internally by the LSODA algorithm.

To optimize the model parameters for our media, the model output activation time was compared to the experimental outcome for approximately 2/3 of the TIR 1262 QS-only dataset. A_1, A_2, and Q_0 were then slightly altered, and another iteration was run to compare the error between the model and the experimental activation time. After approximately 100 iterations, the final parameters that led to the lowest error across experiments (approximately within +/-

18% error averaged for experiments with 20 or more agents using the "large" population model) were selected to move forward with. The model with optimized parameters was then validated against the remaining 1/3 QS-only experiments, before being applied to the QS-QQ dataset. Note that all optimization was done using the "large" growth model and experiments with more than 20 agents, as the large growth model had reduced sensitivity to the uncertainties associated with population growth modeling.

ii. 0.2% Agar Well Experiments

As mentioned previously, the experiments described in this thesis utilized engineered strains previously developed in our laboratory (Leaman *et al.,* 2018; 2016*)*. In that previous foundational work, the wild-type *E. coli* MG1655, known for high motility, was isolated and engineered to contain a quorum sensing (QS) circuit. Different QS strain variants were created with reduced ribosomal translation initiation rates (TIR), and thus less sensitive QS genetic circuits. Additionally, *Salmonella enterica serovar* Typhimurium (*S.* Tm) 14028 was modified to incorporate a synthetic quorum quenching (QQ) circuit and to express red fluorescent protein (RFP) (Leaman *et al*., 2018). Casamino acids were prepared from a dry solution, filtered, and subsequently stored as a stock solution prior to their addition to the 0.2% agar LB (Lysogeny Broth) Miller solution that was used in the experiments. For the *E. coli* MG1655 1262 au plasmid and the *S.* Tm 14028, 35 µg/mL concentration of Kanamycin antibiotic was necessary to promote retention of the synthetic plasmids. The QS constructs with 99 au and 30 au RBS strengths required Tetracycline (15 µg/mL) antibiotic.

The QS *E. coli* and QQ *S.* Tm strains were revived from -80°C stock cultures and streaked on cold (4°C) LB Miller 1.5% agar plates supplemented with the appropriate antibiotics as mentioned previously. *S.* Tm plates were incubated for 10-14 hours overnight at 37°C, whereas *E. coli* plates were consistently grown for 10 hours overnight at 37°C.

For *S.* Tm*,* a single colony was inoculated into 5 mL of LB Miller and grown overnight in a round-bottom culture flask on a rotating shaker at 100 rev/min and at 37°C; subsequently, 50 µL of the *S.* Tm overnight culture was inoculated into 10 mL of LB Miller broth and cultured for an additional 8-12 hours to an optical density at 600 nm (OD_{600}) of approximately 1.0.

E. coli was inoculated from a single colony directly into 10 mL of broth at the same conditions (100 rev/min and 37°C) and harvested at an OD_{600} of 0.05 to prevent premature QS activation. While the target OD_{600} values for *E. coli* and *S.* Tm were 0.05 and 1.0, respectively, to synchronize their readiness, in practice, the *S.* Tm were harvested at OD_{600} ranging from 0.8 to 1.2, and *E. coli* was harvested at OD_{600} of 0.05 ± 0.005 in most experiments.

Figure II. 3 shows a visual aid of the steps used in the experimental phase of this work.

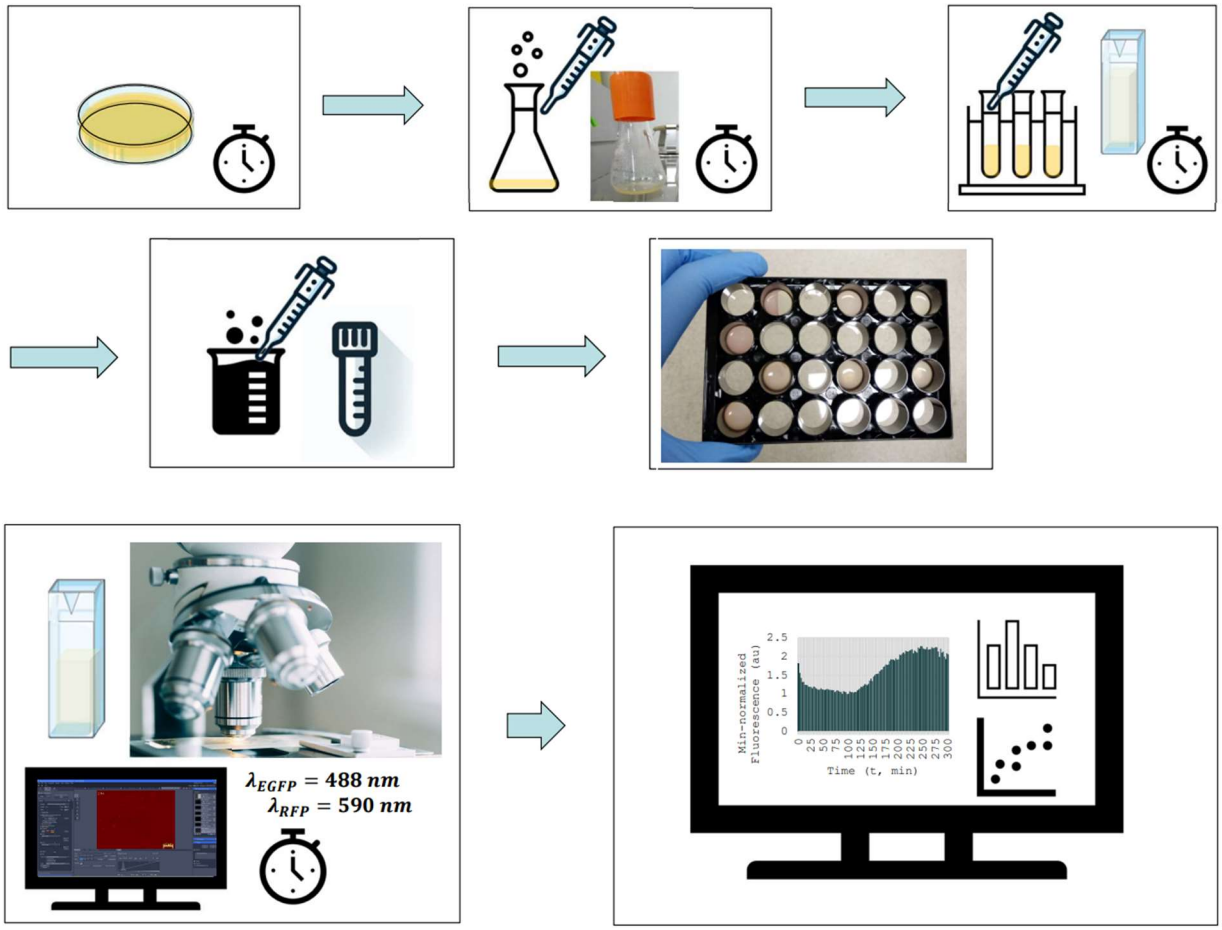

Fig. II.3. Experimental process flow. In direction of arrows: 1) Bacteria streaked on cold (4 °C) Lysogeny Broth (or LB broth (Miller)) 1.5% agar plates with appropriate antibiotic from -80 °C stock. *E. coli* was grown for 10 hours and *Salmonella* for 12 hours at 37 °C. 2) Single colony of *E. coli* inoculated directly into 10 mL of LB media; rotated on shakers at 100 rpm at 37 °C. *Salmonella* grown in overnight culture before sub-culture under the same conditions. 3) *Salmonella* harvested at OD_{600} = 1.0 and *E. coli* harvested at OD_{600} = 0.05; centrifuged at 1.7 RCF and resuspended in <0.3 mL of LB. 4) Final composition (1 mL) for wells prepared: 0.8 mL of 0.2% (or 0.6%) agar, 0.2 mL of diluted bacteria resuspension, and 0.41 % w/v casamino acids. 5) A0.500 mL (0.300 mL for 0.6% agar experiments) aliquot was pipetted into each test well in 24-wellplate. Control: blank well with no bacteria. 6) OD_{600} of the bacteria suspensions was measured at the start of data collection. Wells were imaged 400 µm × 300 µm of each well every 2.5 min at 40× magnification (50 ms exposure time for fluorescence imaging; 10 ms exposure time for phase imaging) for 300 minutes at 37 °C at two z-locations (z = 0 and z = 30 µm from the bottom glass). 7) Images were exported to obtain mean gray value in ImageJ (Fiji). Figure was prepared in part with BioRender.

After reaching the target OD values, or as close as feasible, the cultures were centrifuged at 1.7 Relative Centrifugal Force (RCF) for 5 minutes, resuspended in LB Miller without washing, and then diluted to the desired OD values for introduction into the experimental wells. The experimental media composition for well inoculation was as follows: 800 µL of 0.2% agar LB Miller supplemented with 0.41 % (w/v) of casamino acids, the appropriate LB bacterial suspensions to achieve the target introduced OD_{600} values, and additional LB media without bacteria, referred to as "blank LB," to yield 1 mL. Though antibiotics were used to promote plasmid retention during culture phase, antibiotic was not added in the experimental wells due to the short duration of the experiments. From this mixture, for each case, 500 µL were dispensed into a well of a 24-well plate. Before commencing data collection, the OD_{600} values for base resuspension solutions of *E. coli* and *S.* Tm were measured such that the concentrations of *E. coli* and *S.* Tm in the wells could be calculated based on dilution ratios given the known volumes of base resuspensions that were used in each well. To mitigate potential signal interference, bacterial populations were not placed in adjacent wells but were instead separated by at least one empty well. Most of the fluorescence assays included the testing of a minimum of six different scenarios or “test cases”, encompassing varied population densities or QQ/QS ratios, as well as a blank control well containing the same media and agar composition but without bacteria to assess and account for any inherent autofluorescence of the media.

For microscopy imaging in well experiments, a 40× magnification was used at the base of the glass and approximately 30 µm from the bottom, with exposure times set to 50 milliseconds for the EGFP and RFP channels at $\lambda_{EGFP} = 488\ nm$ and $\lambda_{RFP} = 590\ nm$ respectively, and 10 ms for phase imaging. For fluorescence and growth experiments (or experiments where both phase and fluorescence data was obtained), the imaged area was approximately 400 μm × 300 μm. For motility data collection, the well was imaged at 30 µm from the bottom glass at 60 frames per second (FPS), 12.5 ms exposure time using a high-speed camera, with an imaged area of 160 μm × 120 μm.

iii. 0.6% Agar Well Experiments

Due to the high bacteria motility in 0.2% agar, 0.6% agar was used to facilitate spatial organization of the populations into distinctly separate regions. Bacterial suspensions were

prepared by harvesting cultures, as previously outlined. For each experiment, volumes of the bacterial resuspensions were combined with a prescribed volume of sterile LB broth to achieve a combined volume of 200 µL per Eppendorf tube. In experiments involving split configurations, different bacterial populations were segregated into individual tubes. A volume of 800 µL of 0.65% agar in LB broth, liquefied through autoclaving or microwave heating and subsequently cooled to a temperature comfortable to touch and safe for bacteria, was added to each tube containing the bacterial suspension, and then mixed before being pipetted and allowed to cool into its final shape.

For homogeneously mixed QS and QQ population experiments, 300 µL of the bacterial-agar mixture was introduced into each well. In the split bulk configuration (i.e., QS and QQ bacteria are each restricted to 1/2 of the well), 150 µL of *E. coli* suspension was added to the wells, with a sterile semicircular disk of Polydimethylsiloxane (PDMS) pressed against the glass bottom serving as a placeholder in the remaining space. After the *E. coli*-containing agar solidified, the PDMS placeholder was carefully lifted and removed from the well space, and 150 µL of *S.* Tm suspension was introduced to occupy the vacated space, completing the agar disk formation.

In the split layer approach (i.e., QS and QQ bacteria are each restricted to a thin film and the films are stacked), a thin layer of *E. coli* suspension was first placed at the bottom of each well and allowed to solidify, followed by the addition of *S.* Tm agar directly atop the *E. coli* layer, which was then also left to solidify.

Each experimental run incorporated a minimum of one replicate from each of the following categories: QS-only Homogenous, QS-QQ Homogenous, QS-QQ Split Bulk, and QS-QQ Split Layer. Additionally, control and test experiments were conducted; in these, the wells were prepared following the same protocol as described previously. However, for the Split Bulk and Split Layer configurations, only *E. coli* was used, omitting the *S.* Tm component in the counterpart agar semi-disk or top agar layer.

iv. Fluorescence Analysis: QS Activation Time and QS-reporter green fluorescence Area-Under-Curve

As described earlier, the QS circuit in this study produced a QS-regulated GFP signal (**Fig. II.1**). Fluorescent images captured at intervals of 2.5 minutes were exported as TIFF files and analyzed using Fiji (ImageJ) software to calculate fluorescence values. In this process, the entirety of the image composed of four tiles was exported from the .czi file with a consistent contrast setting in Zen software. The series of images corresponding to each well and time point were imported into Fiji, converted to 8-bit grayscale, and the mean gray value was measured at each time point. This dataset was subsequently normalized relative to the minimum value within each experiment case, such that fluorescent curves in all experiments had minimum fluorescence values of 1.0. For a discussion on different considerations for approaching the analysis of the experimental data, see Appendix 1.

The activation time was defined as the time in minutes when a sustained increase in normalized fluorescence above the 1.10 threshold first occurred. To qualify as "sustained," the normalized value was required to exceed 1.10 for at least three consecutive 2.5-minute timesteps, representing a 7.5-minute interval. The fluorescence data from both imaged z-locations in the well were analyzed separately, and then the activation time for the experiment case well was calculated as an average of the activation time from the two image sets. Finally, at least one image set out of the two for each well had to exceed 1.2. Cases failing to meet these criteria were classified as non-activating. This evaluative approach is referred to as the "110% threshold method" for activation time quantification in the rest of this thesis and was used moving forward.

In the simulation, activation time, as mentioned in Section II.c, was the time point when internal GFP exceeded 654 nM.

To establish initial conditions (IC), images captured both at the bottom of the wells and at a position 30 μm were uniformly exported at a predefined contrast setting that enhanced countability of initial fluorescent bacteria. The count of fluorescent bacteria obtained from these images was then averaged for the two different z-heights and normalized against the initial optical density (OD) introduced into the wells, yielding an initial condition value in

arbitrary units (au). In the simulation, this experimental value was multiplied by the scaling parameter α to give a head-start AHL value (Eqn. 4).

In our well experiments, a consistent initial fluorescence was observed that would subsequently dissipate. After investigation, this phenomenon was determined to be independent of bacterial fluorescence, and an artifact of the experimental apparatus, as evidenced by its presence in both the blank control wells and those containing bacteria, to comparable degrees. The control wells exhibited a steady fluorescence profile following the decline of the initial fluorescence, while the fluorescence curves of the wells with bacteria rose, if they were activated. Consequently, any fluorescence observed before the curve's minimum point was excluded from the Area-Under-Curve (AUC) analysis (**Fig. II.4**).

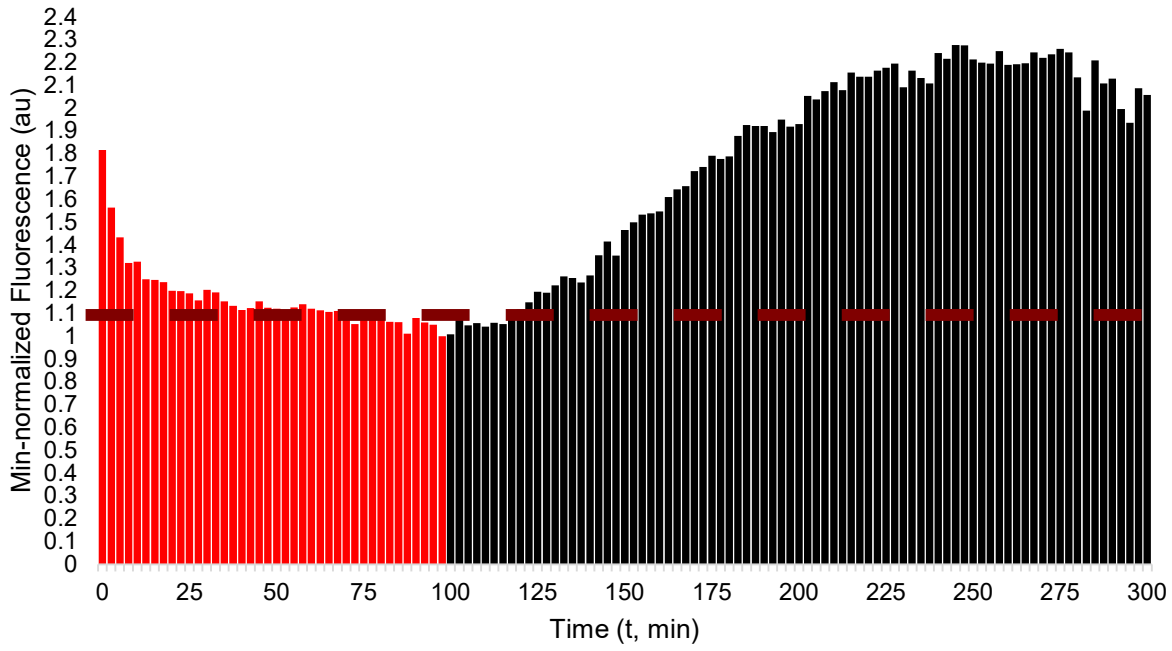

Fig. II.4. Representative normalized GFP fluorescence signal as a function of time for Area-Under-Curve (AUC) calculation method. All points before the minimum fluorescence value (red) were excluded from the AUC calculation. From the minimum fluorescence point onward, values were zeroed if below 1.10, and then remaining values were added together and multiplied by the time step (2.5 minutes in experiments), to give the AUC value.

From the minimum fluorescence point onward, the fluorescence values were zeroed (set to zero) if below 1.10 such that only values following activation were left, and then those remaining values were added together for the remainder of the 300 minutes and multiplied by the time step (2.5 minutes in experiments), to give the AUC value. Similar to activation time, the AUC for each case was an average from the two image sets' individual AUC values.

In the simulation, the AUC for GFP expression over time was calculated by multiplying the simulated concentration of mature GFP at each time point by the length of the respective timestep (0.5 minutes in the simulation) and summing the resultant values from t = 0 to t = 300 min.

v. Growth Analysis

Growth quantification involved the manual counting of in-focus bacteria from brightfield images taken at a specific focal plane, approximately 30 μm from the glass bottom, to minimize any bias from potential sedimentation. This manual process introduced elements of subjectivity and potential error, particularly when discerning partially focused bacteria or dealing with densely populated fields. The counts of in-focus bacteria were standardized against the initial counts, resulting in a normalized growth curve starting at a baseline of one. Two different quadratic polynomial growth models were determined to more effectively characterize the bacterial growth patterns observed in the current study, as opposed to the linear model employed for the microfluidic experimental setup in the investigations conducted by Leaman *et al*. (2018). The coefficients for the quadratic growth equations of large and small populations were computed from numerous wells across various experiments with different starting populations to ensure that a singular OD did not bias the growth rates (Section IV.i).

Due to the challenges of distinguishing between *S.* Tm and *E. coli* at 40× magnification in brightfield, growth rates were calculated separately for each species based on monoculture wells. It was estimated that *S.* Tm would exhibit a growth pattern like that of *E. coli*. The effect of co-incubation of two bacterial strains on growth rate of each strain will be explored in future studies.

vi. Motility Analysis

For motility, high-speed videos at 60 FPS were collected at a depth of 30 μm from the bottom glass in the well, for *S.* Tm and *E. coli* populations, and random individual bacteria were tracked during runs to obtain average speeds across those runs.

III. Chapter 3: Experimental Results and Discussion

Our goal was to first explore how spatial organization of the QS and QQ bacterial communities affected QQ-based attenuation of QS by comparing QS-QQ interactions in 4 different spatial arrangements. We found that Split Bulk activated the fastest and had the highest AUC values, and Split Layer activated the slowest and had the lowest AUC values.

Our second goal was to test the hypothesis that QQ manifested its effect as a delay of the onset of QS, and we found that this is not always true. We observed that QQ may not delay QS activation time and rather attenuate QS signal (quantified as reduced AUC of the QS GFP signal) . Thus, activation time and AUC results together provide a better picture of the effect of QQ on QS than either parameter individually.

Finally, our third goal was to experimentally validate the QQ theoretical model for different population sizes and ratios of QS and QQ agents in mixed communities.

We will discuss the results of the first two goals in this section, and the results toward the third goal will be discussed in Chapter IV.

Figure **III.1** below shows representative microscopy images of the effect of QS-regulated GFP signal (Fig. III.1b) and the effect of QQ bacteria on the GFP signal intensity (Fig. III.1a). .

(a)

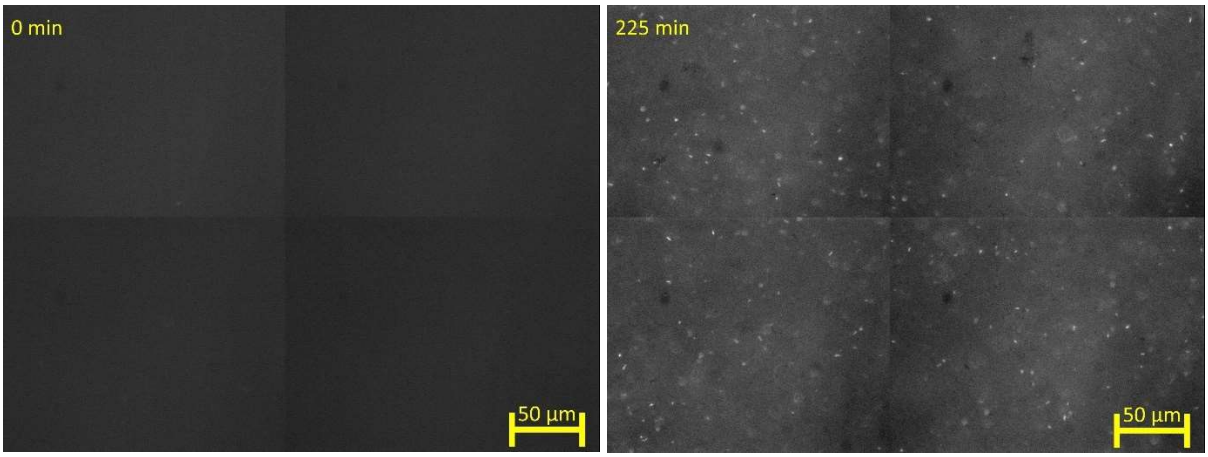

(b)

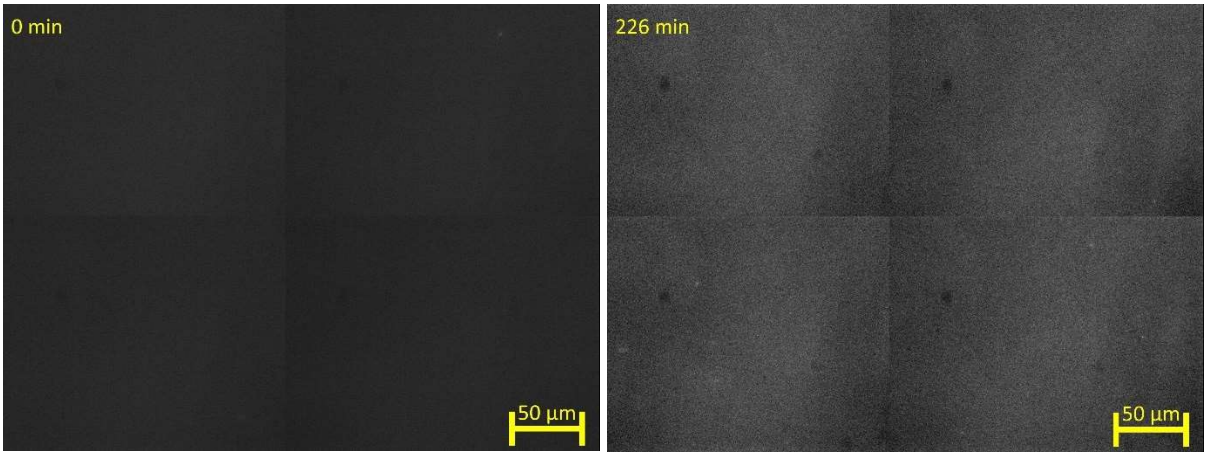

Fig. III.1. Microscopy images of QS-regulated green fluorescence signal of QS-only (a) and QS-QQ (b) experiments. (a) 23 QS agents; Initial condition = 168 au; (b) 23 QS agents, 88 QQ agents; Initial Condition = 274 au.

i. 0.6% Agar Experiments with Highly Sensitive QS strain

We inquired if the spatial arrangement of the QS and QQ bacteria would affect the dynamics of their interactions. The hypothesis was that spatially separated populations would exhibit a diminished influence of QQ agents on QS fluorescence behavior. A significant part of this thesis's experimental phase involved the development of an experimental approach to create the desired spatial organization of the two bacterial populations. The different geometries investigated are depicted in **Fig. III.2**. It is important to note that each geometry has the same number of bacteria of each type of population (except for QS-only) within the entire well, but

depending on arrangement, that population is concentrated in one sublocation or spread throughout.

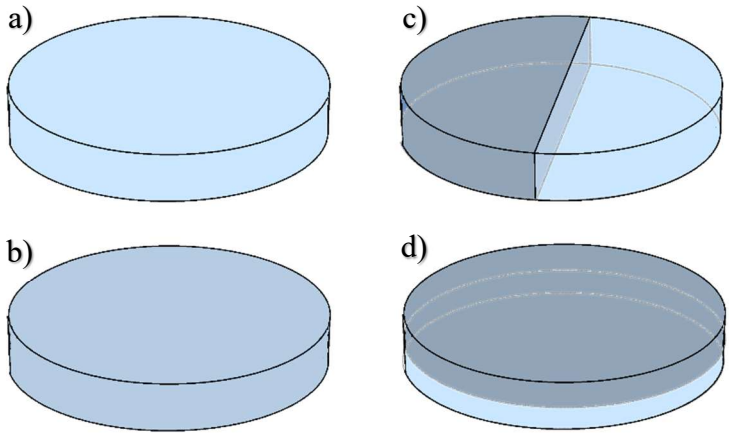

Fig. III.2. Visualization aid of different spatial geometry arrangements for 0.6% agar experiments. (a) QS-only Homogenous; (b) QS-QQ Homogenous; (c) QS-QQ Split Bulk; (d) QS-QQ Split Layer. Lighter blue represents QS bacteria; darker blue represents QQ bacteria, and medium blue represents a mix or interface.

To achieve this, we identified an appropriate agar concentration that would inhibit bacterial motility at 37 °C (experimental conditions) while remaining sufficiently fluid for pipetting and setup at a temperature that wouldn't harm the bacteria. A 0.6% agar concentration was chosen after several trials and successful proof-of-concept experiments with spatially separated wells. A few individual bacteria were still motile in 0.6% agar, but the population overall was non-motile and would not cross the delineating agar boundary. Agar concentrations below 0.6% allowed too much motility and bacteria were found to migrate across the boundary, while higher concentrations significantly reduced the viable window for pipetting, hindering the practicality of the experimental setup.

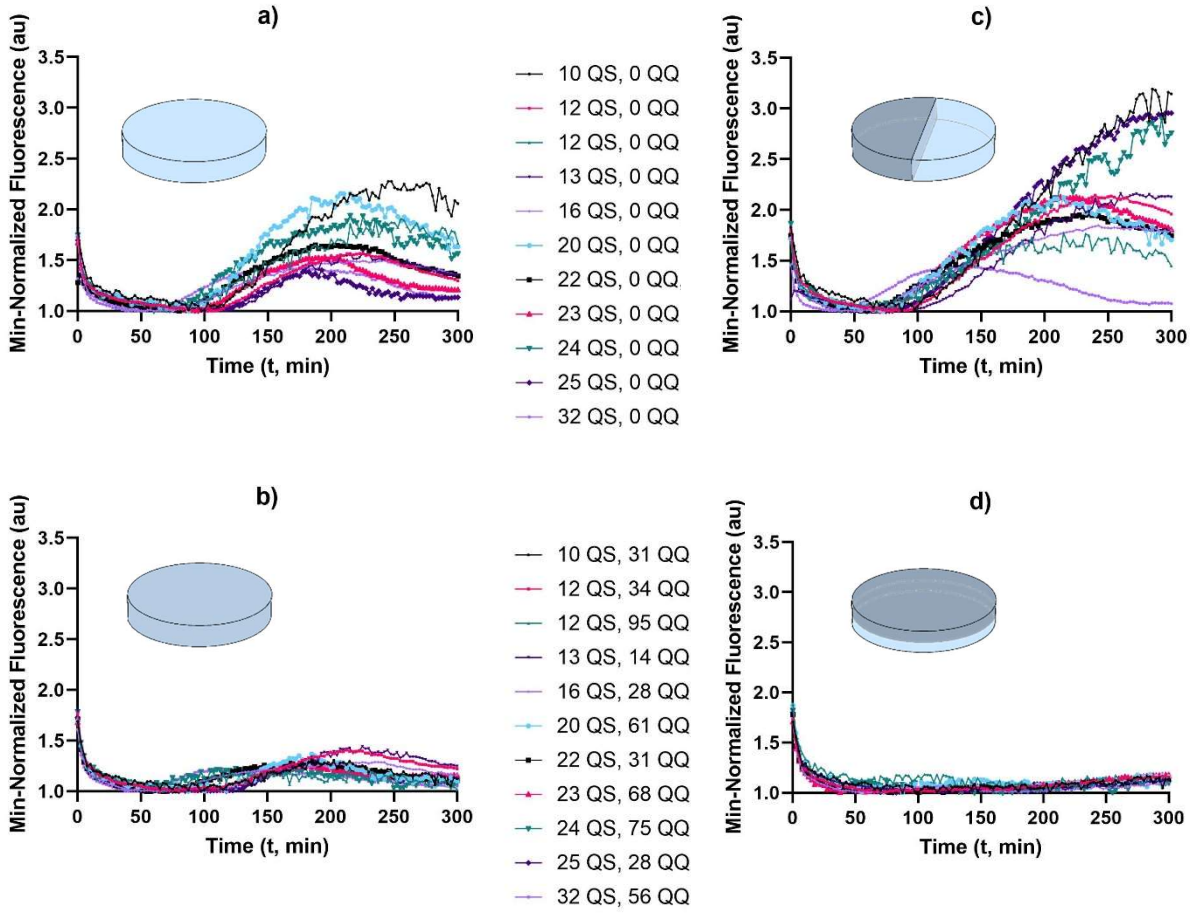

Fig. III.3. Min-normalized fluorescence curves for different spatial arrangements of QS-QQ communities. (a) QS-only homogenous; (b) QS-QQ homogenous; (c) QS-QQ split bulk; (d) QS-QQ split layer. Note that all four configurations test the same number of QS agents in the whole well and (b), (c) and (d) have the same number QQ agents, but equivalent experiments have slightly different initial conditions.

Figure III.3 shows that both homogenous QS-QQ populations (Fig. IIIb)and split-layer populations (Fig. IIId) exhibited lower signal intensities. Each associated test case maintained consistent QS/QQ ratios and agent counts, ensuring that the comparison was focused on spatial arrangements. The observation that QS agents in QS-only and QS-QQ split bulk schemes were less impacted by QQ agents aligns with our expectations, given the limited mixing and interaction in these setups compared to homogeneously cultured communities (QS-QQ homogenous) or those with interacting thin layers (QS-QQ split layer). In the case of QS-QQ split layer arrangements, it is theorized that despite the spatial separation of populations, the

extensive boundary surface area and reduced diffusiondistance facilitatedd interaction and the diffusion of AHL signals for degradation. The QS-regulated GFP signal intensity is further characterized in the heat maps and Area Under the Curve (AUC) graphs presented below in **Figure III.4**.

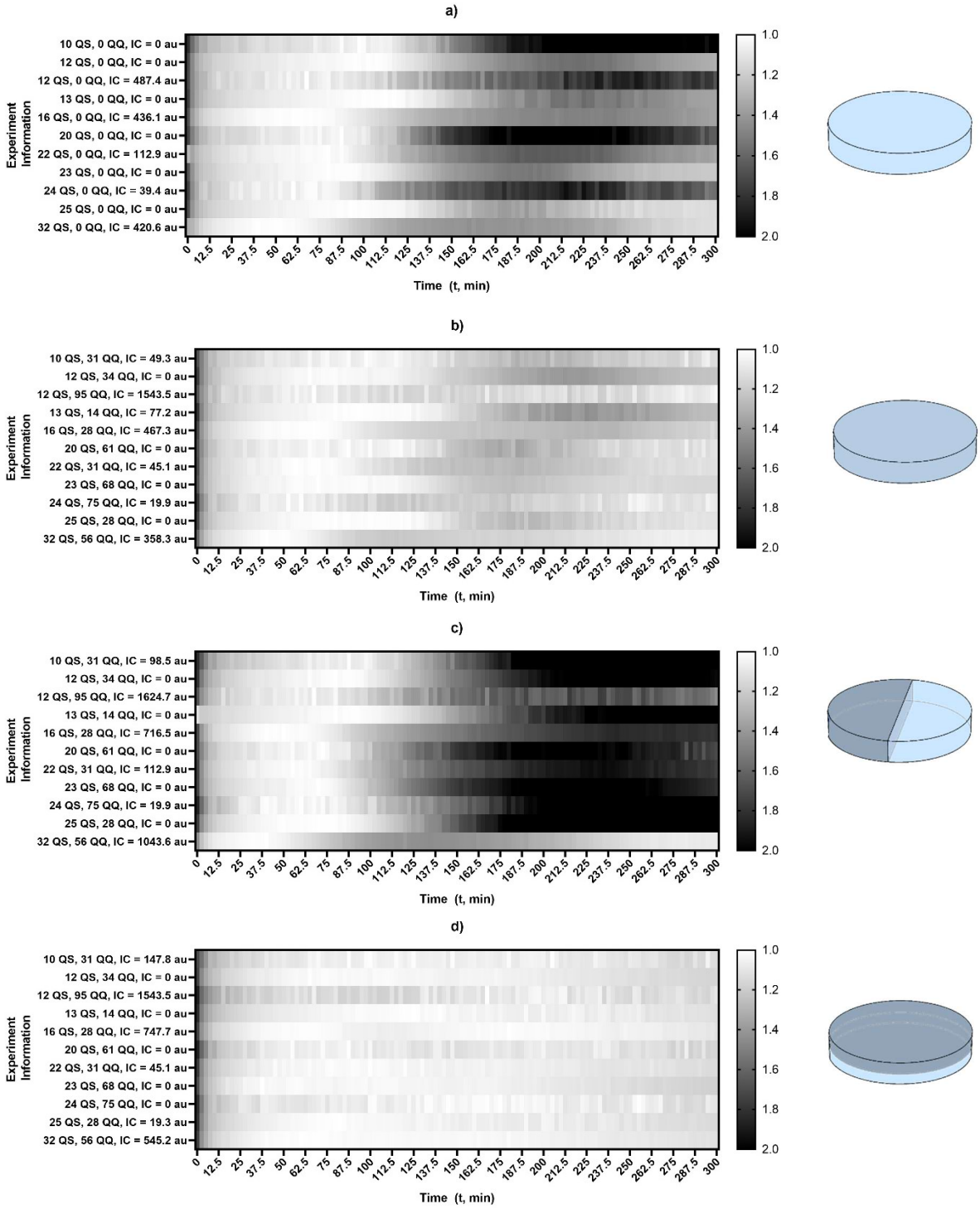

Fig. III.4. Heat maps of min-normalized fluorescence for different spatial arrangements in 0.6% agar. From top to bottom: (a) QS-only homogenous; (b) QS-QQ homogenous; (c) QS-QQ Split Bulk; (d) QS-QQ Split Layer. Arranged by increasing QS agents.

Both QS-QQ Split Layer and QS-QQ Homogeneous arrangements exhibit reduced QS-associated fluorescence signals compared to the other two arrangements. The heat maps provide a more organized view of the spectrum of geometric experiments. The initial fluorescence is noticeable in the first 5 minutes of each experiment well case. Note that not every QS-only case had strong fluorescence activation signals, even with higher QS agents. We believe this is an artifact of genetic variation in the QS circuit, and that it is more helpful to look at a larger picture with trends than at individually noisy cases. Analysis of the activation time and Area-Under-Curve (AUC) of the different arrangements allowed for quantitative comparison of the outcomes, as shown in **Figure III.5**.

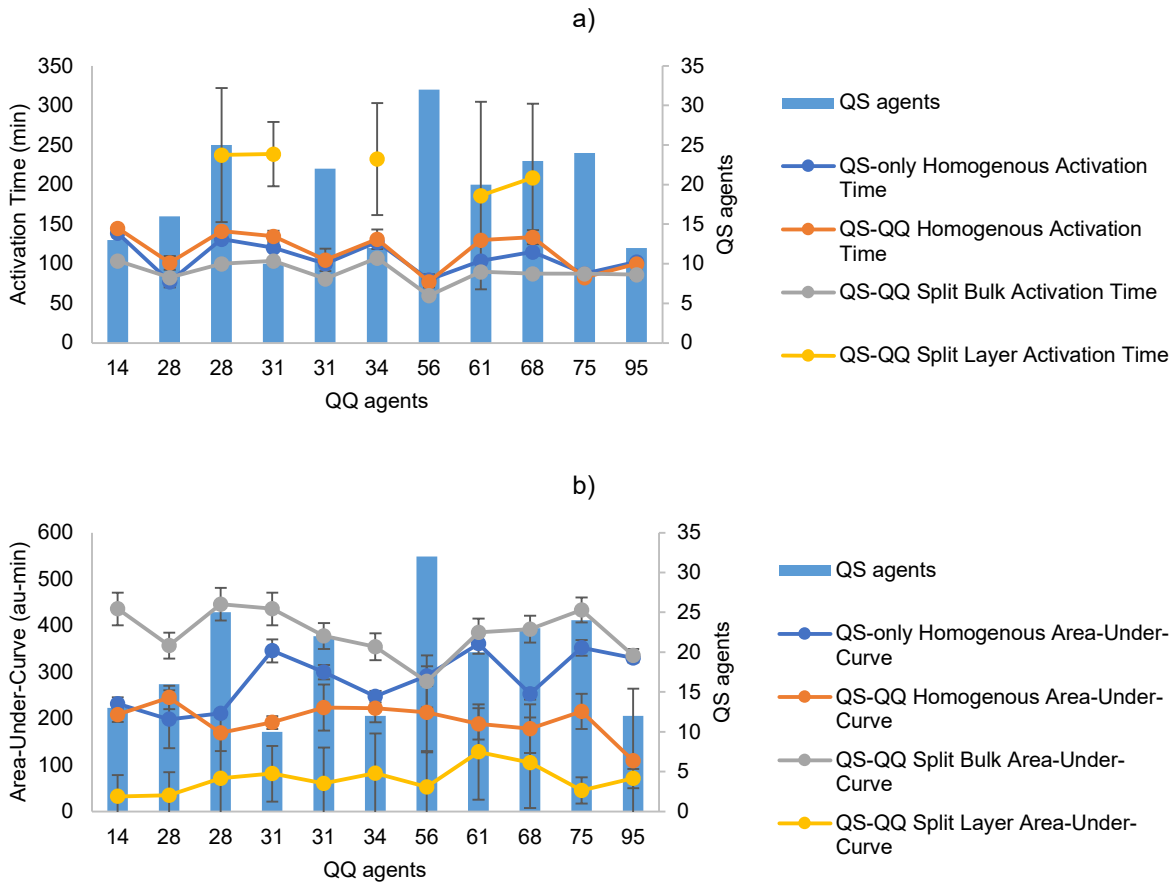

Fig. III.5. Min-normalized activation time (a) and Area-Under-Curve (AUC) (b) for different spatial arrangements of QS-QQ communities, organized by increasing QQ agents.

The AUC data from the experiments did not present a discernible pattern with the tested QQ/QS ratios or initial conditions. However, once again, there was a consistent AUC sequence: QS-QQ Split Bulk exhibited the strongest QS behavior, followed by QS-only Homogenous, then QS-QQ Homogenous, and finally QS-QQ Split Layer.

Although QS-QQ Split Layer and QS-QQ Homogenous setups displayed reduced QS activity due to QQ influence, the reasons for lower QS activity in the QS-QQ Split Layer compared to the QS-QQ Homogenous configuration remain speculative. Efforts were made to mitigate the influence of the agar-to-agar boundary in split wells on the fluorescent signal captured. For the split bulk configuration, where the boundary between QS and QQ agents was vertical, imaging was conducted several millimeters distance from the boundary to minimize its impact on light. However, in the split layer arrangement, with its horizontal boundary, some interference from the fluorescence signal was inevitable. To provide as clear a signal as possible, the QS bacteria were positioned at the bottom layer as opposed to the top layer to enhance imaging clarity under the microscope. It must be noted, however, that across the different spatial arrangement cases, the same z-position was imaged, to provide consistent treatment and data collection as much as possible.

Geometry itself, even for QS-only populations, does appear to influence activation time and AUC for different spatial arrangements. Figure III.6 below shows that even if only QS is observed and there is no QQ population present, Split Bulk still activates the fastest and has the highest AUC and Split Layer activates the slowest and has the lowest AUC.

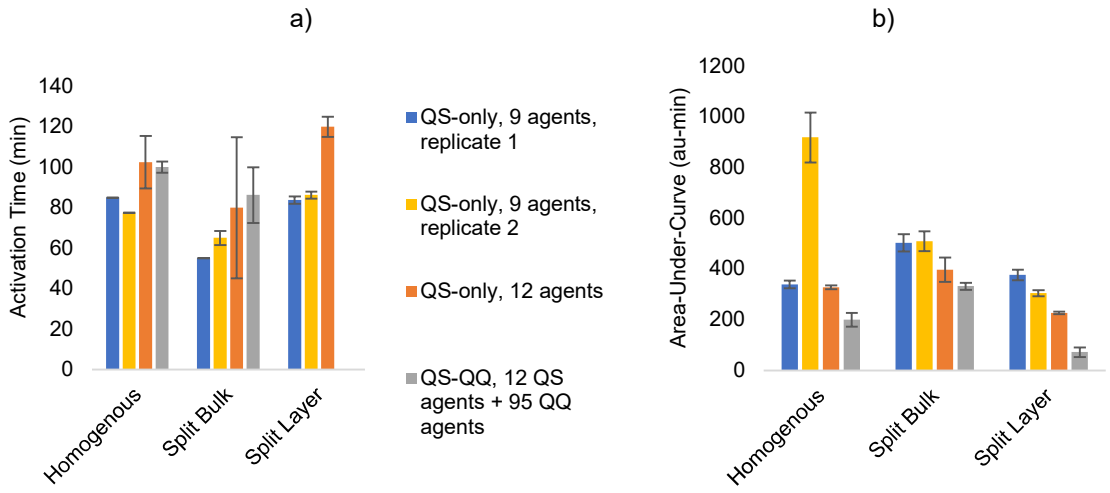

Fig. III.6. Activation time (a) and Area-Under-Curve (AUC) (b) for 0.6% agar spatial arrangements with QS-only wells.

As shown in **Figure III.6**, the limited (n= 3) QS-only experiments using 0.6% agar suggest that the geometry of the arrangement alone can influence the light signal, activation time, and AUC. This is likely due to difference in diffusion distance. However, these were preliminary tests only, and a more detailed study is needed to fully understand how these factors affect the fluorescent signal. A more detailed understanding of how QQ affects QS in different geometries for future research would benefit from control wells and QS-only wells of each geometry type. In our experiments, we only had QS-only wells of the homogenous arrangement.

In summary, contrary to initial assumptions, QQ agents did not significantly delay activation time; instead, the effect of QQ agents in a population appears to have manifested primarily as an attenuation of the magnitude of QS-associated fluorescence, as indicated by AUC measurements, which reflects the signal strength. The influence of QQ agents on the Area AUC appears more consistent than their impact on activation time (AT). However, it's plausible that AT could also be significantly affected by QQ agents, albeit under specific spatial conditions.

ii. 0.2% Agar Experiments with High Sensitivity (TIR=1262 au) QS strain

Toward our second goal and to characterize the nature of the effect of QQ on QS, we studied the data from homogenously mixed communities with different ratios and sizes of QS and QQ populations. **Figure III.7a** shows how QS-only experiments show higher and more sustained min-normalized fluorescence than QS-QQ experiments (**Fig. III.7b**), as expected. All the QS-only experiments in Fig. III.7a activated. However, a few cases with low-QS agents in the QS-QQ experiments (Fig. III.7b) did not activate at all within 300 minutes, even though counterpart QS-only experiments with the same number of QS agents activated within 200 minutes. While the delay of activation time with QS-QQ experiments does not appear to correlate trend-wise with QQ/QS ratio or QQ agent number, it did appear that for very small populations, activation time was increased for QS-QQ experiments compared to QS-only experiments.

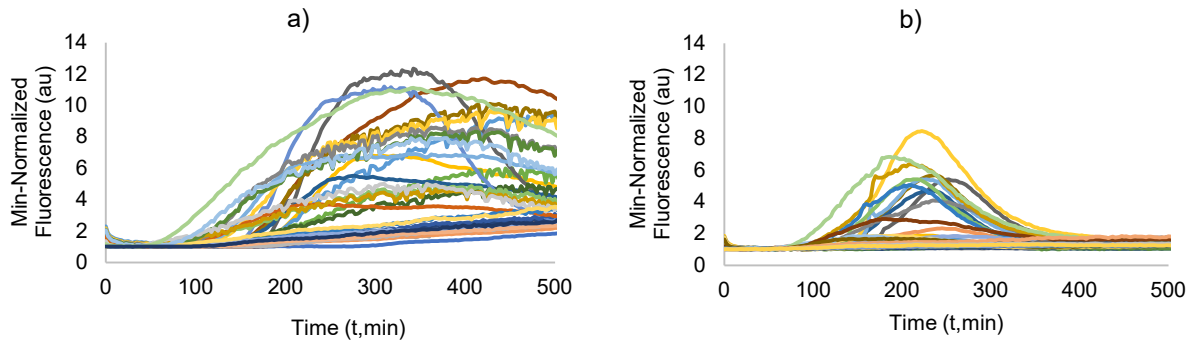

Fig. III.7. Min-normalized fluorescence curves where to achieve normalization, the mean-gray value at time t was divided by the minimum mean-gray value for the range t = [0, 300 min], yielding a dimensionless fluorescence parameter. (a) QS-only experiments; (b) QS-QQ experiments. Each curve represents one of the experiments shown in Figure III.8.

Qualitatively, visually inspecting the graphs in Figure III.7, QS-QQ experiments show fluorescence peaks at lower maximum fluorescence and overall fluorescence degrades faster than in QS-only experiments. Instead of a sigmoidal-shaped curve, the data for QS-QQ experiments take on more of a bell-shaped curve.

Once again, heat maps of min-normalized fluorescence intensity, shown in **Fig. III.8.**, provides another perspective. In experiments involving both QS and QQ (Fig. III.8b), the heat maps show patterns that are noticeably less intense and activated compared to those from QS-only experiments with similar numbers of QS agents and initial conditions (Fig. III.8a).

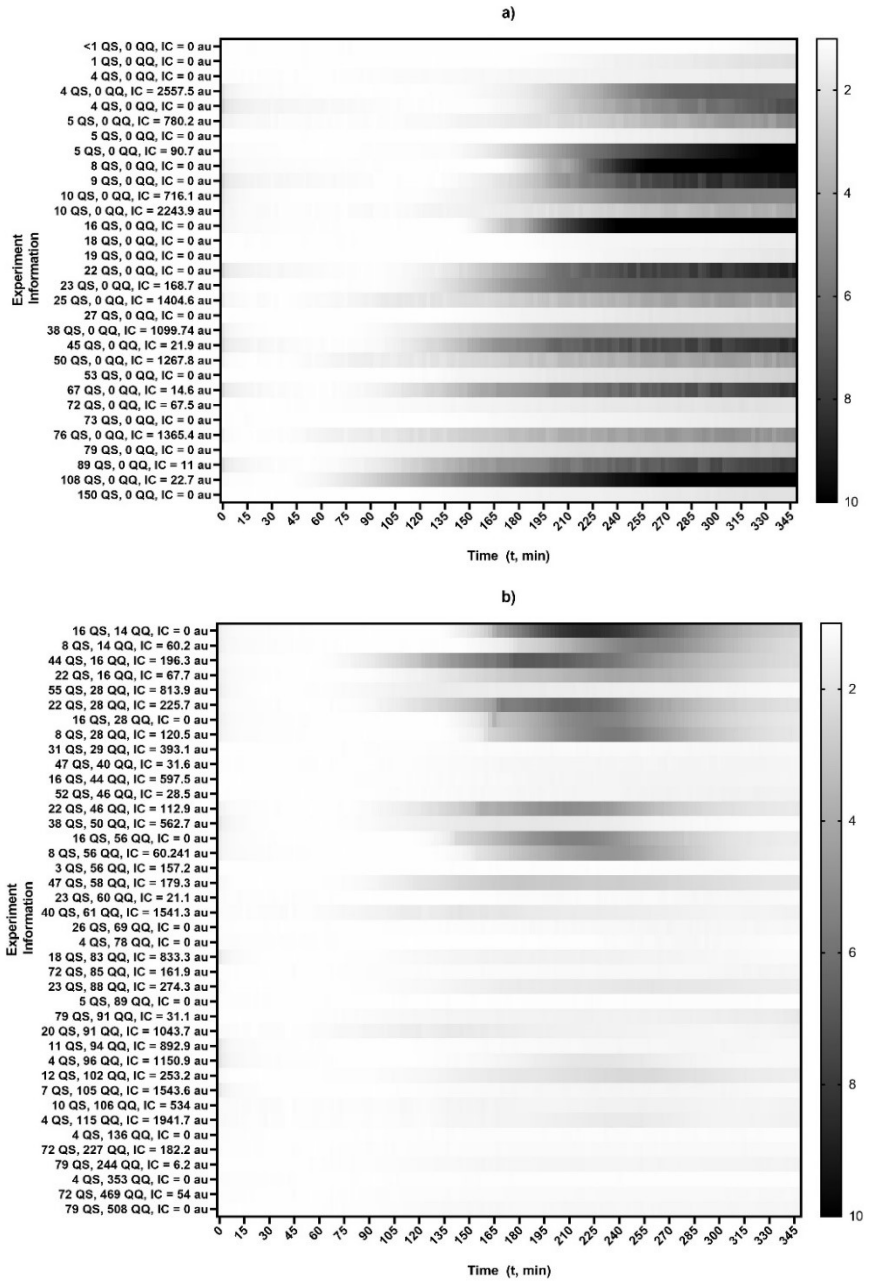

Fig. III.8. Heat map of min-normalized fluorescence for homogeneous 0.2% agar experiments with the Biobrick (TIR 1262 au) strain. (a) QS-only experiments, and (b) QS-QQ experiments in 0.2% agar homogenous wells. QS-only experiments are ordered by increasing QS agents; QS-QQ experiments are ordered by increasing QQ agents. Experiment information with the number of each type of agent as well as the initial condition (IC) shown on the left axis.

The heat maps simultaneously indicate activation time when the fluorescence starts rapidly increasing past a threshold, as well as the "strength" of fluorescence, which is associated and quantified through the area-under-curve (AUC) parameter, discussed later. One aspect of interest is that the experiments with "intense" fluorescence tend to also feature an initial fluorescence, and shallower curves tend to not feature this. While even control wells without any QS bacteria reporter strains also had an initial fluorescence, thus leading to our choice to not include it in AUC calculations, it is possible that that initial fluorescence is not entirely an artifact of autofluorescence of the media, and further study of this phenomenon might lead to more understanding and capability of quantifying QQ effect on QS. This factor was distinct but often associated with a non-zero initial condition of the type already used and quantified in these experiments. The current initial conditions referred to in this work, as discussed in the Methods (Section II.ii) are calculated by counting the number of initially fluorescent bacteria at the start of data collection. In some experiments, a vague hazy initial fluorescence was observed, but distinct bacteria could not necessarily be counted. It is recognized thus there was some type of initial condition in these experiments, but not one that we could quantify with our current method, and during the experimental phase we were not able to identify what was causing this discrepancy between experiments beyond the suspicion of microbubbles diffusing the light. Quantifying this initial fluorescence or further troubleshooting the fluorescence experimental setup and discrepancies would be an area of improvement for future work.

The initial conditions, as discussed here, are a measure of how much the population has already progressed toward QS activation when starting data collection. We organized activation time vs AUC analysis for low IC (0-200 au) and high IC (200+ au) populations.

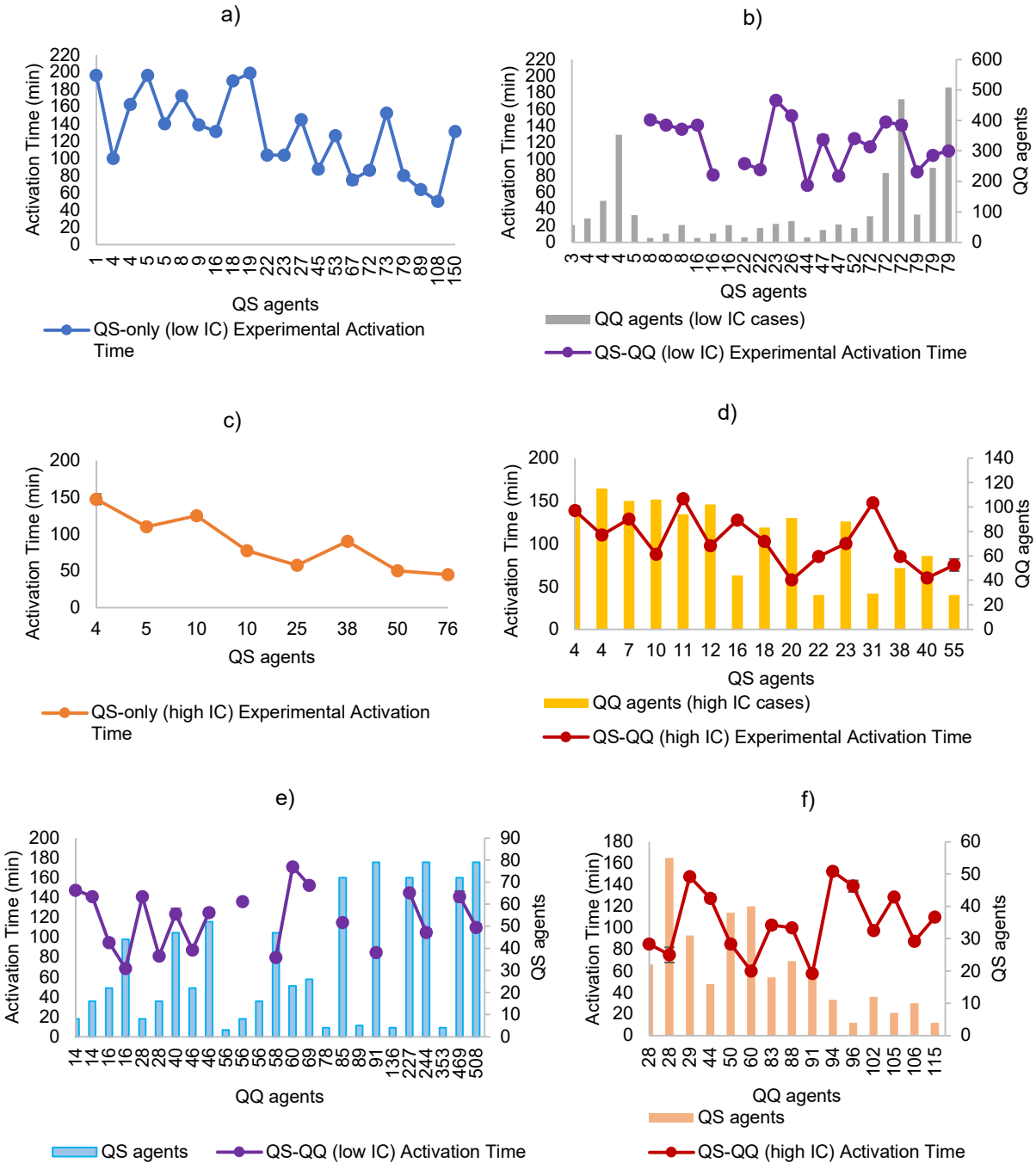

Fig. III.9. Comparison of Activation Time (AT) for 0.2% agar homogenous experiments. (a) QS-only and (b) QS-QQ AT for low initial conditions (0-200 au). (c) QS-only and (d) QS-QQ AT for high initial condition (IC) (200+ au). In (a)-(d) horizontal axis show increasing QS agents. (e) QS-QQ AT for low IC; (f) QS-QQ AT for high IC, arranged by increasing QQ agents.

High IC populations featured lower activation times compared to low IC populations, although this effect of IC was more noticeable with QS-only experiments (Fig III.9a) compared to QS-QQ experiments (Figure III.9b). This makes intuitive sense and agrees with the previous work of Leaman *et al*. (2018). There is a bigger difference between the activation time of small QS-only populations and large QS-only populations than small QS-QQ populations and large QS-QQ populations.

It was expected that the presence of QQ agents would lead to a delay in activation time compared to QS-only experiments. However, the experimental activation time for QS-only communities compared to that of QS-QQ communities with similar quantities of QS agents appeared to be equivalent. This similarity suggests that the presence of QQ bacteria, at least in the concentrations and ratios we evaluated for the 1262 TIR strain, does not significantly alter the activation timing in these communities, regardless of whether the initial conditions are low or high. For both QS-only and QS-QQ communities, activation time decreased for higher QS agents. When experiments cases are organized by increasing QQ agents (Figure III.9e and III.9f), activation time followed the opposite trends of QS agent number. Figure III.10 shows equivalent graphs and trends, but for AUC.

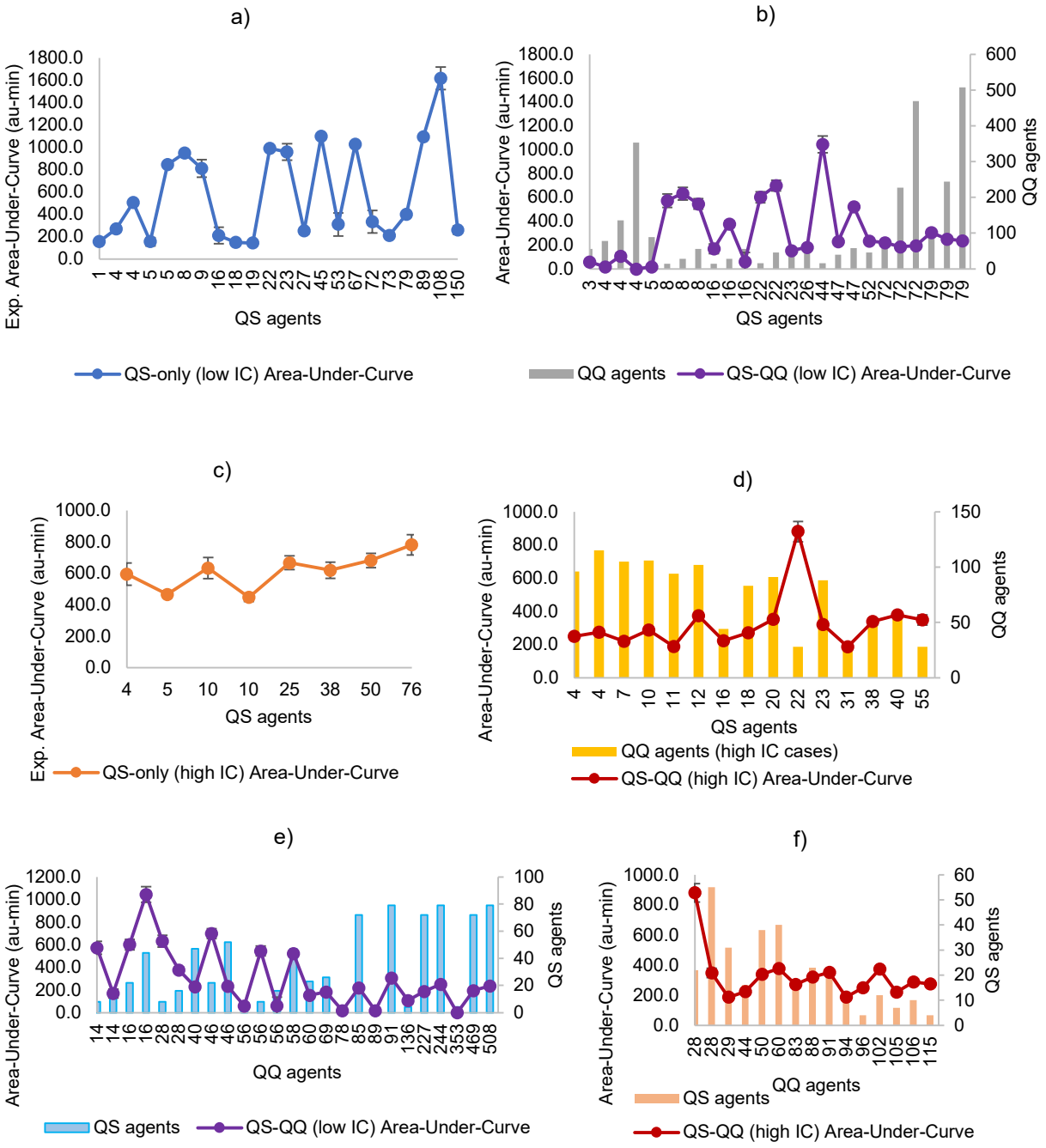

Fig. III.10. Comparison of area-under-curve (AUC) for 0.2% agar homogenous experiments. (a) QS-only and (b) QS-QQ AUC for low initial conditions (0-200 au). (c) QS-only and (d) QS-QQ AUC for high initial condition (IC) (200+ au). In (a)-(d) horizontal axis show increasing QS agents. (e) QS-QQ AUC for low IC; (f) QS-QQ AUC for high IC, arranged by increasing QQ agents.

The AUC results are modestly influenced by both the presence of QQ agents and the initial QS conditions. Though there is fluctuation in the data, low-IC QS-only appeared more likely to exhibit higher AUC values, which makes intuitive sense. However, this pattern becomes less distinct when comparing low-IC QS-QQ with high-IC QS-QQ experiments, implying that the presence of QQ bacteria diminishes the advantage typically conferred by higher initial conditions in promoting strong QS behavior. In other words, the QQ factor seems to level the playing field, making high IC less beneficial in scenarios where QS is countered by QQ mechanisms.

The AUC was a better measure of the influence of QQ on QS communities. The AUC, while very noisy, does appear to increase with the increasing number of QS agents, as in Figure III.10.c. In contrast, as shown in Fig. III.10e, AUC trends downward as the number of QQ agents increased (x-axis). It takes an expected opposite trend of activation time in Figure III.9, and yet appears to more cleanly follow a trend of increasing with QS agents and decreasing with increasing QQ agents. These trends are further supported by experiments with other strains, as discussed in the next subsection.

iii. 0.2% Agar Experiments with Low Sensitivity (TIR=99 and 30 au) QS strains

Experiments with strains featuring lower basal and upregulated AHL production rates were also done to explore the effect of lower QS circuit sensitivity (i.e., same bacteria cell number density exhibits a later activation time) to gain more insight into what is being affected by QQ. As with the TIR 1262 au strain, heat maps, activation time, and AUC results are presented in this subsection for two alternate strains with less sensitive QS circuits.

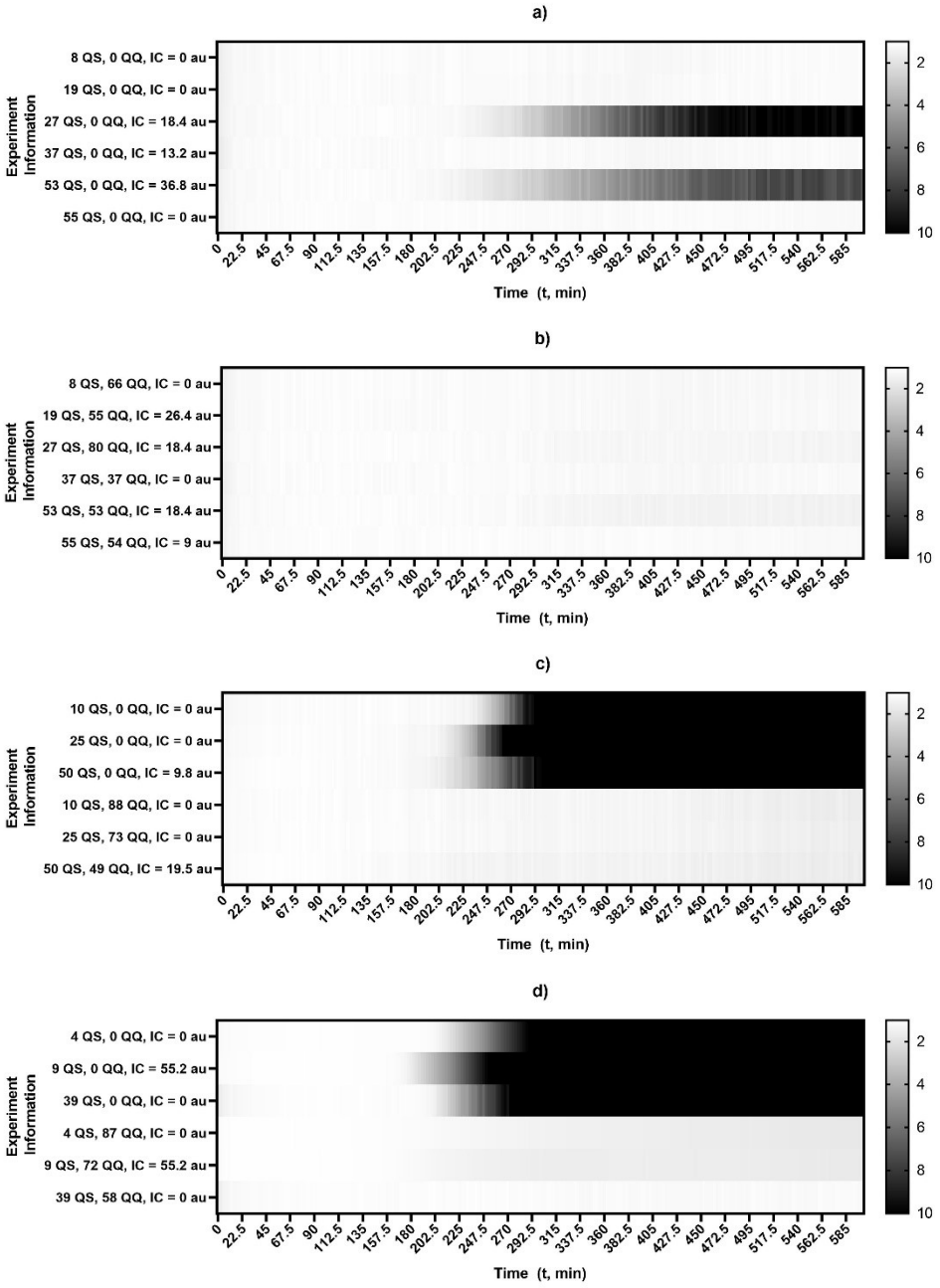

Fig. III.11. Heat map of min-normalized fluorescence for homogeneous 0.2% agar experiments with the 30 and 99 au RBS constructs. Subfigures: (a) RBS 30 au construct, single *luxI*, QS-only; (b) RBS 30 au construct, single *luxI*, QS-QQ; (c) RBS 30 au construct, double *luxI*, QS-only and QS-QQ; (d) RBS 99 au construct, single *luxI*, QS-only and QS-QQ.

Heat maps in **Figure III.11**, clearly show that for these lower sensitivity strains, compared to the BioBrick (1262 au) construct (Fig. III.8), the presence of QQ has the potential to drastically affect the heat maps. While not all QS-only experiments had strong QS heat maps, all the QS-QQ cases showed shallower heat maps.

Figure III.12 shows the activation time and AUC trends for these strains.

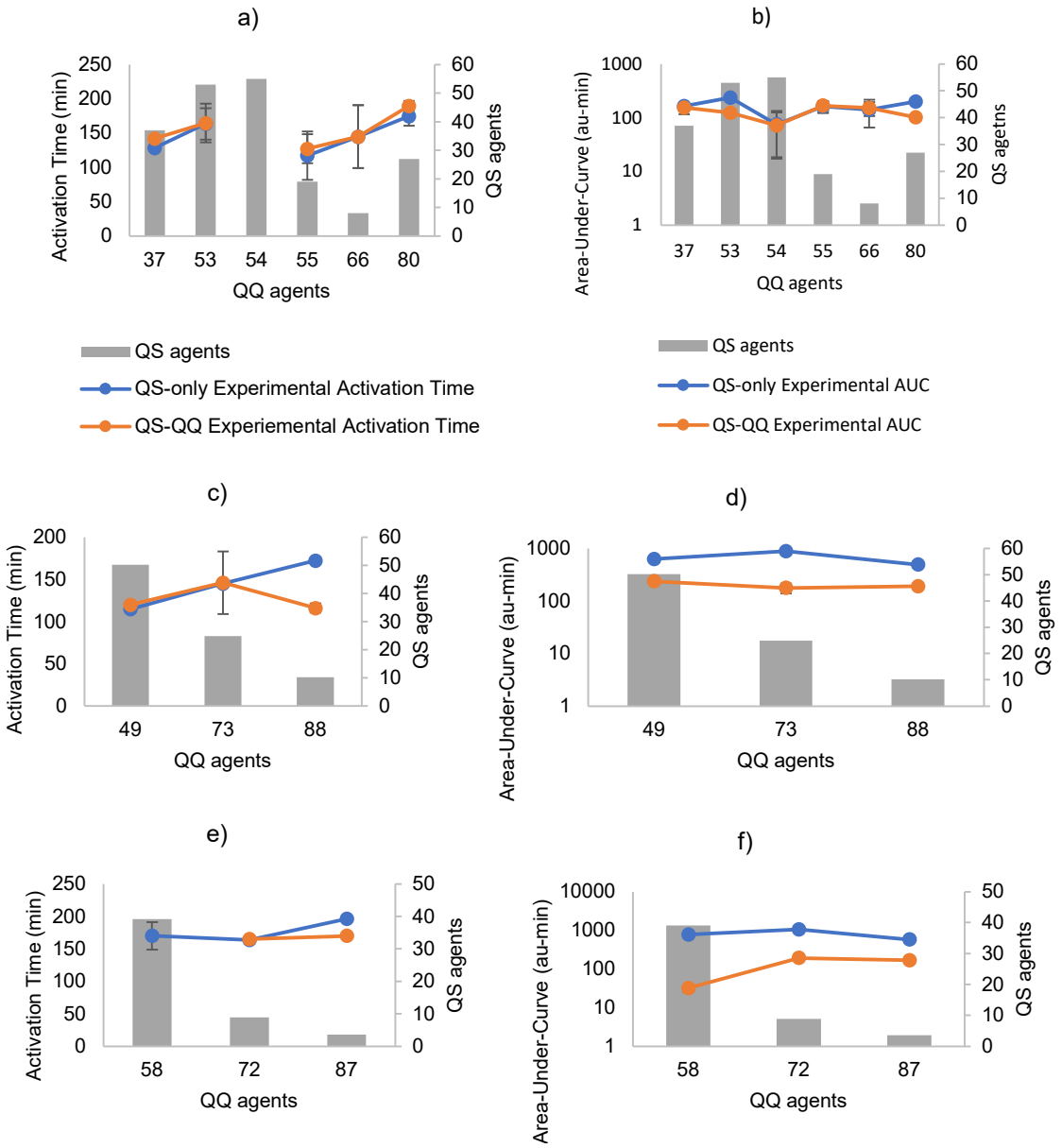

Fig. III.12. Comparison of Activation Time (a) and (b) Area-Under-Curve (AUC) for 0.2% agar homogenous experiments with RBS construct TIR 30 au, single *luxI*. Activation time (c) and AUC (d) for RBS construct TIR 30 au, double *luxI*. Activation time (e) and AUC (f) for TIR 99 au, single *luxI*.

The AUC values of QS-QQ communities are almost always lower than in QS-only setups, but activation times, on the other hand, do not show the same trend and appears less sensitive to changes in the number of QQ agents present. As a result, we conclude that AUC is a more informative and reliable parameter and captures the influence of QQ agents more effectively. .

IV. Chapter 4: Results and Discussion of the Computational Modeling Validation and Predictions

As mentioned previously, the third aim of this thesis was to adapt our previously developed QS model to describe the QS behavior of bacteria in agar and experimentally validate the QS-QQ theoretical model for different population sizes and ratios of QS and QQ agents in mixed communities.

Sensitivity to AHL and agent grid size, growth, and speed were studied. The model basal and upregulated production of AHL parameters for QS were optimized for our media, as well as the AHL upregulation threshold. Growth models were developed based on experimental observations, and velocity inputs were also taken from experiments.

The model was found most sensitive to growth among other input parameters, and uncertainty and inaccuracy in growth are anticipated to be the leading areas in need of improvement in future work.

Once the model's sensitivity or lack of sensitivity to input parameters was established, the AHL upregulation threshold and rates of AHL production were optimized, and the model was validated against experimental conditions. After optimization, the model was applied to QS-QQ experiments to study how its predictions compared to key outcomes like activation time and area-under-curve (AUC).

It was observed that the model followed experimental trends with activation time and AUC. An increase in QS agent numbers and higher initial conditions were associated with a reduction in activation time and an elevation in AUC values. Higher QQ agents numbers were associated with a reduction of AUC and/or increase of activation time. It appeared that when comparing QS-QQ experiments to other QS-QQ experiments, increasing the number of QQ agents interacting with a set number of QS agents tended to result in an increased activation time. Conversely, increasing the QS agents interacting with a consistent number of QQ agents resulted in the activation time decreasing. However, it could not be consistently said that QS-QQ experiments had higher activation times than QS-only experiments. Indeed, sometimes QS-QQ experiments activated earlier than QS-only experiments, perhaps as a result of community interactions of the QS agents with the QQ agents.

i. Growth Modeling

In this subsection, we discuss the characterization of growth in our experiments and the growth model used as inputs to the simulation. **Figure IV.1** shows the experimental data for four different QS-only experiments with low agent count.

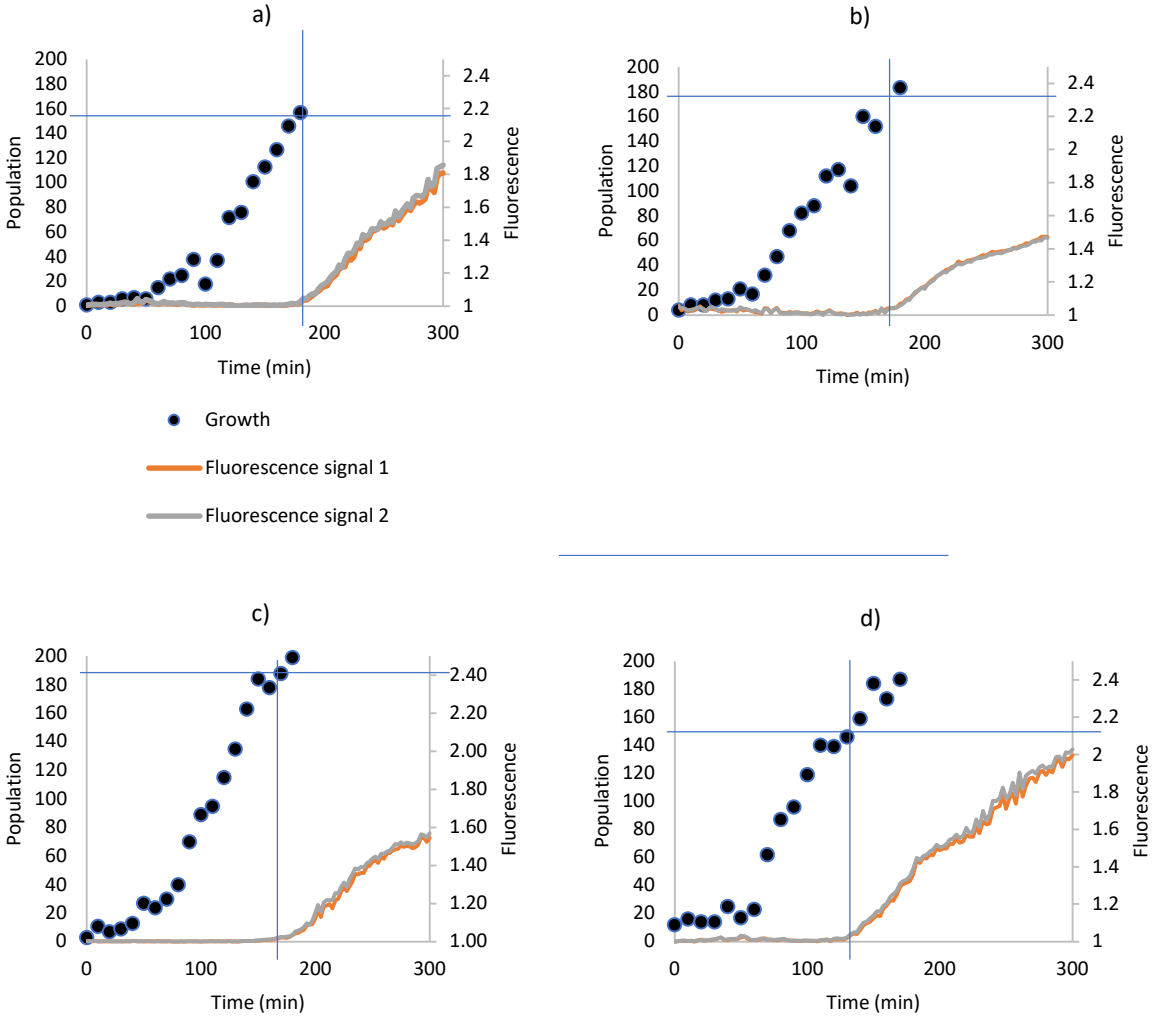

Fig. IV.1. Growth and fluorescence curves for small populations of $OD_{600} < 0.03$. (a) QS $OD_{600} = 0.0054$ or 2.71E6 CFU/mL, initial condition (IC) = 0 au; (b) QS $OD_{600} = 0.0186$ or 9.29E6 CFU/mL, IC = 0 au; (c) QS $OD_{600} = 0.0191$ or 9.55E6 CFU/mL, IC = 0 au; (d) QS $OD_{600} = 0.02705$ or 1.35E7 CFU/mL, IC = 0 au. Raw bacterium counts within a 400 µm × 300 µm imaged area shown on y-axis (left axis). "Fluorescent signal 1" is the signal from z = 0 µm; "Fluorescent signal 2" is the signal from z = 30 µm.

Generally, for smaller populations, the fluorescent signal did not rise until at least 130 minutes (Figure IV.1). Thus, growth in simulations for smaller populations was an extrapolation of behavior when modeling beyond 150 minutes. Interestingly, activation time consistently occurred when the population reached around 150-180 bacterium within a 400×300 μm^2field, corresponding to approximately 1800-2200 agents in the simulation.

Figure IV.2 shows approximate fittings of the normalized populations for small-population experiments, where a parabolic fit appears more appropriate than a linear fit.

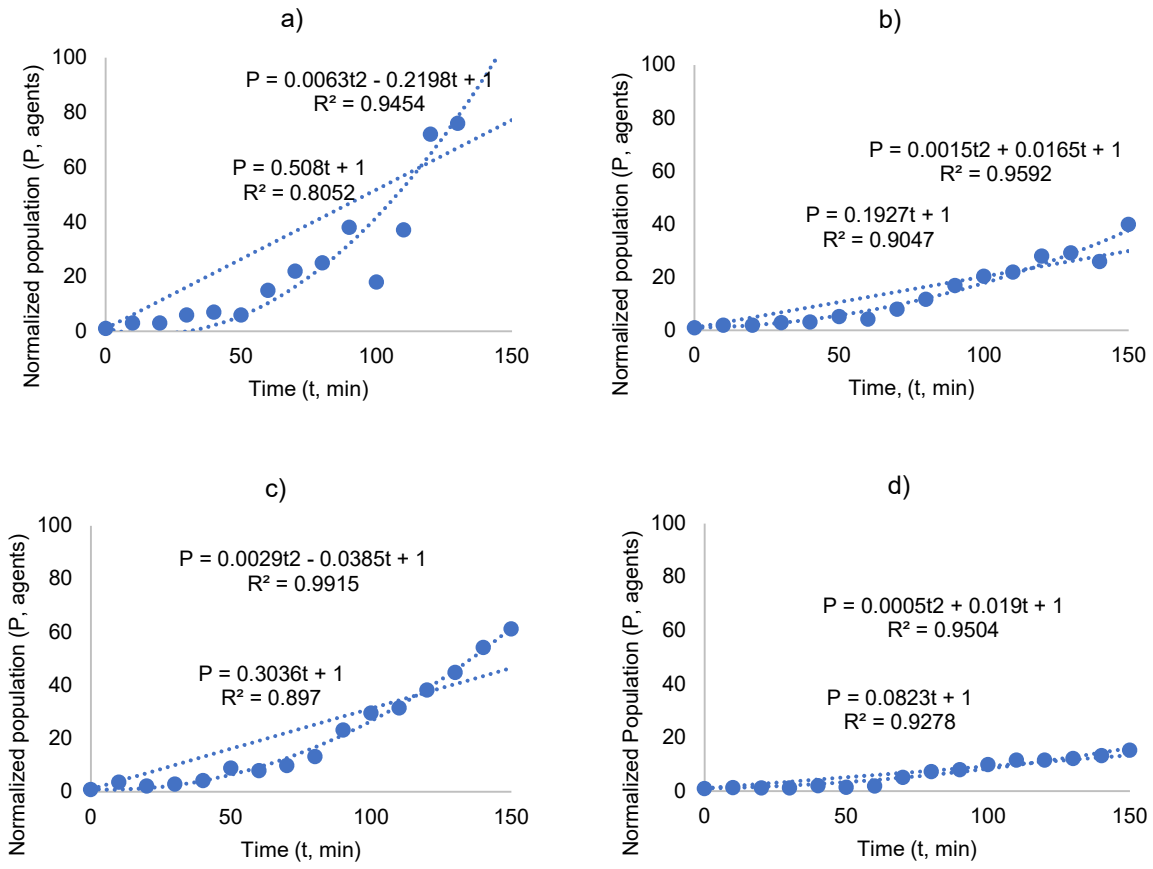

Fig. IV.2. Growth curves for small populations of OD_{600} < 0.03. Linear and parabolic fitted curves shown on graphs, with respective R^2 values. (a) QS OD_{600} = 0.0054 or 2.71E6 CFU/mL, initial condition (IC) = 0 au; (b) QS OD_{600} = 0.0186 or 9.29E6 CFU/mL, IC = 0 au; (c) QS OD_{600} = 0.0191 or 9.55E6 CFU/mL, IC = 0 au; (d) QS OD_{600} = 0.02705 or 1.35E7 CFU/mL, IC = 0 au. Experimental population is normalized to initial population count at t = 0.

It should be noted that for increasingly large populations, a parabolic fit appeared less and less suitable compared to a linear fit, and the linear fit began to outperform the parabolic fit.

Figures IV.3 and **IV.4** show counterpart graphs for larger populations.

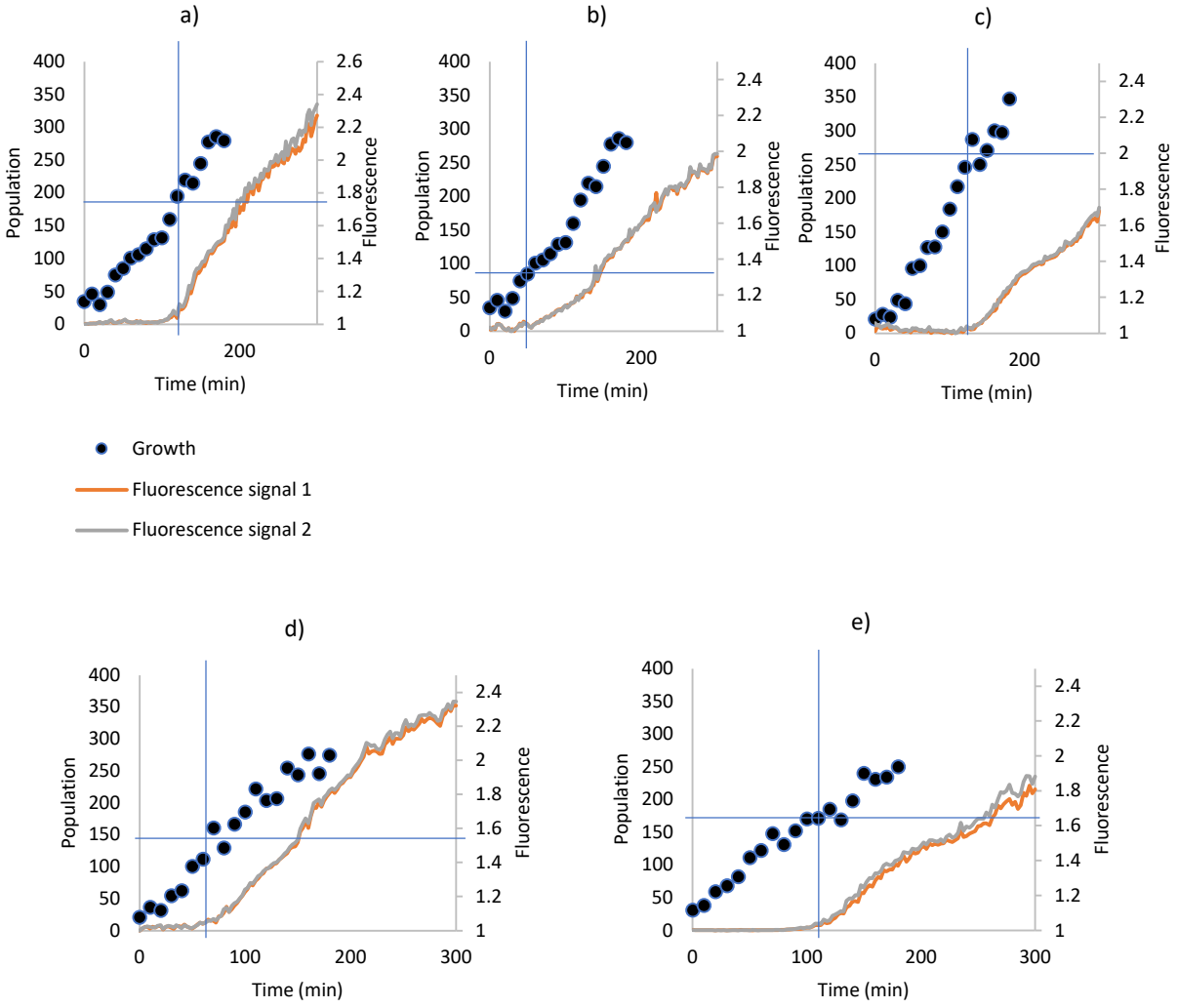

Fig. IV.3. Growth and fluorescence curves for large populations of $OD_{600} > 0.03$. (a) QS $OD_{600} = 0.054$ or 2.71E7 CFU/mL, initial condition (IC) = 0 au; (b) QS $OD_{600} = 0.0741$ or 3.71E7 CFU/mL, IC = 67.48 au; (c) QS $OD_{600} = 0.0743$ or 3.72E7 CFU/mL, IC = 0 au; (d) QS $OD_{600} = 0.0804$ or 4.02E7 CFU/mL, IC = 0 au; (e) QS $OD_{600} = 0.153$ or 7.67E7 CFU/mL, IC = 0 au. Raw bacterium counts within a 400 µm × 300 µm imaged area shown on y-axis (left axis). "Fluorescent signal 1" is the signal from z = 0 µm; "Fluorescent signal 2" is the signal from z = 30 µm.

For larger populations with more linear growth, the fluorescent signal rose earlier. Because there was more of an overlap of the time period when the population was activated and when we had experimental data for, we have more confidence with modeling larger populations.

With the larger populations, once again, fluorescence rise tended to correlate with raw bacterium count between 100-200, or approximately 150 agents, same as with the smaller populations. This is expected, as a certain consistent density must be reached to achieve QS. It is encouraging that the density or concentration threshold appears generally to be the same regardless of initial population size. Due to difficulties characterizing community growth and *Salmonella* with the method we used in this project (discussed later in this section), the exploration of if or how this density threshold changes with the presence of QQ would be an interesting area to explore in future work but was out of scope for this thesis.

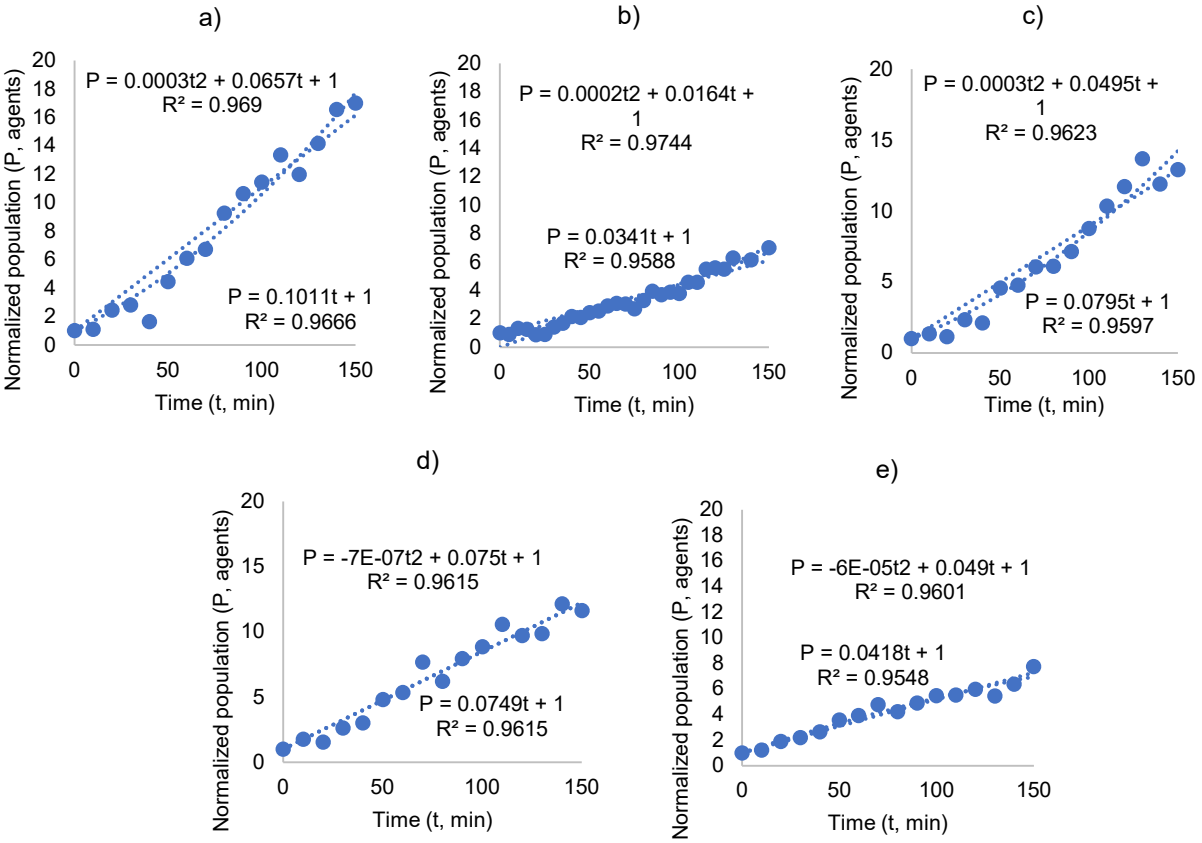

Fig. IV.4. Growth curves for large populations of $OD_{600} > 0.03$. Linear and parabolic fitted curves shown on graphs, with respective R^2 values. (a) QS $OD_{600} = 0.054$ or 2.71E7 CFU/mL, initial condition (IC) = 0 au; (b) QS $OD_{600} = 0.0741$ or 3.71E7 CFU/mL, IC = 67.48 au; (c) QS $OD_{600} = 0.0743$ or 3.72E7 CFU/mL, IC = 0 au; (d) QS $OD_{600} = 0.0804$ or 4.02E7 CFU/mL, IC = 0 au; (e) QS $OD_{600} = 0.153$ or 7.67E7 CFU/mL, IC = 0 au. Experimental population normalized to initial population at t = 0.

When the initial population sizes were larger, linear models proved to be more predictive than parabolic models as initial OD increased. The observed divergence in growth patterns between smaller and larger populations indicated the requirement for at least two distinct growth curves to accurately reflect the varying dynamics.

To simplify the growth model input, the growth curves were subjected to averaging for the two categorized population groups (designated as 'small' and 'large'), and various range intervals were evaluated to determine the most appropriate fits, as shown below in **Figure IV.5**.

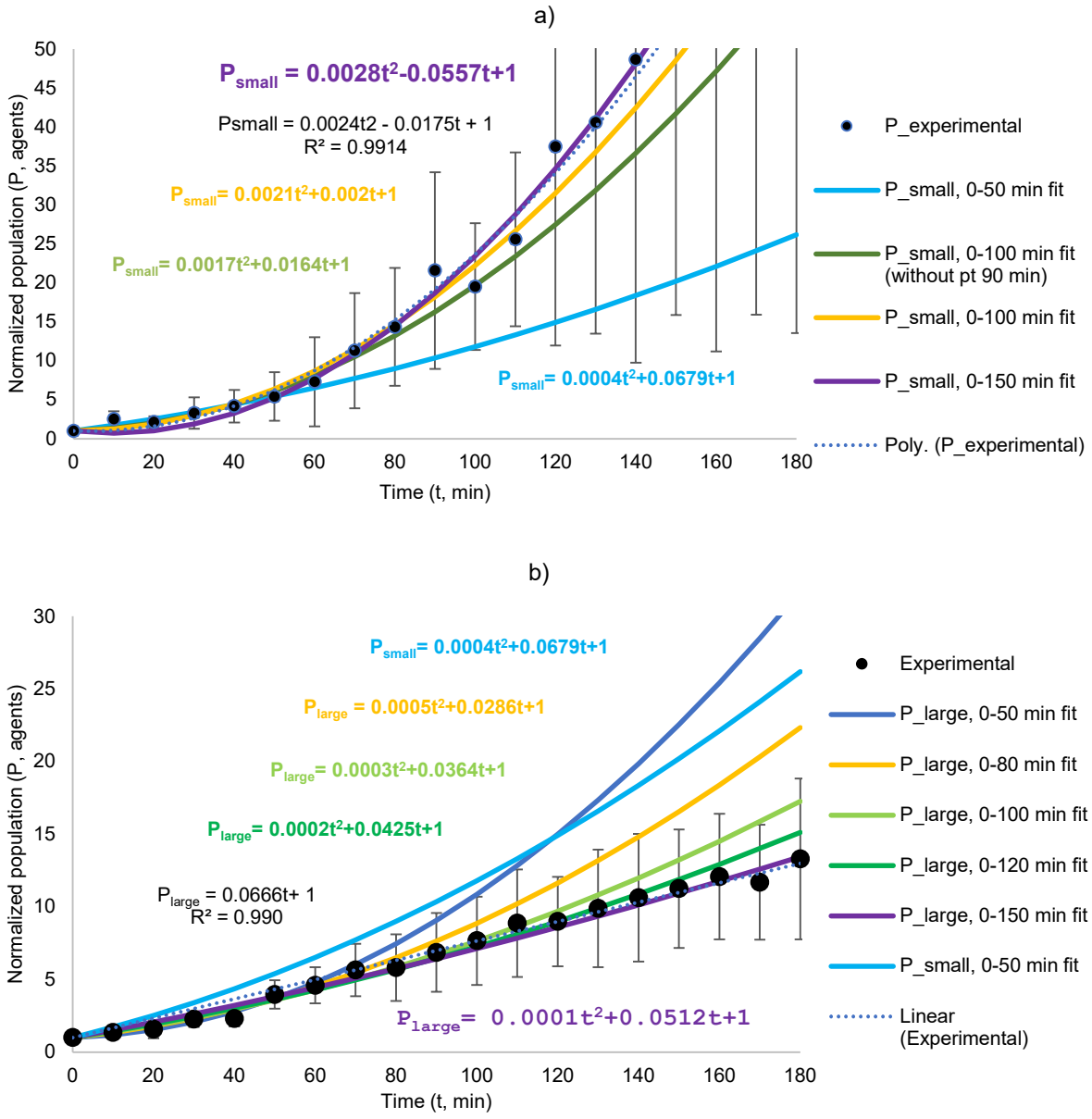

Fig. IV.5. Average growth curves for populations for (a) $OD_{600} < 0.03$ and (b) $OD_{600} > 0.03$ (bottom) showing average and standard deviation for experimental growth and models based on different fitting intervals. Experimental population is normalized to initial population count at t = 0. Selected models, discussed below, shown in purple. Note that (b) includes a test case from (a) where $P_{small} = 0.004t\text{^}2 + 0.0679t + 1$ to show how even the small population growth model with minimal curvature did not agree well, when applied to larger populations.

We sought a growth equation applicable to both large and small bacterial populations. However, a universal model that accurately represented both scenarios was not identified. A

P_{small} fit is applied in Figure **IV.5b** (blue curve) to show how deviant the small population model is when applied to larger population data.

For larger populations, a linear model fitting to the full 180-minute duration of experimental growth data was undesirable because it tended to overestimate growth during the initial 20-40 minutes. To address this discrepancy, a parabolic fit with minimal curvature was employed instead for the larger population modeling. It could not be said that initial growth was more important than later growth; rather, both were important. Our objective to accurately model the area-under-curve (AUC) parameter for both initial and later stages necessitated precise growth modeling at all time points as much as possible. Therefore, for both population bins, we aimed to employ a respective model that accurately reflected the experimental growth data from early to later stages.

Two distinct growth models were used:

18) $$P_{large} = 0.0001\,t^2 + 0.0512\,t + 1$$

for larger populations, and

19) $$P_{small} = 0.0028\,t^2 - 0.0557\,t + 1$$

for smaller populations, where *t* is time. This bifurcated modeling approach allowed for a more precise and nuanced analysis of bacterial growth dynamics across different population scales than previous iterations of the model and was an important step toward being able to model larger ranges of agent numbers. The necessity for an alternative growth modeling approach different from Leaman *et al.*'s method was anticipated due to the different experimental conditions and media utilized in this research.

The decision to utilize only two distinct categories for population sizes was primarily driven by the limited number of growth experiments conducted. Further research should consider incorporating a greater granularity of population sizes to enhance the precision of the models. Moreover, future research could potentially benefit from a more sophisticated growth model that dynamically adjusts according to population size. This could take the form of applying a different equation for growth as population size passed various checkpoints. The development of such a model was deemed beyond the scope of this study, but would be a worthwhile

endeavor, considering growth rates have significant effects on QS Activation Time (AT) and Area-Under-Curve (AUC) results, especially for small populations.

Once again, it is important to also acknowledge that due to crowding effects in the experiment, acquiring reliable growth data beyond 150 minutes was difficult, and it was generally unfeasible beyond 180 minutes. Consequently, for activation times and AUC modeling extending past 180 minutes, the confidence in the accuracy of the growth model diminishes. At later time points beyond 150 minutes, our growth models are best regarded as approximate estimations. Nevertheless, subsequent sensitivity analysis, which is elaborated upon later in this chapter, revealed that variations in the leading term of parabolic growth models, while significantly influencing the activation times of smaller populations, had a less pronounced impact on larger populations. This finding aligns with the understanding earlier established that smaller populations, which typically activate later, may not conform to the growth model in the latter stages of the experiment.

Furthermore, the comparatively large QQ populations made it infeasible to conduct an in-depth growth analysis of *Salmonella* analogous to that of *E. coli*. As mentioned earlier, past a certain population, it was difficult to confidently count QQ agents as crowding and clumping became a more noticeable effect. To validate our QS-QQ experiments, we would need a model of QQ growth for higher agent populations, which our existing methods of growth measures precluded. While steps could have been made toward such a model, the constrained timeframe of the experimental phase limited the practicality and priority of undertaking the comprehensive series of growth experiments for *Salmonella* necessary for a model that would reliably extend to higher QQ agent populations. Consequently, the focus was shifted to prioritize experiments on the growth curves of *E. coli*. Future investigations would benefit from elaborating on the QQ growth model or alternatively engineering QQ *E. coli* strain that are more likely to parallel the growth characteristics of the quorum sensing (QS) *E. coli* strain. It is important to note that metabolic burdens, such as fluorescence production or alterations in growth due to the activation of quorum sensing, could still result in disparities between QS and QQ strains. Furthermore, it should also be considered that growth dynamics may shift in community interactions, even when individual populations are analyzed at varying sizes, particularly when the strain under observation is not in isolation. Challenges such as the

attenuation of the fluorescent signal and the difficulty in distinguishing individual bacteria in our agar-based experiments complicated the investigation of community growth rates.

Lastly, the possibility of growth plateauing should also be considered. The bacterial populations first go through a phase of rapid growth, followed by a subsequent slowdown. This is a well-known phenomenon in biological systems where growth is eventually limited by resource availability. Our focus was on fluorescence within the initial 300 minutes, so the concerns regarding starvation and reduced growth rates were less significant, based on our observations of not seeing significant starvation indicators before 300 minutes.

The focus of this study was more on gaining a qualitative understanding of the impact of quorum quenching on quorum sensing rather than achieving a perfect quantitative match between the model and the experimental data. Our primary objective was to validate general trends rather than to ensure exact numerical alignment with experimental outcomes. We do, however, believe that limitations with our growth modeling are a leading cause of the existing differences in the outcomes of the model compared to experiments.

ii. Motility Modeling

We briefly discuss motility here, as it is an input to the model as well. Motility is more important if net chemotaxis is present, which was not in our experiments. Figure IV.6 shows the run speeds from sampled bacteria in various population sizes.

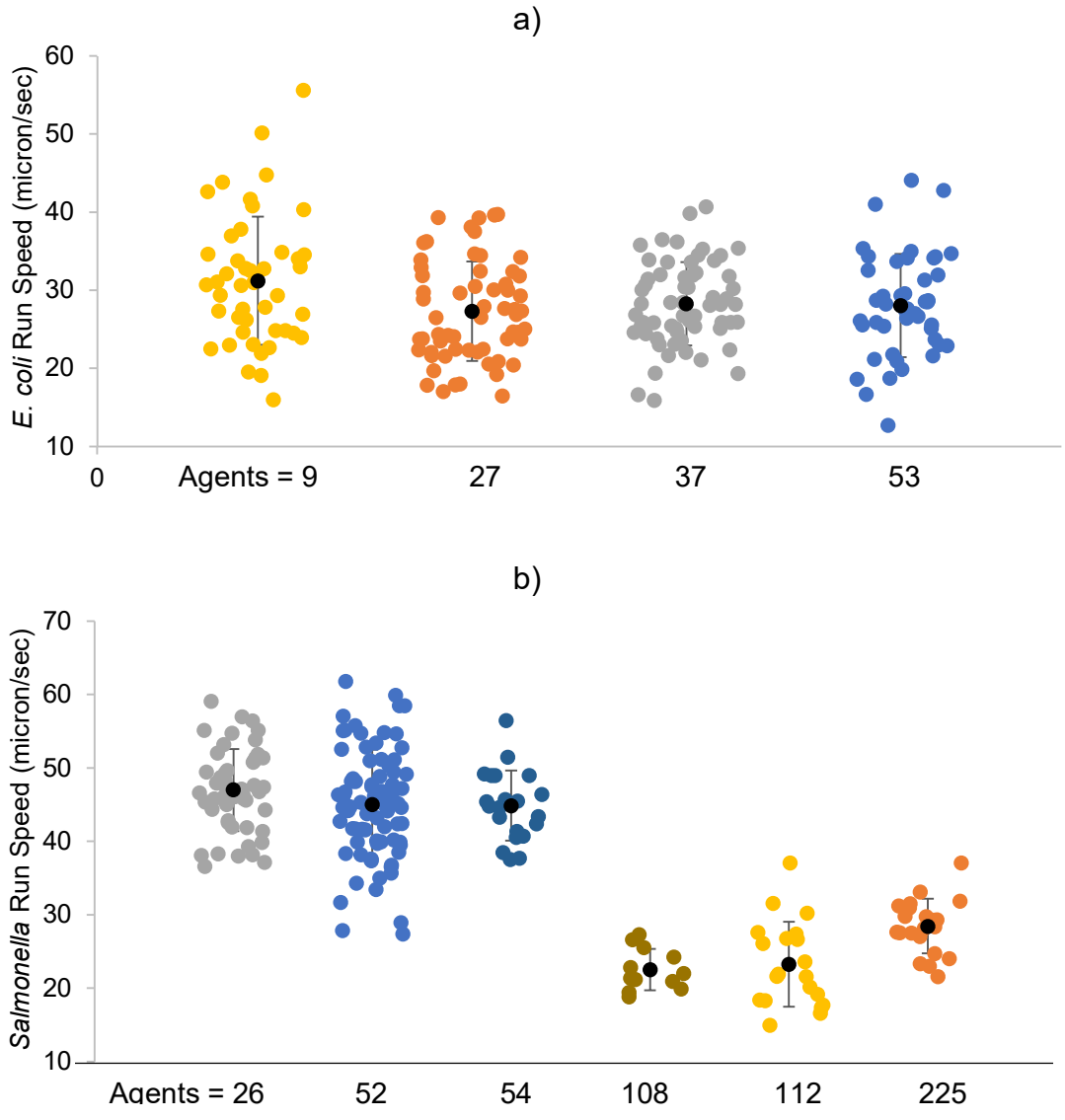

Fig. IV.6. Motility run speeds for (a) *E. coli MG1655* BioBrick QS construct and (b) *S.* Tm 14028 QQ construct. Number of agents are shown on horizontal axis. Average speed values are shown by black dots. Error bars represent standard deviation values.

In **Figure IV.6**, it is evident that elevated OD_{600} readings 100 agents (equivalent count in the simulation) resulted in diminished velocity for QQ agents. This reduction in speed can be attributed to factors such as overcrowding and potential nutrient scarcity. For modeling purposes, average speeds were considered: 28.6 μm/s for *E. coli* and 33.5 μm/s for *Salmonella*. These averages were subsequently integrated into the computational model for the 0.2% agar cases. For 0.6% agar experiments, motility was arrested by the high agar concentration.

iii. Sensitivity Analysis: Effects of Growth, Domain size, Agent Size, and AHL Grid Size

In this section, we consider the sensitivity and response of the model to input parameters such number of each agent, agent size, AHL grid size, and the intracellular GFP concentration required to consider QS activation. Figures **IV.7a** and **IV.7b** respectively show how the activation time and AUC compare between simulations with and without initial conditions and changing number of QS and QQ agents. Unless otherwise specified, all sensitivity tests were done with the large growth model.

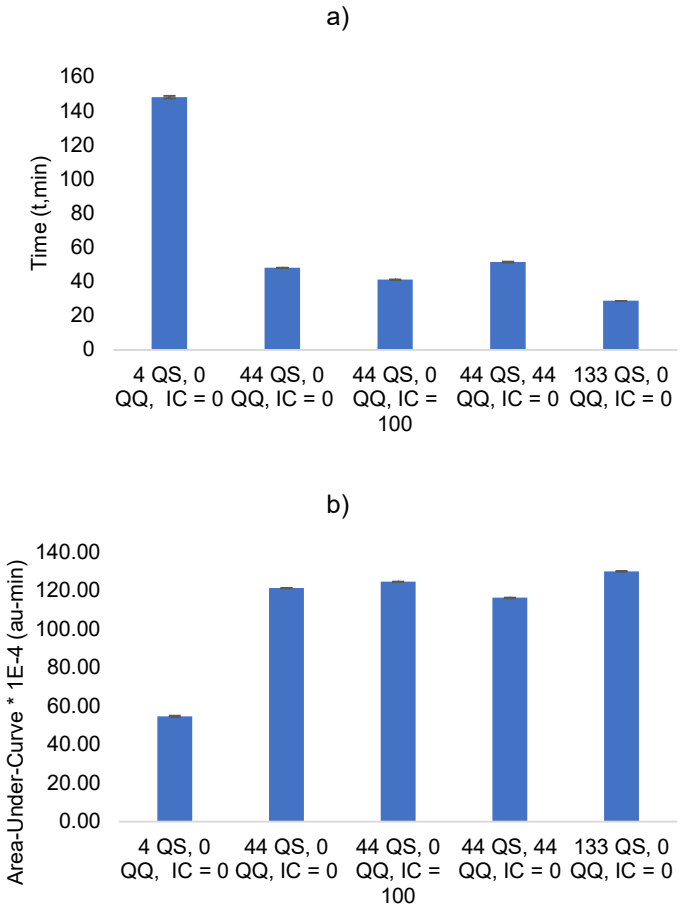

Fig. IV.7. Effect of quorum quenching (QQ) agents, initial condition (IC), and quorum sensing (QS) agent number on (a) activation time, and (b) area-under-curve (AUC). Averages and standard deviations shown for each case for three consecutive simulations. AUC value is scaled by 1E-4.

Scenarios with low agent counts, specifically 4 agents, exhibited higher activation times and lower AUC values. The inclusion of QQ agents in the simulation led to an increase in activation time and a decrease in AUC. The presence of a non-zero initial condition decreased the activation time and increased AUC. Scenarios with high agent numbers, such as 133 agents, had significantly lower activation times and higher AUC values. A pronounced correlation between the area-under-the-curve (AUC) and activation time was discerned within the simulation, suggesting that the sensitivity or insensitivity observed for activation time can

be extended to predictions of AUC. All of these trends are consistent with experimental observations discussed in the previous chapter.

Figure IV.8 takes a closer look at agent and grid size, and GFP activation threshold.

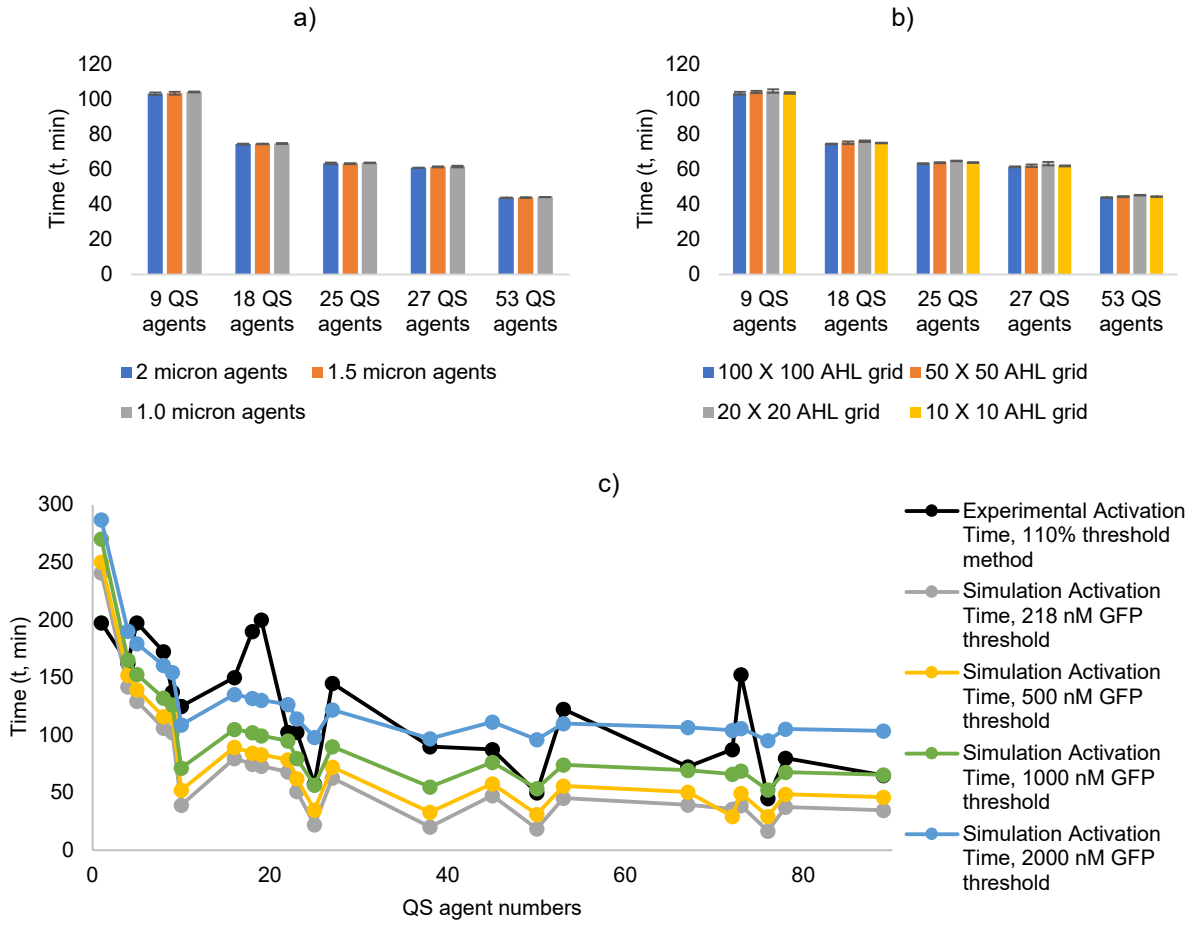

Fig. IV.8. Sensitivity Analysis: effect of (a) agent size, and (b) AHL grid size on activation time. Averages and standard deviations shown for each case for three consecutive simulations. (c) shows different GFP threshold concentrations to qualify activation time. Increasing the threshold increased the activation time.

In **Figure IV.8**, the model, under the selected grid and parameter configurations, exhibited insensitivity to minor variations in both agent size (a) and AHL grid dimensions (b). Consequently, to mitigate crowding issues in the simulation and reduce computational demands, an agent size of 1.5 microns and an AHL grid size of 20×20 were utilized.

Further tests revealed a lack of sensitivity in activation time to speed variations, up to ±30% of the experimental value, and to changes in domain size. For the simulations, a domain size of 1400 × 1400 μm² was employed, which is on a similar scale as previously utilized in research conducted by Leaman.

As seen in **Figure IV.8**, increasing the reference intracellular GFP threshold for activation time does increase the activation time. It should be noted, though, that activation time is not delayed by a consistent amount when comparing larger and smaller QS populations. Indeed, what threshold is used appears to matter less at low populations than high populations when it comes to influencing activation time. This is likely because by the time that smaller populations are reaching a population size where activation is possible, they are also entering steeper growth slopes of the parabolic growth curve, and thus steeper curves for GFP as well, resulting in less time between GFP checkpoints.

iv. Experimental Validation of Model and Predictions

In this section, we discuss the results of comparing the model to experimental data using QS-optimized parameters. The AHL upregulation threshold, and the basal and upregulated rates of AHL production were optimized to reduce error between computational activation time and experimental activation time using the large growth model and a subset of the QS-only experiments, the process of which is discussed in Section II.i. **Figure IV.9** compares the output GFP curves of the model to the experimental fluorescence curves for both QS-only and QS-QQ experiments with the TIR 1262 au strain.

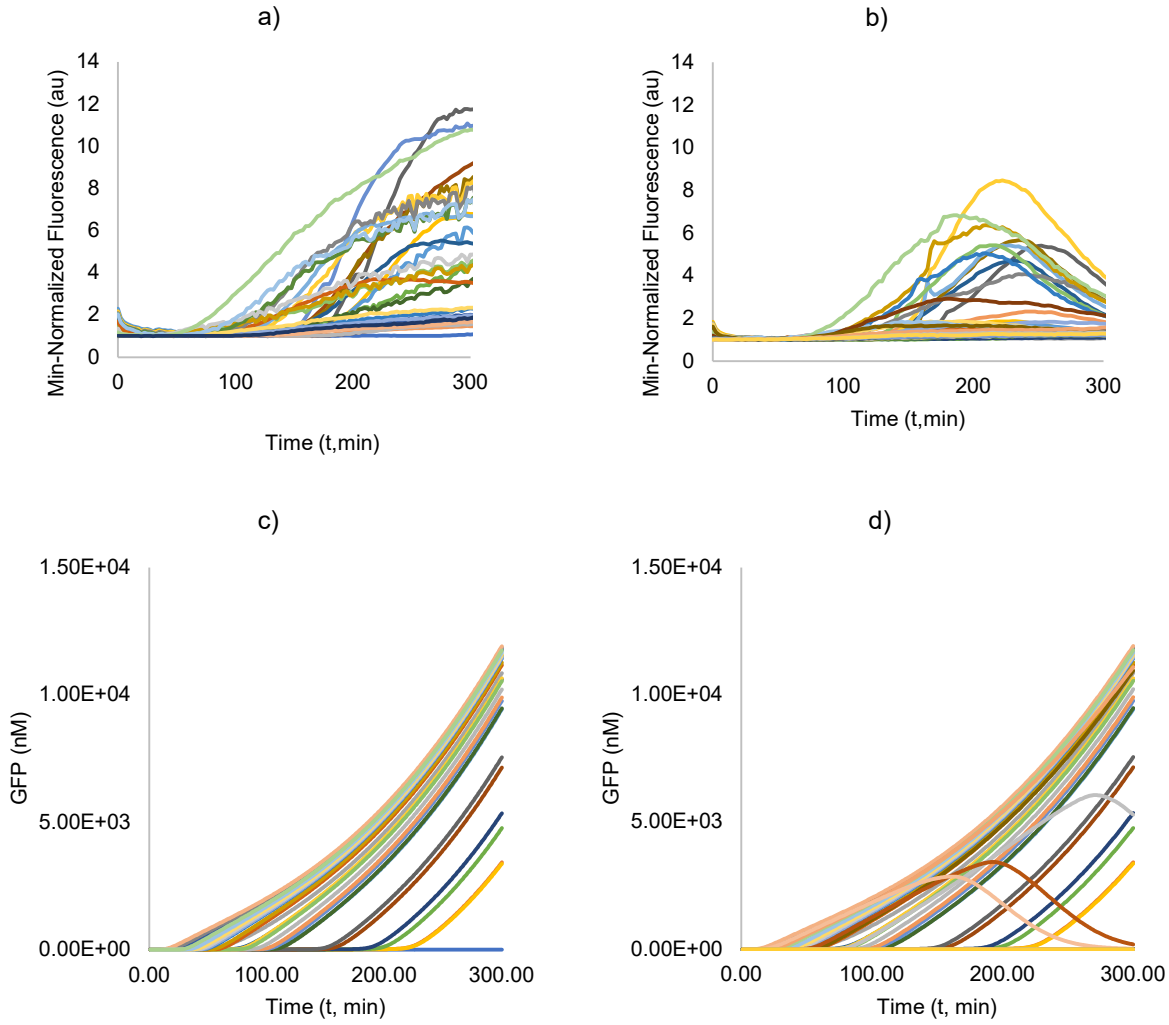

Fig. IV.9. Experimental (a), (b), and Simulation fluorescence (c), (d) curves for (left) QS-only dataset; (right) QS-QQ dataset, for 1262 TIR strain using the large growth model.

In the simulation, like experiments, the fluorescence curves for QS-only experiments were more likely to achieve and maintain activation. The QS-QQ cases in the model featured more of a hill or bell shape, where the gained fluorescence subsided with time, same as with experiments. While the model still predicts a sigmoidal shape for many QS-QQ experiments, the noticeable change in shape does suggest the QQ model has merit. We believe the differences in the model compared to experiments arise primarily from limitations with the growth model. In the simulation, growth follows the parabolic curve for 300 minutes or until the population reaches a size of 5000 agents. This, however, is likely not a perfect model of

reality, where growth ceilings are approached gradually and behavior appears to shift as the population itself grows, instead of binary switching on or off. Likely, then, the model overestimates QS (and QQ) growth and thus AHL and GFP production, resulting in stronger sigmoidal curves for QS-QQ than in experiments alone, where bell-shaped curves appear to comprise the majority instead.

The population ceiling of 5000 agents was established in the simulation because computational operation beyond a certain density would lead to errors and disruption of the simulation. The choice of 5000 agents as the ceiling, though an estimate, is not arbitrary; it represents 30 times the size of the largest quorum sensing (QS) population tested experimentally, equivalent to 150 agents. Based on the growth results and average growth curves discussed previously, it was anticipated that the population would not likely exceed 30 times the size of the largest observed population within a 300-minute timeframe, considering that in numerous experiments, signs of lag phase such as a significant decrease in bacteria size or microcolony formation (may be an indicator of loss of motility due to starvation), typically appeared after 300 minutes (about 5 hours). However, once again, the population ceiling estimates presented here are speculative and would require experimental validation in future studies to confirm their accuracy.

Next, we discuss quantitative comparison of simulations and experiments, especially in trends for activation time and AUC. **Figure IV.9** below shows the experimental vs simulation activation time for the 1262 au BioBrick QS construct, separating experiments in the dataset based on low or high initial conditions.

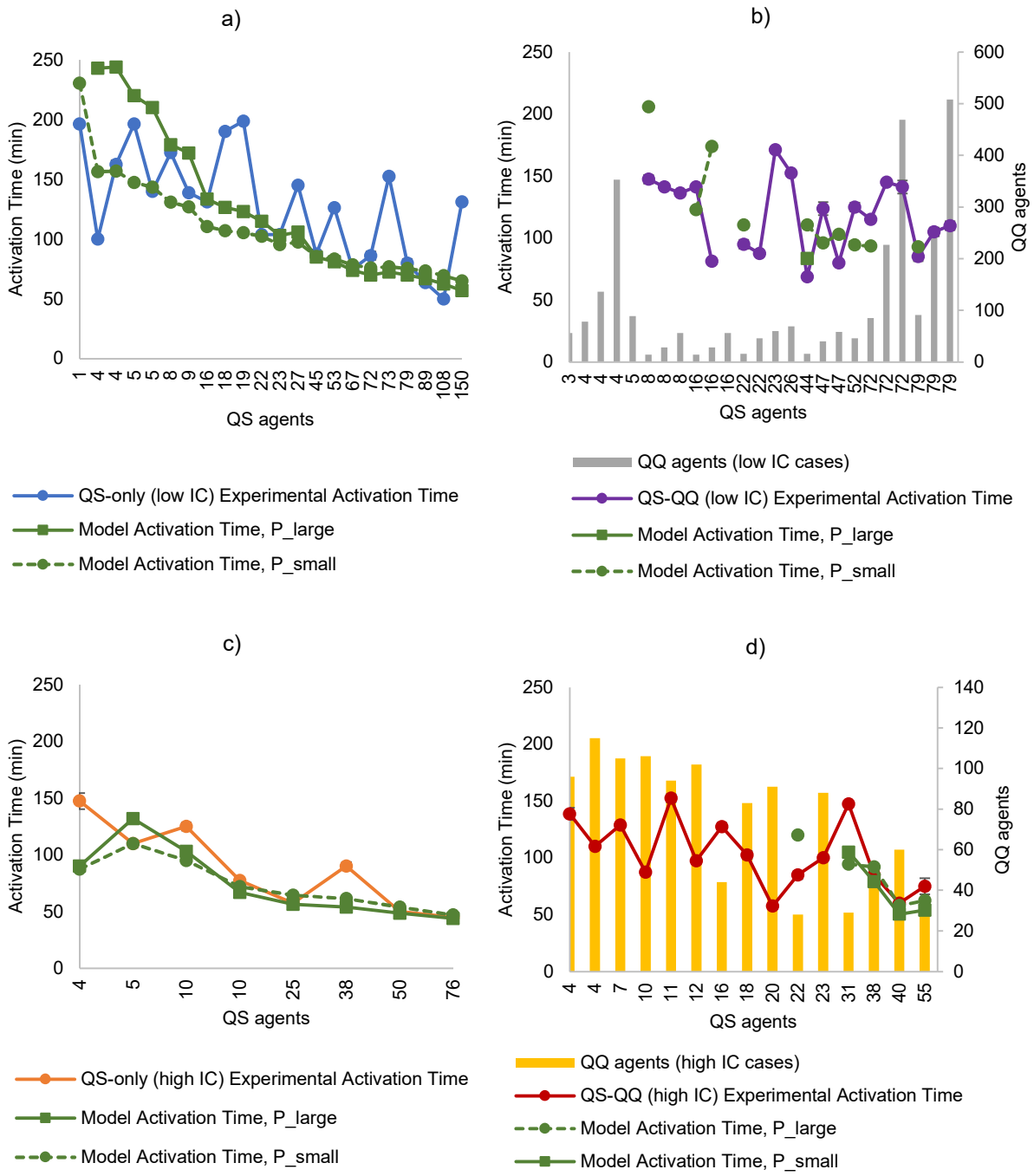

Fig. IV.10. Experimental and simulated activation time for TIR 1262 au strain in (a) low initial condition (IC) QS-only experiments, (b) low initial condition (IC) QS-QQ experiments, (c) high initial condition (IC) QS-only experiments, and (d) high initial condition (IC) QS-QQ experiments.

From **Figure IV.10**, it is apparent that, as with experiments, simulation activation time decreases with increasing QS agents and is generally higher for increased initial condition compared to lower initial condition experiments. However, in the majority of cases, for the experiments and especially for the larger growth model simulations, the BioBrick strain failed to activate when subjected to QQ conditions. With QS-QQ experiments, experiments with larger initial QS experiments did tend to activate but those with large numbers of QQ agents and/or small numbers of QS agents did not reach activation threshold even though corresponding experiments did. This indicates that the model may be overestimating QQ and need optimization of the QQ parameters to reconcile the differences between the experiments and the model. This overestimating of QQ behavior may in turn be partly due to inaccuracies in the QQ growth model. It is possible that we are overestimating QQ agent numbers at each point in time.

The differences between the large and small growth model appear to diminish as either the QS or the QQ (or both) agent numbers increase. This is likely because larger QS populations behave more similarly regardless of the growth model applied as they activate before having much chance to grow. Conversely, large QQ populations will dominate and dampen the QS signal regardless of QS growth model (note once again that QQ was always modeled with the large growth model equation).

Figure IV.11 shows the equivalent graphs for AUC instead of activation time.

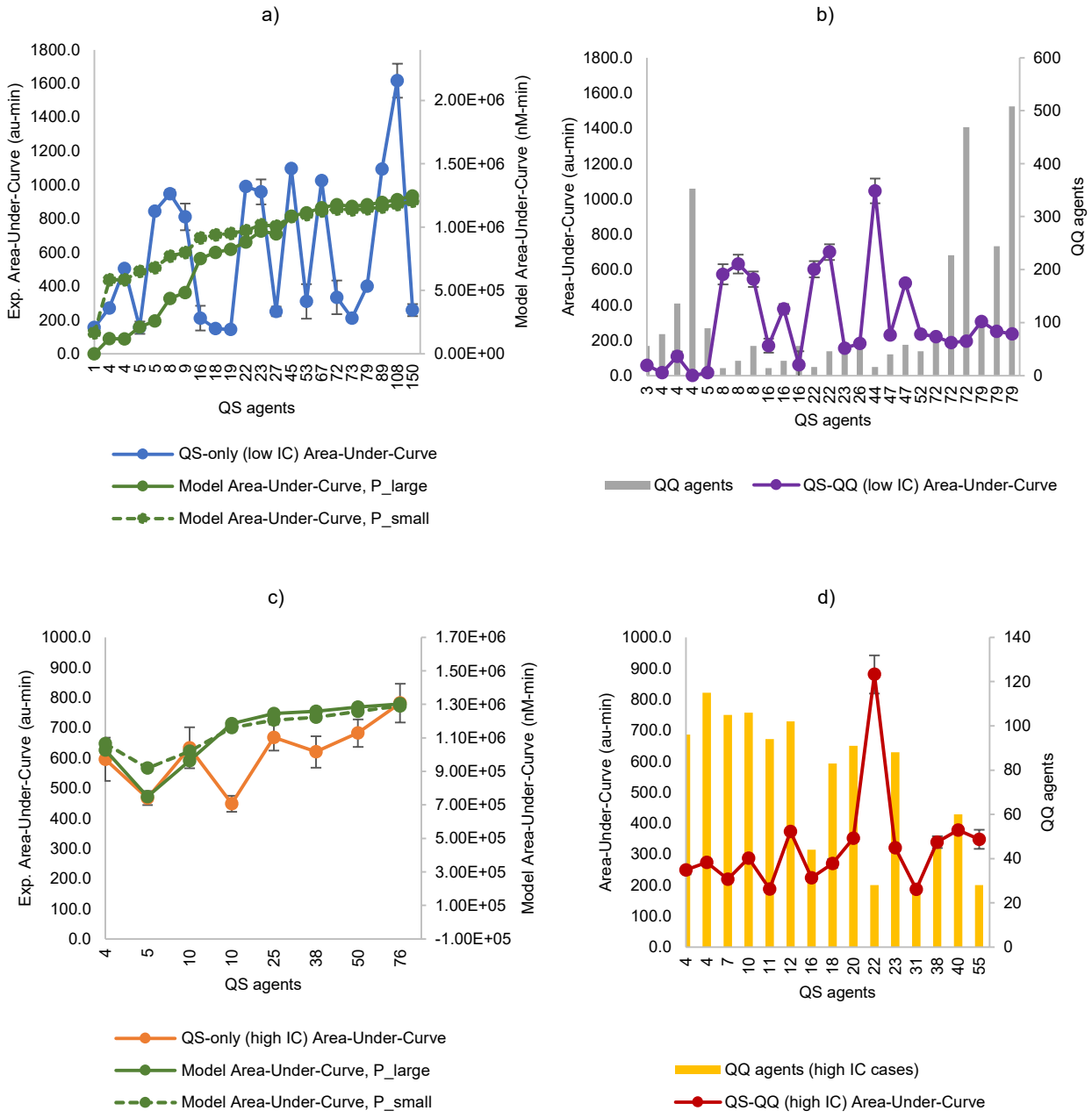

Fig. IV.11. Experimental and simulation AUC for TIR 1262 au strain in (a) low initial condition (IC) QS-only experiments, (b) low initial condition (IC) QS-QQ experiments, (c) high initial condition (IC) QS-only experiments, and (d) high initial condition (IC) QS-QQ experiments.

AUC generally shows opposite trends compared to activation time, albeit cleaner. The AUC is consistently lower for QS-QQ experiments compared to QS-only in the simulations, as was seen experimentally. AUC generally appears to increase with increasing QS agents, and AUC

peaks tend to correspond with QQ agent valleys and vice versa. Once again, in the QS-only experiments, the large growth model predictions were more accurate for scenarios with higher agent counts. Conversely, the small growth model gave closer approximations in test cases with lower agent numbers. As either type of agents increases, the different growth model outputs converge. Likely the difference between the small and large growth model for AUC is due accounted by the same reasons that cause discrepancies with activation time, discussed earlier.

It is important to also note here the observable difference in the scales between experimental and simulation AUC. AUC for simulations is best represented on a log scale, while the same does not hold for experimental AUC. We believe this is not surprising, as experimental AUC is a measure of the area of the normalized fluorescence curve (au), while simulated AUC is a measure of the area of the GFP concentration (nM). Because GFP concentration has a much wider range (by several orders of magnitude) as an output across 300 minutes in the simulation, differences in the area under a variety of experimental curves will be further emphasized and compounded by the nature of integration, even discrete integration when compared to experimental fluorescence curves, where the values ranged between 1.0 and 12.0. We believe the development of a scaling factor in future work will help reconcile the differences between experimental and simulated AUC.

Figures IV.12 and **IV.13** provide an alternate method for organizing and thus viewing the data: by increasing QQ agents. **Figure IV.12** shows the model directly compared to experiments, where both QS-growth variations of the model follow the same experimental AUC trends. The peaks and valleys align, as well as the general downward trend as QQ agent number (horizontal axis) increases.

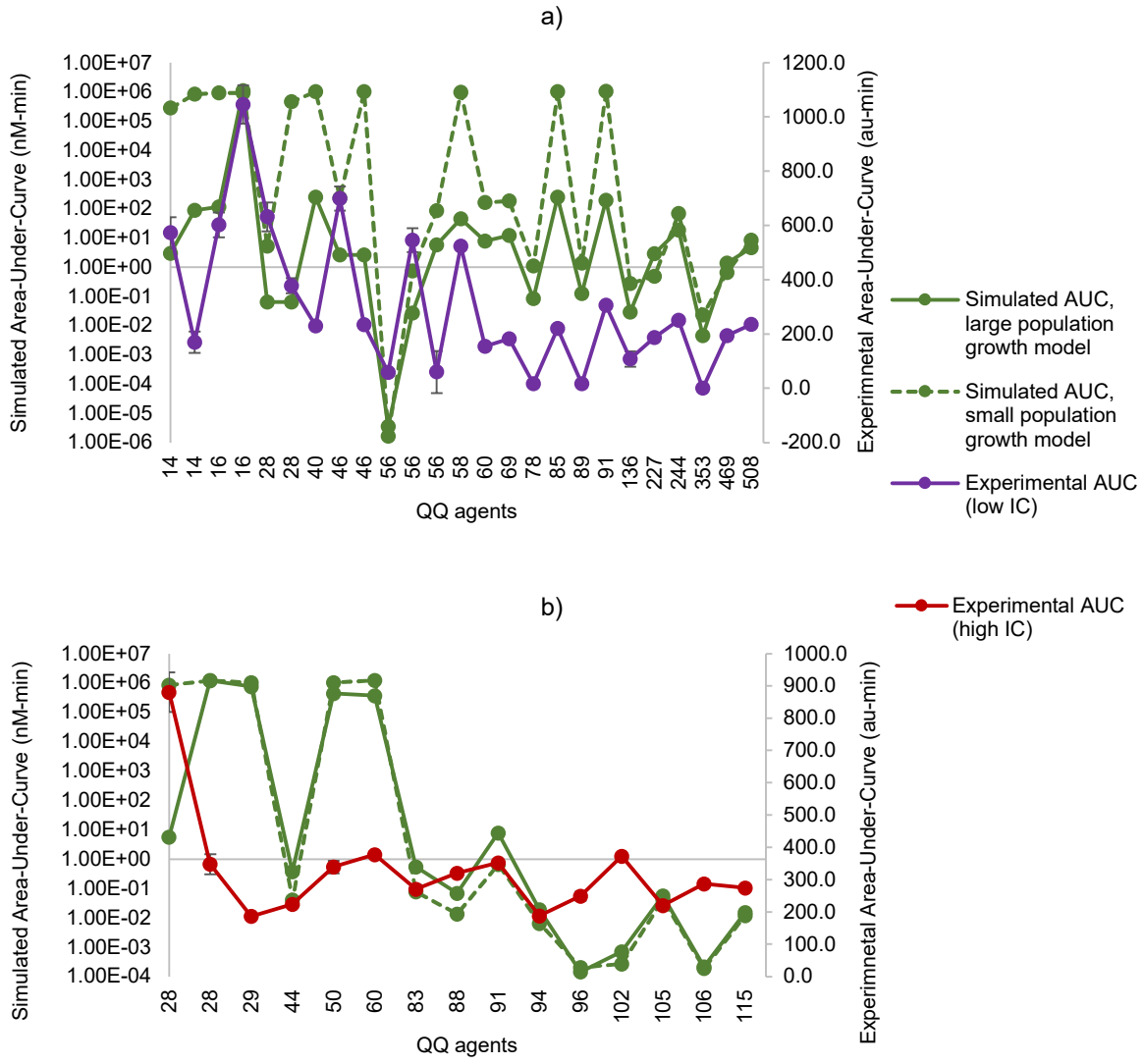

Fig. IV.12. Simulation vs Experiments for AUC for TIR 1262 au (BioBrick) strain. QS-QQ Experiments vs simulation using large QS population growth model or small QS population growth model for low initial condition (<200 au) (a) or (b) high initial condition (200+ au). It should be noted that the number of QS agents is not constant in these graphs.

Interestingly, as seen more closely in **Figure IV.12**, it appears that higher IC experiments are less sensitive to the use of different growth models. This makes sense, as experiments with non-zero initial conditions have a head start toward activation and are less reliant on growth to achieve the needed AHL threshold.

Figure IV.13 looks closer at the model output and the relation between QS agents, QQ agents, and AUC.

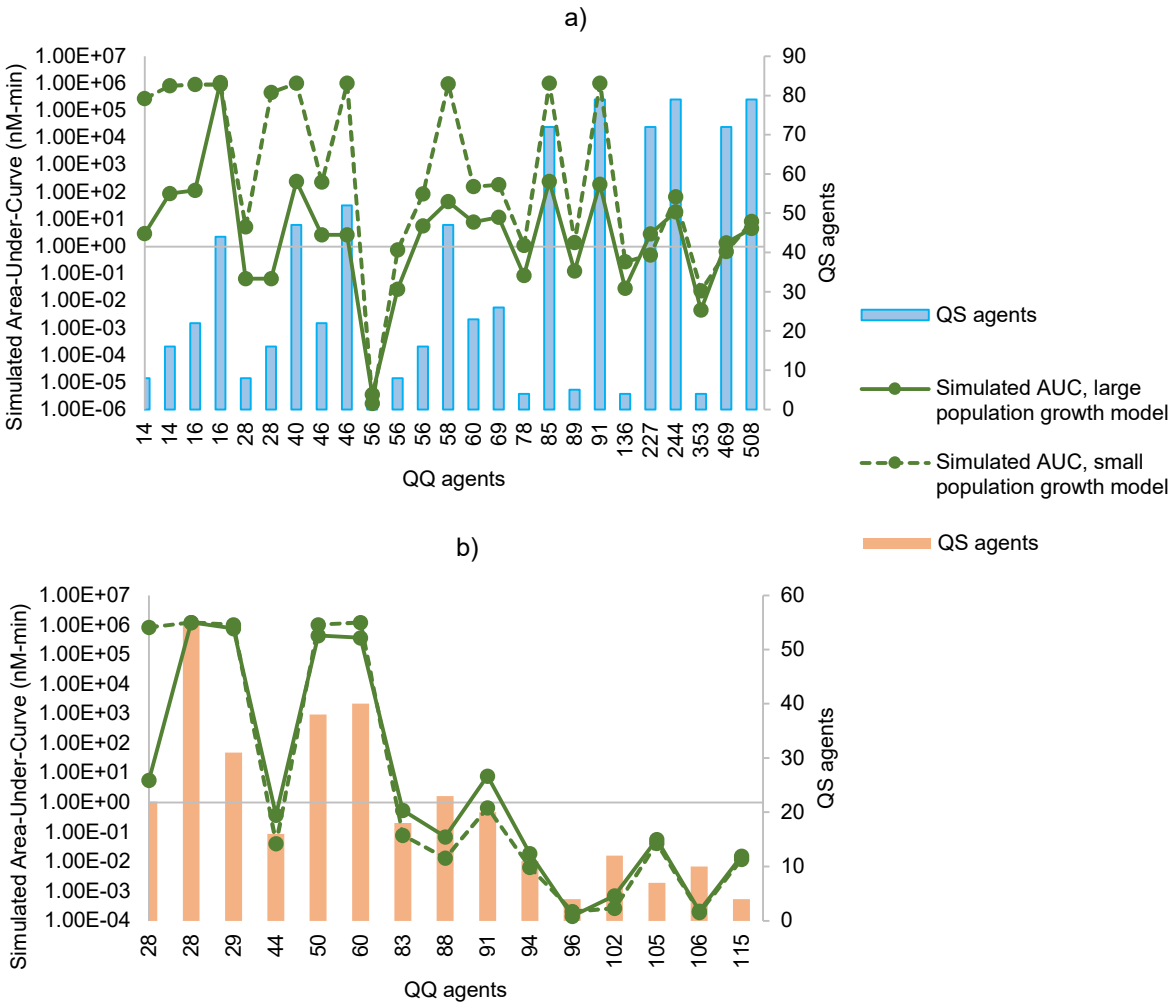

Fig. IV.13. Simulations for TIR 1262 (BioBrick) for QS-QQ experiments with (a) low initial condition (<200 au) and (b) high initial condition (200+ au). Cases ordered from left to right by increasing QQ agent number.

Note that the simulations for the entire dataset of TIR 1262 strain experiments is shown in Appendix I, Figures A.2 and A.3.

Figure IV.13 shows more clearly that AUC increases or decreases as the QS agents (pink or blue bars) increase or decrease, and that increasing QQ agents results in a gentle downward trend in AUC.

Figure IV.14 shows simulation predictions for the less sensitive TIR 30 au and TIR 99 au slower QS strains, to complement the work with the TIR 1262 au strain.

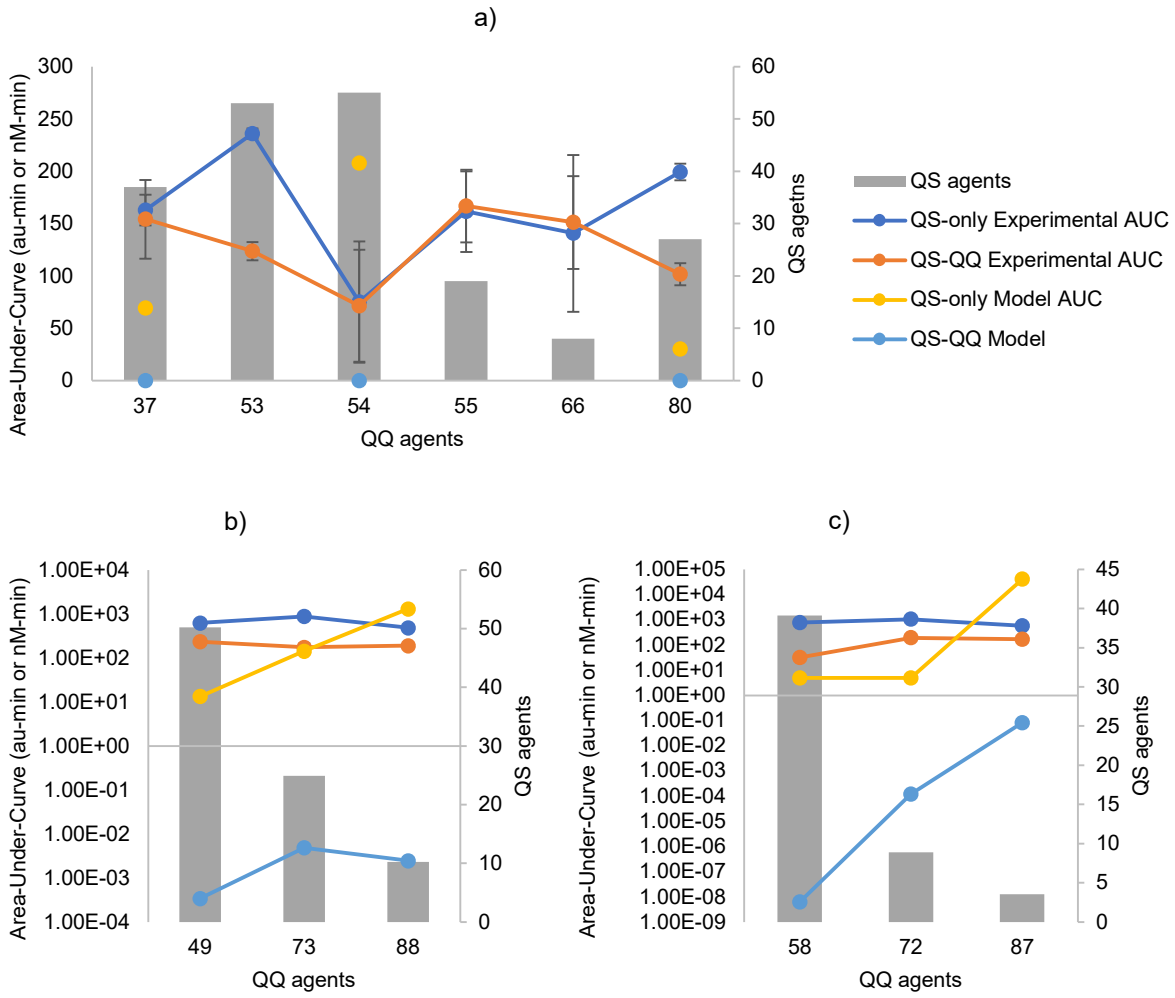

Fig. IV.14. Simulation vs Experiments Area-Under-Curve for (a) TIR 30 au single *luxI* and (b) double *luxI*, and (c) 99 au single *luxI*. Standard deviation from 3 simulations for AUC were less than or equal to 2% error.

Once again, simulated and experimental AUC is lower for QS-QQ experiments compared to QS-only. However, the trends are not as clear as with the TIR 1262 au strain, especially when it comes to variation of independent variables such as QS or QQ agents. This suggests that perhaps a certain threshold strength of the QS circuit is needed to be able to perceive differences between experiments with different QS agent numbers or QQ agent numbers. Furthermore, once again, as with the TIR 1262 strain, the model may overestimate the impact

of QQ on QS, leading to a more dramatic predicted interference than what is observed experimentally. Activation times for the TIR 99 au and TIR 30 au strains are not shown because most of the QS-QQ experiments did not activate. Again, this suggests that activation time is not as useful a parameter for describing QQ-associated attenuation of QS fluorescence as AUC is. More refinement and optimization of QQ parameters and growth model, once again, would be needed for the model to mirror the nuances of the effect of QQ more accurately on QS activation in laboratory settings, and in applications beyond.

One of the main benefits of a model is being able to test edge cases. **Figure IV.15** shows the model predictions when holding QS agents constant and varying QQ agents or initial conditions.

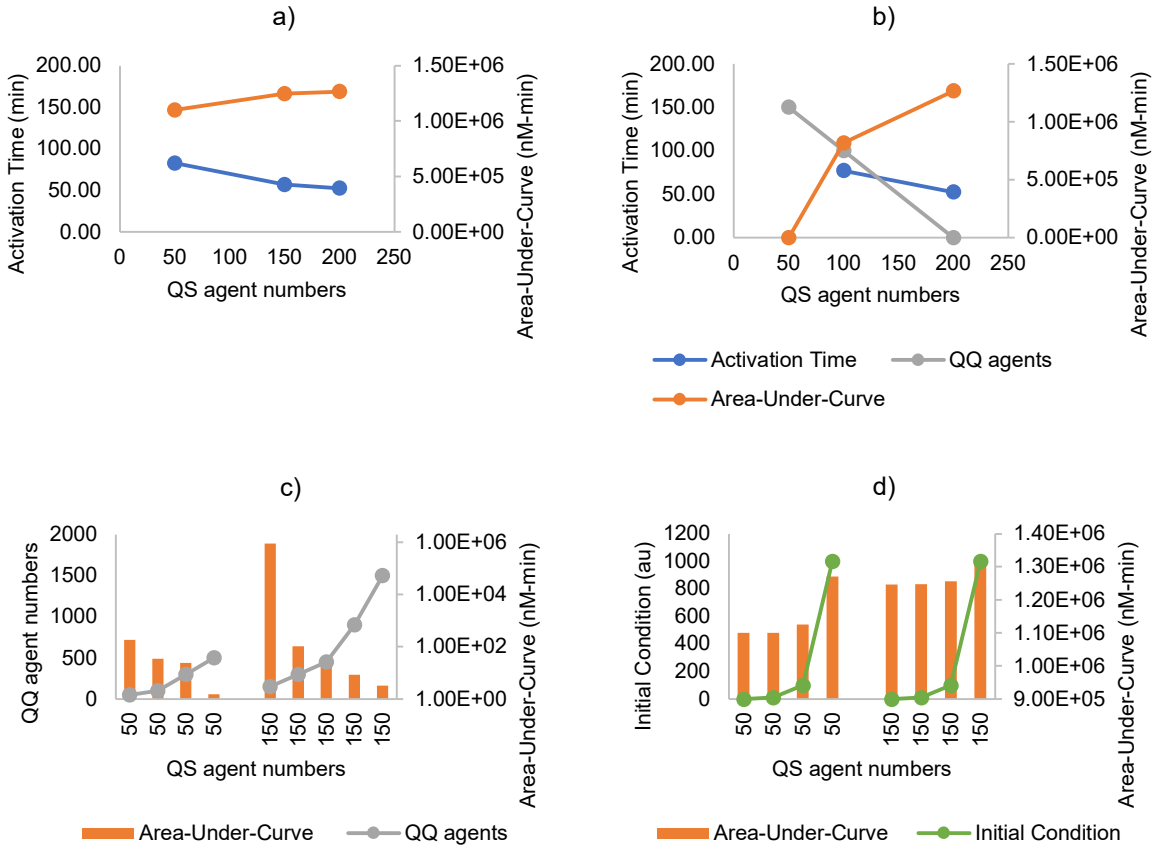

Fig. IV.15. Simulation predictions for Activation Time and Area-Under-Curve (AUC) for varying initial conditions and QS-QQ ratios. (a) increasing QS agents in QS-only simulations; (b) decreasing QQ proportions with constant total agents; (c) AUC with increasing QQ agents; (d); AUC with increasing initial condition with different numbers of QQ agents. Standard deviation from 3 simulations for AUC were less than or equal to 2% error.

As shown in **Figure IV.15**, the simulations predicted that Activation Time and AUC increased with increasing QS agents for both QS-only and QS-QQ experiments. When QQ agents are present in high ratios, the AUC is severely affected. For smaller QS populations (50 agents) compared to larger populations (150 agents), increasing QQ agents results in decreasing AUC, although larger populations have higher AUCs compared to smaller populations with comparable ratios, as shown in Fig. IV.15c. The initial condition did not have as strong an impact on AUC, but higher ICs led to higher AUC, with the benefit being more marginal for larger populations compared to smaller populations (Fig. IV.15d). In a similar way, smaller populations even with the same non-zero IC compared to larger populations are still heavily

affected when QQ agents are present. It appears that IC presents marginal benefit when high ratios of QQ are present.

Finally, it was necessary to evaluate the sensitivity of the QQ model to growth and also QQ parameters such as k_A, the constitutive rate of AiiA production, and $k_{A,deg}$, the relative rate of AiiA degradation. **Figure IV.16** shows how multiplying the leading term in the parabolic growth models by 1.20 or 0.8 affects the activation time or AUC for QS-QQ experiments.

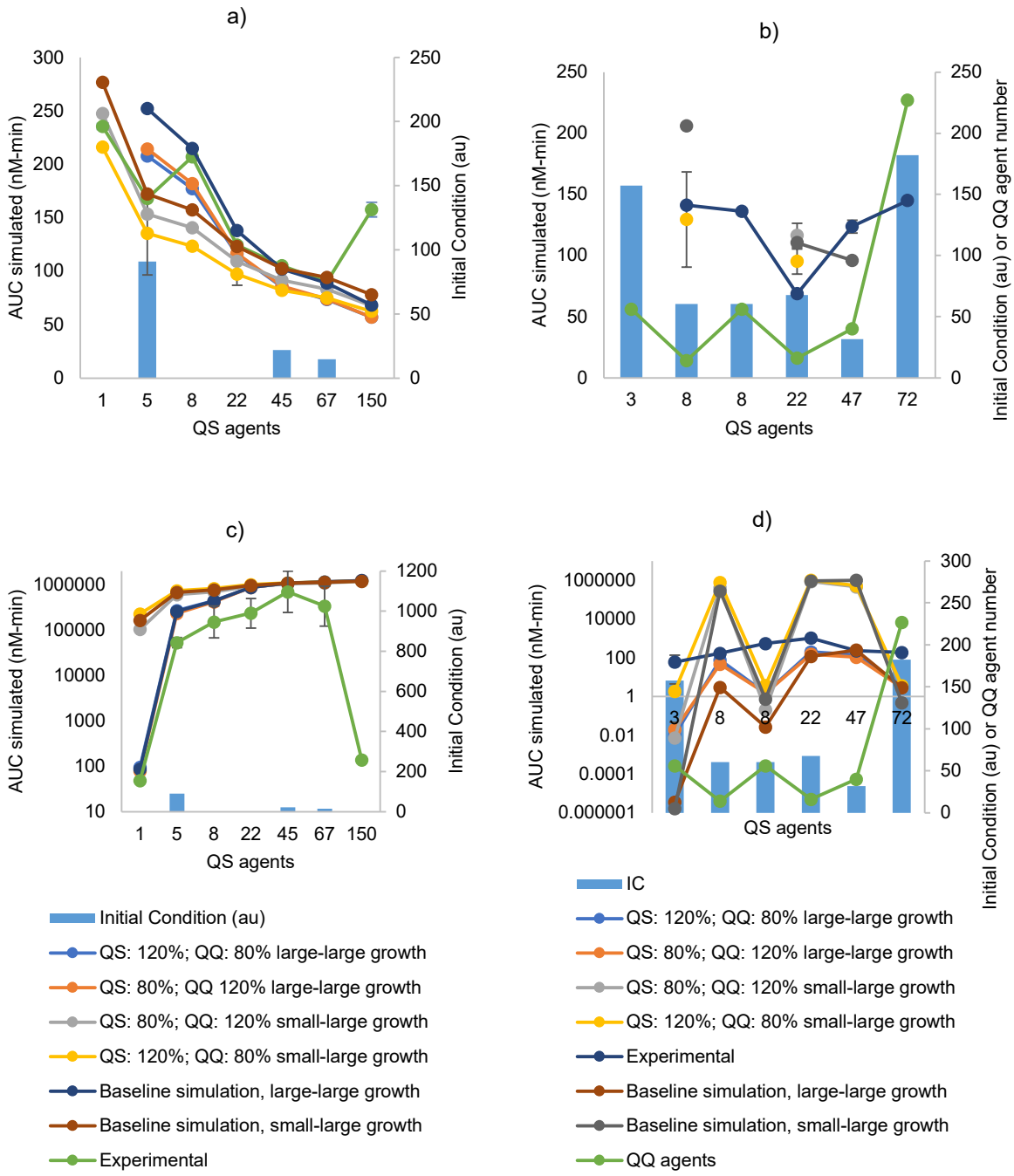

Fig. IV.16. Simulation predictions for activation time for (a) QS only and (b) QS-QQ, and Area-Under-Curve (AUC) for (c) QS-only and (d) QS-QQ.

In **Figure IV.16**, it is clear once again that the model is sensitive to growth more so with smaller QS populations. Comparing the modified growth simulations to respective baselines, the large growth model appears less sensitive to growth modification or error than the small

growth model. This seems to agree with observations earlier. Once again, activation time is not as informative a parameter as AUC, as most of the QS-QQ experiments did not activate, either with the baseline growth curves or the modified ones.

Figure IV.17 shows how modifying the rate of AiiA production affects the simulation. Also, a comparison of the area under the curve for 300 minutes to the area under the curve for 100 minutes in the simulation is shown as well.

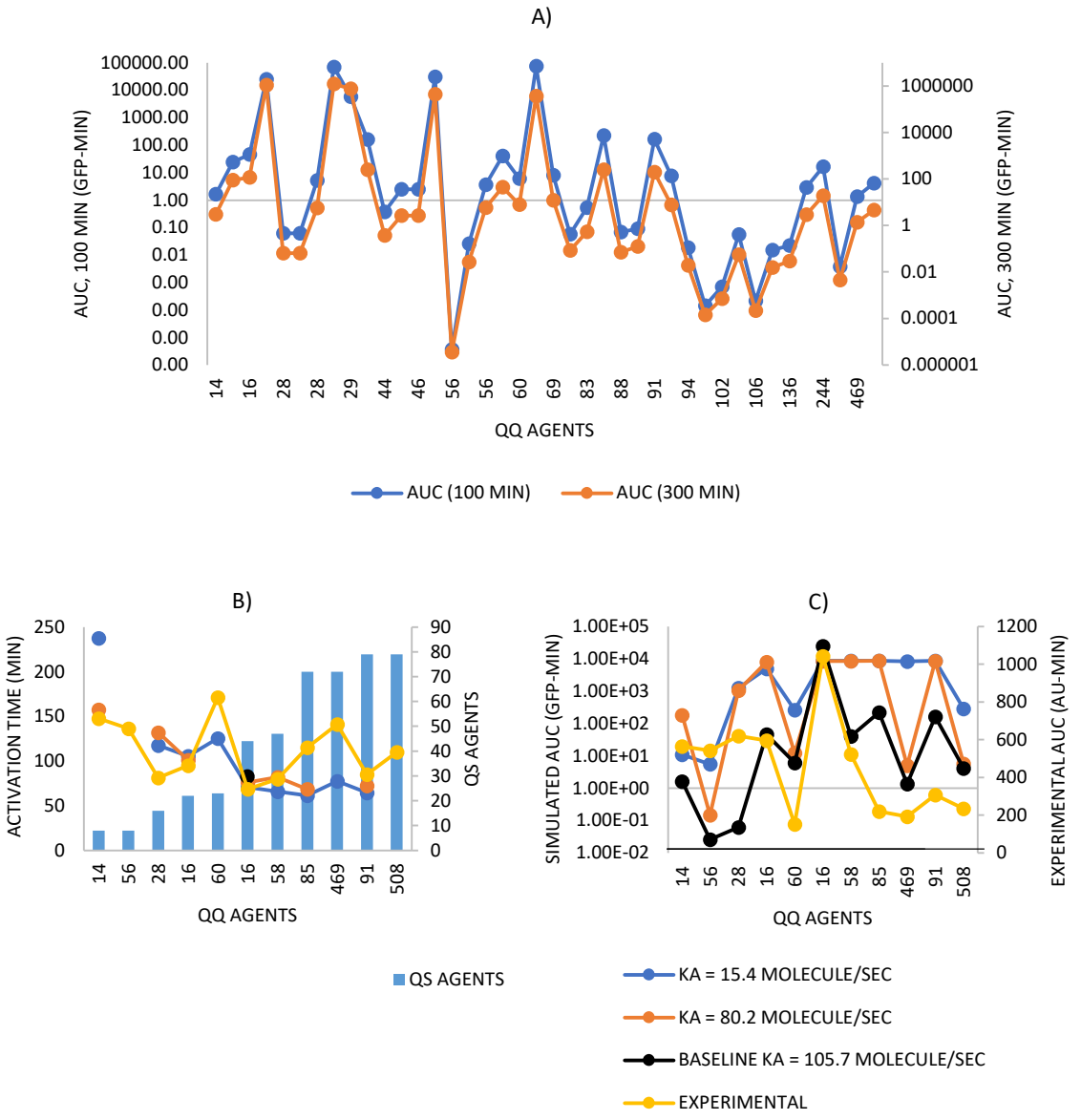

Fig. IV.17. Simulation predictions. (a) 300 min basis for AUC vs 100 min basis; (b) activation time for various AiiA production rates; (c) AUC (100 min basis) for various AiiA production rates.

Since according to Figure IV.17, there is not significant difference in the pattern between the AUC based on 300 minutes to the AUC based on 100 minutes, we can confidently compare the simulations with varied AiiA production rates to the simulation with the baseline production rate as well as to experiments. Regarding differences in simulation results when changing AiiA production rates, it appears that lower AiiA production rates result in more QS-QQ experiments activating than with the baseline simulations (IV.17b), even for experiments with

lower QS agents. This makes sense, and the results suggest that our baseline simulations were overestimating AiiA production. Modifying AiiA production rate also seemed to affect the AUC (IV.17c), especially for high QQ agent numbers. If we lower AiiA too much, the AUC for large QS population cases and activation time with small QS population cases rise too much and start deviating from experimental trends. More work would be needed to optimize the QQ model parameters to minimize error for both activation time and AUC, but we have reason to believe the model would only improve further in matching experiments with such tuning of parameters.

Altogether, the results suggest that the model does indeed present some merit based on comparisons of experiments to simulations. While activation time cannot always be relied on due to experiment cases failing to meet the criteria and is thus only a useful metric if activation is indeed achieved, AUC is a useful indication of the dampening of QQ on QS fluorescence, regardless of whether the experiment achieved “activation” or not. These results suggest that AUC is an effective parameter for quantitatively characterizing the complex impact of QQ on QS dynamics, in this project and moving forward.

V. Chapter 5: Conclusions and Future Directions

Our hopes are that this thesis contributes to a deeper understanding of quorum sensing (QS) and quorum quenching (QQ) interactions and dynamics in microbial communities through our agar-based experiments and computational exploration. To reiterate the key conclusions discussed in the previous two chapters, we report that certain spatial organization of the QS-QQ commnities do attenuate QS-associated fluorescent signal more than others. The Area-Under-Curve (AUC) of the fluorescent signal was lower for homogenously distributed QS-QQ populations and for split layer populations, and activation time follows an opposite trend.

The original hypothesis that QQ delays onset of QS behavior was not supported. The primary manifestation of QQ's effect on QS bacteria is attenuation of the QS signal as opposed to delay (activation time), as measured by the Area-Under-Curve (AUC) parameter. However, the effect of QQ on QS is better understood by looking at both. AUC is positively correlated with the initial condition and QS agent count and negatively correlated with QQ agent count. Activation time is positively correlated with QQ agent number and negatively correlated with QS agent number and initial condition.

Furthermore, the model predictions for AUC and activation time, while not perfectly reconciled to experiments, appear to have merit, based on comparison with experimental data.

The growth analysis suggested that a certain consistent density must be reached to achieve QS. It is encouraging that the density or concentration threshold appears generally to be the same regardless of initial population size. If and how this threshold changes with varying QQ population sizes or ratios would be an interesting question to explore in future work.

The data in homogenously mixed communities, we believe, has consistently demonstrated that QQ attenuates the intensity of QS signals, resulting in lower AUC values for QS-QQ scenarios compared to QS-only experiments. This effect predominantly influences the strength rather than the timing of QS activation, unlike initially hypothesized. Spatial configuration also plays a role, however, in the degree of attenuation of QS-associated fluorescence. The QS-QQ split bulk setup, in particular, showed less impact from QQ agents due to spatial separation and increased diffusion length of chemical signals while the split-layer arrangement results

indicated more pronounced QS attenuation, suggesting that physical distancing within bacterial populations plays an important role.

Though our research answered a few of our initial questions regarding QQ behavior, it opened up many more in turn. The assumption that QQ agents exhibit similar growth patterns to QS agents was a starting point, but future work would benefit from more exploration and accurate modeling, given the impact of growth on QS in simulations of green fluorescent protein (GFP) production. Growth dynamics could change when bacterial strains are not isolated but are part of a community, as interactions may alter growth rates. The challenges in measuring community growth rates due to fluorescent signal attenuation and the difficulty in discerning individual bacteria in agar-based experiments precluded such a model from being part of the scope of this work. However, moving forward, future research could concentrate on the development of more complex growth models for both QS and QQ agents that can adapt in real-time to changing population sizes, and account for strain interaction in co-cultured populations which could significantly refine the predictive accuracy for quorum sensing activation time and AUC values. A model universally applicable across varying initial population sizes would be beneficial, incorporating equations that take into account nutrient consumption and availability. Our current experimental setup, which does not replenish nutrients, leads to nutrient depletion. This depletion occurs more rapidly with larger initial population sizes, affecting the growth rate. Therefore, a model that operates under steady nutrient conditions, such as those in a microfluidic system, might enable the formulation of a more universally applicable equation for a broader range of population sizes.

Next, the QQ parameters in the simulation would benefit from being optimized based on AUC error between the model and experiments to improve predictions, and more work is also needed to scale and reconcile the scale discrepancies between the model and the experiments in AUC predictions. The use of 654 nM as the intracellular GFP threshold to consider activation achieved in the simulation may also benefit from experimentally-informed optimization.

Also, to further characterize the effect of spatial arrangements with QS-QQ interactions, control wells of QS-only geometries could be added to the experimental setup. This would help answer the question of how much of the difference in AUC between the different geometry

arrangements is an artifact that would manifest similarly in QS-only experiments, and how much is the result of altered QS-QQ spatial interaction.

Finally, the model has only been applied in this work towards homogenously mixed communities. Application of the agent-based model to spatially separated experiments could further test the model towards similar applications in industry and research.

While we present an experimentally validated QS-QQ model, further research is needed to refine our models and experiments. Our hope is that this work complements ongoing advancements in the exploration of microbial communities and their interactions, that our contributions further the collective effort to not only understand but also manipulate and harness microbial communication towards ecological sustainability, human health, and disease management; and that this work contributes to the ongoing dialogue surrounding the complexities of microbial dynamics.

References

Anandan, K., & Vittal, R. R. (2019). Quorum quenching activity of AiiA lactonase KMMI17 from endophytic Bacillus thuringiensis KMCL07 on AHL- mediated pathogenic phenotype in Pseudomonas aeruginosa. *Microbial Pathogenesis*, *132*. https://doi.org/10.1016/j.micpath.2019.05.015

Cho, I., & Blaser, M. J. (2012). The human microbiome: At the interface of health and disease. In *Nature Reviews Genetics* (Vol. 13, Issue 4). https://doi.org/10.1038/nrg3182

Clemente, J. C., Ursell, L. K., Parfrey, L. W., & Knight, R. (2012). The impact of the gut microbiota on human health: An integrative view. In *Cell* (Vol. 148, Issue 6). https://doi.org/10.1016/j.cell.2012.01.035

Dejea, C. M., Wick, E. C., Hechenbleikner, E. M., White, J. R., Mark Welch, J. L., Rossettid, B. J., Peterson, S. N., Snesrud, E. C., Borisy, G. G., Lazarev, M., Stein, E., Vadivelu, J., Roslani, A. C., Malik, A. A., Wanyiri, J. W., Goh, K. L., Thevambiga, I., Fu, K., Wan, F., … Sears, C. L. (2014). Microbiota organization is a distinct feature of proximal colorectal cancers. *Proceedings of the National Academy of Sciences of the United States of America*, *111*(51). https://doi.org/10.1073/pnas.1406199111

Delgado-Baquerizo, M., Oliverio, A. M., Brewer, T. E., Benavent-González, A., Eldridge, D. J., Bardgett, R. D., Maestre, F. T., Singh, B. K., & Fierer, N. (2018). *A global atlas of the dominant bacteria found in soil*. http://science.sciencemag.org/

Dong, Y. H., & Zhang, L. H. (2005). Quorum sensing and quorum-quenching enzymes. In *Journal of Microbiology* (Vol. 43).

Geller, L. T., Barzily-Rokni, M., Danino, T., Jonas, O. H., Shental, N., Nejman, D., Gavert, N., Zwang, Y., Cooper, Z. A., Shee, K., Thaiss, C. A., Reuben, A., Livny, J., Avraham, R., Frederick, D. T., Ligorio, M., Chatman, K., Johnston, S. E., Mosher, C. M., … Straussman, R. (2017). Potential role of intratumor bacteria in mediating tumor resistance to the chemotherapeutic drug gemcitabine. *Science*, *357*(6356). https://doi.org/10.1126/science.aah5043

Helman, Y., & Chernin, L. (2015). Silencing the mob: Disrupting quorum sensing as a means to fight plant disease. In *Molecular Plant Pathology* (Vol. 16, Issue 3). https://doi.org/10.1111/mpp.12180

Helmink, B. A., Khan, M. A. W., Hermann, A., Gopalakrishnan, V., & Wargo, J. A. (2019). The microbiome, cancer, and cancer therapy. In *Nature Medicine* (Vol. 25, Issue 3). https://doi.org/10.1038/s41591-019-0377-7

Kim, I., Jang, J. U., Park, H., Park, J., Oh, H. S., Lee, S., Choo, K. H., Park, P. K., & Lee, K. (2023). An efficient continuous quorum quenching feed to mitigate membrane biofouling in membrane bioreactors: Strain 1A1 (extracellular) versus strain BH4 (intracellular). *Journal of Water Process Engineering*, *52*. https://doi.org/10.1016/j.jwpe.2023.103594

Kim, J., Kim, J., Kim, Y., Oh, S., Song, M., Choe, J. H., Whang, K. Y., Kim, K. H., & Oh, S. (2018). Influences of quorum-quenching probiotic bacteria on the gut microbial community and immune function in weaning pigs. *Animal Science Journal*, *89*(2). https://doi.org/10.1111/asj.12954

Leaman, E. (2016). *An Experimentally-validated Agent-based Model to Study the Emergent Behavior of Bacterial Communities*. Virginia Tech.

Leaman, E. J., Geuther, B. Q., & Behkam, B. (2018). Quantitative Investigation of the Role of Intra-/Intercellular Dynamics in Bacterial Quorum Sensing. *Cite This: ACS Synth. Biol*, *7*, 1030–1042. https://doi.org/10.1021/acssynbio.7b00406

Leaman, E. J., Geuther, B. Q., & Behkam, B. (2019). Hybrid centralized/decentralized control of a network of bacteria-based bio-hybrid microrobots. *Journal of Micro-Bio Robotics*, *15*. https://doi.org/10.1007/s12213-019-00116-0

Leaman, E. J., Sahari, A., Traore, M. A., Geuther, B. Q., Morrow, C. M., & Behkam, B. (2020). Data-driven statistical modeling of the emergent behavior of biohybrid microrobots. *APL Bioengineering*, *4*, 16104. https://doi.org/10.1063/1.5134926

Maeda, T., García-Contreras, R., Pu, M., Sheng, L., Garcia, L. R., Tomás, M., & Wood, T. K. (2012). Quorum quenching quandary: Resistance to antivirulence compounds. *ISME Journal*, *6*(3). https://doi.org/10.1038/ismej.2011.122

Margolis, K. G., Cryan, J. F., & Mayer, E. A. (2021). The Microbiota-Gut-Brain Axis: From Motility to Mood. In *Gastroenterology* (Vol. 160, Issue 5). https://doi.org/10.1053/j.gastro.2020.10.066

Miller, M. B., & Bassler, B. L. (2001). Quorum sensing in bacteria. In *Annual Review of Microbiology* (Vol. 55). https://doi.org/10.1146/annurev.micro.55.1.165

Molnar, A. (2019). Antimicrobial Resistance Awareness and Games. In *Trends in Microbiology* (Vol. 27, Issue 1). https://doi.org/10.1016/j.tim.2018.09.007

Momb, J., Wang, C., Liu, D., Thomas, P. W., Petsko, G. A., Guo, H., Ringe, D., & Fast, W. (2008). Mechanism of the quorum-quenching lactonase (AiiA) from Bacillus thuringiensis. 2. Substrate modeling and active site mutations. *Biochemistry*, *47*(29). https://doi.org/10.1021/bi8003704

Müller, J., Kuttler, C., Hense, B. A., Rothballer, M., & Hartmann, A. (2006). Cell-cell communication by quorum sensing and dimension-reduction. *Journal of Mathematical Biology*, *53*(4). https://doi.org/10.1007/s00285-006-0024-z

Ouyang, Y., Hu, Y., Huang, J., Gu, Y., Shi, Y., Yi, K., & Yang, Y. (2020). Effects of exogenous quorum quenching on microbial community dynamics and biofouling propensity of activated sludge in MBRs. *Biochemical Engineering Journal*, *157*. https://doi.org/10.1016/j.bej.2020.107534

Pan, X. rong, Yuzuak, S., Lou, J. min, Chen, L., Lu, Y., & Zuo, J. e. (2023). Microbial community and antibiotic resistance gene distribution in food waste, anaerobic digestate, and paddy soil. *Science of the Total Environment*, *889*. https://doi.org/10.1016/j.scitotenv.2023.164192

Proctor, L. M., Creasy, H. H., Fettweis, J. M., Lloyd-Price, J., Mahurkar, A., Zhou, W., Buck, G. A., Snyder, M. P., Strauss, J. F., Weinstock, G. M., White, O., & Huttenhower, C. (2019). The Integrative Human Microbiome Project. *Nature*, *569*(7758). https://doi.org/10.1038/s41586-019-1238-8

Qian, Y., Lan, F., & Venturelli, O. S. (2021). Towards a deeper understanding of microbial communities: integrating experimental data with dynamic models. In *Current Opinion in Microbiology* (Vol. 62). https://doi.org/10.1016/j.mib.2021.05.003

Rodríguez, M., Torres, M., Blanco, L., Béjar, V., Sampedro, I., & Llamas, I. (2020). Plant growth-promoting activity and quorum quenching-mediated biocontrol of bacterial phytopathogens by Pseudomonas segetis strain P6. *Scientific Reports*, *10*(1). https://doi.org/10.1038/s41598-020-61084-1

Sepich-Poore, G. D., Zitvogel, L., Straussman, R., Hasty, J., Wargo, J. A., & Knight, R. (2021). The microbiome and human cancer. In *Science* (Vol. 371, Issue 6536). https://doi.org/10.1126/science.abc4552

Shah, S. S. A., Park, H., Park, H. J., Kim, J., Angelidaki, I., Lee, C., Kim, J., & Choo, K. H. (2023). Polyelectrolyte-silica composite quorum quenching biomedia as new antifouling agents for anaerobic membrane bioreactor treatment. *Chemical Engineering Journal*, *452*. https://doi.org/10.1016/j.cej.2022.139568

Song, H., Payne, S., Gray, M., & You, L. (2009). Spatiotemporal modulation of biodiversity in a synthetic chemical-mediated ecosystem. *Nature Chemical Biology*, *5*(12). https://doi.org/10.1038/nchembio.244

Song, X. N., Cheng, Y. Y., Li, W. W., Li, B. B., Sheng, G. P., Fang, C. Y., Wang, Y. K., Li, X. Y., & Yu, H. Q. (2014). Quorum quenching is responsible for the underestimated quorum sensing effects in biological wastewater treatment reactors. *Bioresource Technology*, *171*. https://doi.org/10.1016/j.biortech.2014.08.027

Wang, Q., Bai, X., Miao, Q., Wang, T., Wang, X., & Xu, Q. (2023). Isolation and characterization of quorum quenching bacteria from municipal solid waste and bottom ash co-disposal landfills. *Waste Management and Research*, *41*(9). https://doi.org/10.1177/0734242X231155807

World Health Organization. (2021). Global antimicrobial resistance and use surveillance system (GLASS) report 2021. In *World Health Organization.*

Wu, S., Feng, J., Liu, C., Wu, H., Qiu, Z., Ge, J., Sun, S., Hong, X., Li, Y., Wang, X., Yang, A., Guo, F., & Qiao, J. (2022). Machine learning aided construction of the quorum

sensing communication network for human gut microbiota. *Nature Communications*, *13*(1). https://doi.org/10.1038/s41467-022-30741-6

Ye, T., Zhang, W., Feng, Z., Fan, X., Xu, X., Mishra, S., Zhang, L., & Chen, S. (2020). Characterization of a novel quorum-quenching bacterial strain, burkholderia anthina hn-8, and its biocontrol potential against black rot disease caused by xanthomonas campestris pv. Campestris. *Microorganisms*, *8*(10). https://doi.org/10.3390/microorganisms8101485

Zhou, Z., Wu, X., Li, J., Zhang, Y., Huang, Y., Zhang, W., Shi, Y., Wang, J., & Chen, S. (2022). A novel quorum quencher, Rhodococcus pyridinivorans XN-36, is a powerful agent for the biocontrol of soft rot disease in various host plants. *Biological Control*, *169*. https://doi.org/10.1016/j.biocontrol.2022.104889

Appendix 1.

i. Multiple Normalization Schemes of QS-regulated Fluorescence Signal

Multiple different normalization approaches had been considered to determine which would most effectively yield meaningful interpretation of the fluorescence data. Leaman *et al*. 2018 used max-normalization of the mean-gray values of fluorescence and determined activation time by the peak of the second derivative over time for experiments in small volume aqueous enviornmey experiments, conducted in microfluidic devices.

For the agar well experiments, a second-derivative activation method was initially applied, and sigmoidal curve fitting was performed on the experimental data with Origin software. The peak of the second derivative from the fitted curve was then considered to correspond to the activation time. However, the perceived reliability of this approach was hindered by significant noise within QS-QQ community data and the intricacies of applying such derivative-based methods amidst this noise. Thus, a min-normalization scheme was adopted, as mentioned above, standardizing the initial fluorescence across experiments.

As mentioned in Chapter 2, the activation time was defined as a sustained increase in normalized fluorescence above the 1.10 threshold. To qualify as "sustained," the normalized value was required to exceed 1.10 for at least three consecutive 2.5-minute timesteps, representing a 7.5-minute interval. Furthermore, this elevated fluorescence had to persist without a decline exceeding five timesteps, equivalent to 12.5 minutes. Cases failing to meet these criteria were classified as non-activating. This evaluative approach is referred to as the "110% threshold method" in this thesis and was used for all the analysis.

As "110% threshold" activation time correlated well with peak 2nd derivative activation time, an increase of 10% in min-normalized fluorescence was thus considered to be the activation time (AT). Other thresholds, such as 115% and 120%, were tested, but they were not found to be an improvement upon 110% in terms of correlating with the 2nd derivative activation time. Upon confirming that the 110% threshold method produced similar results as the derivative approach in QS experiments, it was chosen for the noisier QS-QQ studies. This method, prioritizing a simple increase over a minimum value, proved more robust measure of activation

time against noise than the derivative method, which struggled with unreliable, excessively flat curves in some QS-QQ data. As show in Fig II.1, different activation time methods can be used and, notably, that peak 2nd derivative activation time and "110% threshold" activation time are similar across different QS agent populations.

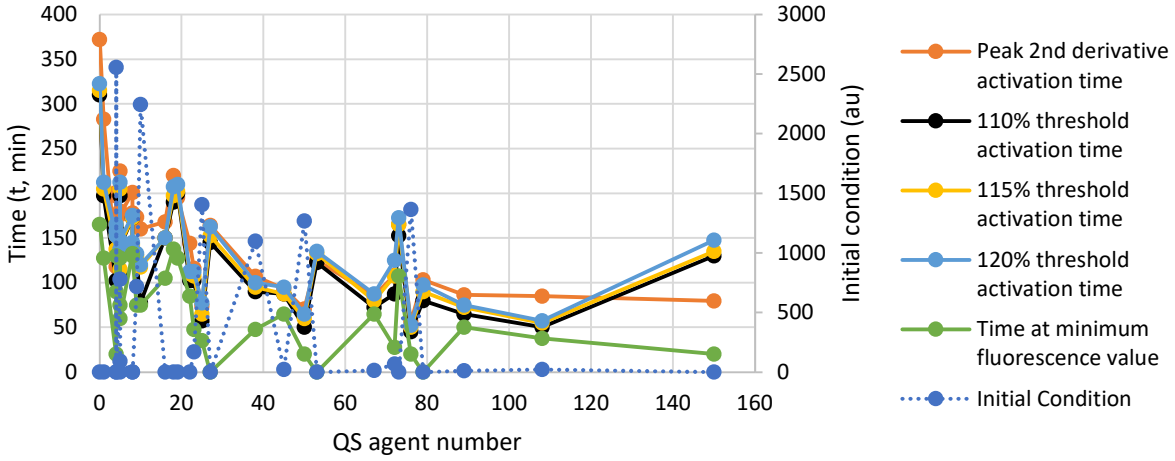

Fig. A.1. Comparison of activation time determination using different analytical methods. The "Peak 2nd derivative activation time" represents the original method of determining activation time used by Leaman *et al*. 2018, while "110% threshold activation time," "115% threshold activation time,", and "120% threshold activation time," depict the time points at which the min-normalized fluorescence surpassed 1.10, 1.15, and 1.20, respectively. "Time at minimum fluorescence value" indicates the moment when each experimental case reached its minimum fluorescence value, corresponding to a min-normalized fluorescence value of 1.0.

ii. Full Dataset of Experimental vs. Simulation, TIR 1262 au QS strain

The following graphs present the complete dataset of QS-only or QS-QQ experiments of the TIR 1262 au strain, not included in Chapter IV for brevity. The first set shows activation time.

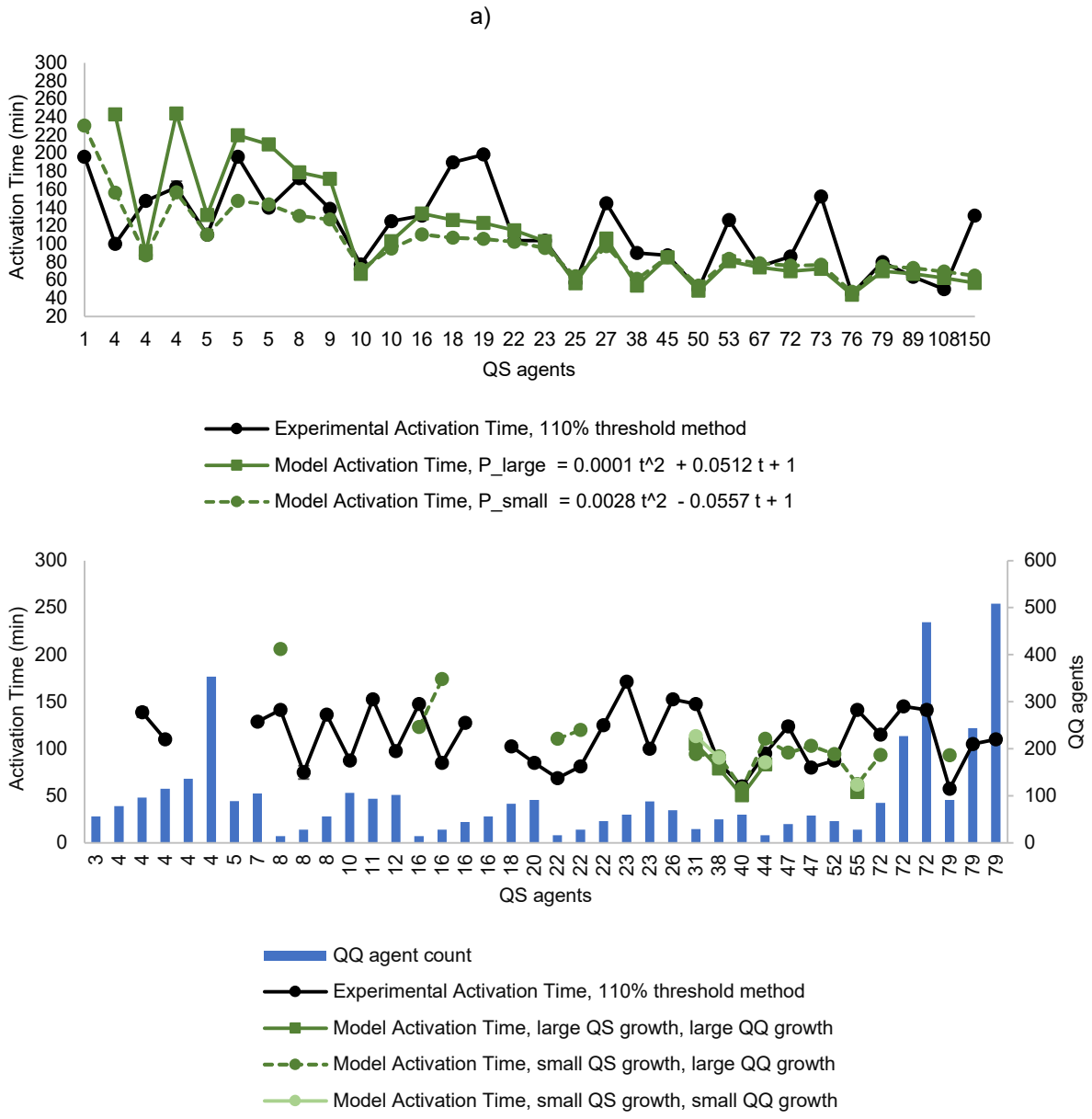

Fig. A.2. Simulation vs Experiments for TIR 1262 au strain, with optimized AHL upregulation threshold Q_0, basal AHL production rate A_1, and upregulated production rate A_2. Subfigure a) QS-only activation time; b) QS-QQ activation time.

The next graphs show the AUC data.

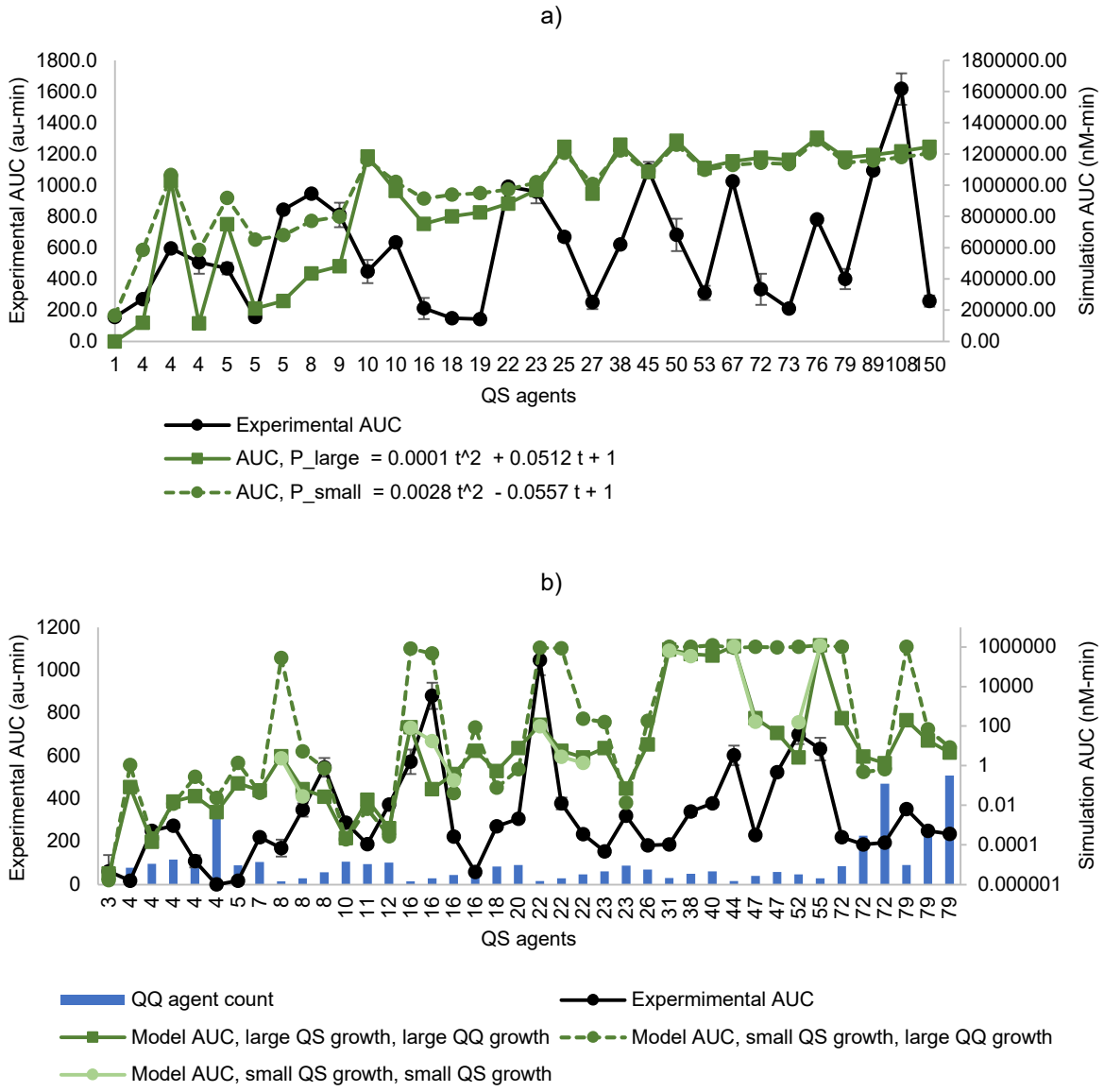

Fig. A.3. Simulation vs Experiments for AUC for TIR 1260 (BioBrick), with optimized AHL upregulation threshold Q_0, basal AHL production rate A_1, and upregulated production rate A_2. Subfigure (a) QS-only Area-Under-Curve; (b) QS-QQ Area-Under-Curve, arranged by increasing QS agents.

As can be seen, these graphs show similar and consistent trends with the ones discussed in Chapter IV.

It is important to note that the "small QS growth, small QQ growth" model was exclusively applied for QQ agent populations not exceeding 60 agents.